Protected STED and Multicolour Multilevel STED Nanoscopy

DISSERTATION
zur Erlangung des Grades eines Doktors
der Naturwissenschaften

vorgelegt von
Sven-Christian Sidenstein, M.Sc. Chemie

eingereicht bei der Naturwissenschaftlich-Technischen Fakultät
der Universität Siegen
Siegen 2016

Gutachter:

Prof. Dr. Holger Schönherr, Department Chemie und Biologie, Universität Siegen

Prof. Dr. Dr. h. c. mult. Stefan W. Hell, Abteilung NanoBiophotonik, Max-Planck-Institut für Biophysikalische Chemie, Göttingen

Tag der mündlichen Prüfung: 11. August 2016

Abstract

The diffraction barrier of focused light has been overcome by modern superresolution fluorescence microscopy techniques. These methods harness transitions between signaling and non-signaling states of the marker molecules to make them discernible at length scales of few tens of nanometers. Although superresolution methods like STED (STimulated Emission Depletion) and RESOLFT (REversible Saturable Optical Linear Fluorescence Transitions) microscopy proved to be valuable tools for cell biology, neurobiology and other fields, further improvements are needed. For example, lower fluorophore bleaching rates and enhanced state contrasts of the molecule ensemble are desired. Moreover, biological studies ask for better multicolour schemes allowing simultaneous imaging of multiple cellular structures with nanoscopic resolution. In this thesis, novel methods for coordinate-targeted superresolution microscopy are presented, which take up these challenges. Superresolution imaging with Multiple Off-State Transitions (MOST) is introduced and realized by reversible photoswitching and STED of fluorescent proteins leading to a new method called 'protected STED'. On the basis of measurements in different biological samples, it can be shown that in protected STED both fluorophore bleaching is reduced and state contrast is enhanced compared to conventional coordinate-targeted superresolution methods. Also, in this theses, a novel multicolour scheme is presented, which is based on a STED wavelength of 620 nm and which is valuable for imaging of both fixed and living samples. Furthermore, with multilevel STED, a new method was developed, which in multicolour imaging with a single STED beam improves both the image quality and avoids unnecessary STED light doses. Three-colour superresolution imaging harnessing multilevel STED was utilized to study nanoscale protein distributions in mature neurons. Periodic actin/βII spectrin lattices were found to be present along dendrites and thick spine necks, but they are absent from pre- and post-synaptic sites. These findings add new pieces to the picture of the nanoscale cytoskeletal arrangement in neurites.

Kurzdarstellung

Die Beugungsgrenze fokussierten Lichtes wurde durch moderne hochauflösende Fluoreszenzmikroskopieverfahren überwunden. Diese Methoden nutzen die (ir-)reversiblen Übergänge in leuchtende und nicht-leuchtende Zustände der Markermoleküle aus, um sie auf der Längenskala von wenigen zehn Nanometern unterscheidbar zu machen. Obwohl Methoden wie STED- (STimulierte Emissions-Depletions) und RESOLFT- (reversibel sättigbare optische Fluoreszenzübergänge, englisch REversible Saturable Optical Linear Fluorescence Transitions) Mikroskopie bereits gezeigt haben, dass sie wichtige Werkzeuge für die Zellbiologie, Neurobiologie

und andere Forschungsgebiete sein können, sind weitere Verbesserungen nötig. Dies betrifft zum Beispiel das Ausbleichen von Farbstoffmolekülen und den erreichbaren Zustandskontrast innerhalb des Molekülensembles. Des Weiteren werden für biologische Studien weiter verbesserte Mehrfarbenschemata benötigt, um gleichzeitig mehrere zelluläre Strukturen mit nanoskopischer Auflösung abbilden zu können. In dieser Arbeit werden neue Methoden für die Bewältigung dieser Herausforderungen vorgestellt. Zum einen wird die hochauflösende Mikroskopie mit mehreren Ausschaltübergängen (englisch Multiple Off-Switching Transitions, MOST) als neues Konzept eingeführt. Es wurde in der Form von „protected STED“ realisiert, indem reversibles Fotoschalten und STED fluoreszierender Proteine kombiniert wurden. Anhand von Messungen in diversen biologischen Proben kann gezeigt werden, dass in „protected STED“ sowohl das Farbstoffbleichen reduziert als auch der Zustandskontrast erhöht sind. Zum anderen wird ein Mehrfahrbenschema zur STED-Mikroskopie fixierter und lebender Proben präsentiert, das mit einer neuartigen STED-Wellenlänge von 620 nm realisiert wurde. Mit „multilevel STED“ wird außerdem eine Methode eingeführt, die in Mehrfarbenaufnahmen mit einem einzelnen STED-Strahl sowohl die Bildqualität verbessert als auch unnötige STED-Lichtbeaufschlagung vermeidet. Das neue Schema und „multilevel STED“ wurden genutzt, um Dreifarben-Hochauflösungsbilder der nanoskaligen Proteinverteilung in vollentwickelten Neuronen aufzunehmen. Ein periodisches Aktin/βII-Spektrin-Gitter konnte entlang von Dendriten und in größeren dendritischen Dornen nachgewiesen werden. In Prä- und Postsynapsen bleibt es jedoch aus. Damit konnten weitere Puzzlestücke zum Bild der nanoskaligen Zytoskelettstruktur in Neuronen hinzugefügt werden.

Contents

List of Abbreviations

1P	one photon
2D	two dimensional
2P	two photon
3D	three dimensional
AC	actin chromobody
AFM	atomic force microscopy
AOM	acousto-optic modulator
APD	avalanche photodiode
Bsn	Bassoon
cw	continuous wave
DNA	deoxyribonucleic acid
(E)GFP	(enhanced) green fluorescent protein
Exc.	Excitation
FCS	fluorescence correlation spectroscopy
FPGA	field programmable gate array
FWHM	full width at half maximum
GSD	ground state depletion
MOST	multiple off-state transitions
NA	numerical aperture
NFasc	neurofascin
OPO	optical parameteric oscillator
(F)PALM	fluorescence photoactivation localization microscopy
PSD	post-synaptic densities
PSF	point spread function
Phall	phalloidin
RESCue	reduction of state transition cycles
RESOLFT	reversible saturable optical linear fluorescence transitions
RSFP	reversibly switchable fluorescent protein
SIM	structured illumination microscopy
Spec	spectrin
STED	stimulated emission depletion
STORM	stochastic optical reconstruction microscopy
TIRF	total internal reflection fluorescence

Chapter 1

General Introduction

Nowadays, the human kind is able to study natural processes on almost all length and time scales. Astronomers are tracing signals which traveled through the cosmic space for longer than thirteen billion years. Physicists are hunting up elementary particles, which constitute the matter, we are made of. Chemists are observing reactions between atoms and molecules in real time and biologists are revealing complex cellular processes being responsible for our viability. In many of these experiments, light plays an important role as information carrier. With their spectral and temporal properties, light photons report about the emitting or reflecting species and the space which they passed.

The light microscope is one of the most widely used instruments that is based on the detection of light. Since the 17^{th} century, it is employed for magnifying biological structures. The transparency of cells for visible light makes it possible to have a look into the smallest unit of life. With time, microscopes became better and better and structures could be captured with even more details and high contrast. At a certain point, the quality of the lenses focusing the light into the sample and onto the detector did not limit the resolution of the microscopes any more. The diffraction limit described by Ernst Abbe in 1873 now set the boundary for the acuity of the attained images[(1)]. Accordingly, the minimal focus size produced by a lens is given by:

$$r_{lateral} \approx \frac{\lambda}{2n\sin(\alpha)} \tag{1.1}$$

and

$$r_{axial} \approx \frac{\lambda}{2n\sin^2(\alpha/2)} \tag{1.2}$$

$r_{lateral}$ and r_{axial} denote the full width at half maximum (FWHM) of the focused spot in the lateral and axial dimensions, respectively. λ is the wavelength of the focused light, n the

refractive index of the medium and α the semi-aperture angle of the lens. According to Abbe's law, the resolution is increased for smaller wavelengths and lenses of higher numerical aperture $NA = n\sin(\alpha)$. The proportional connectivity of wavelength and resolution is harnessed in electron microscopy, where strongly accelerated electrons with de Broglie wavelengths as small as 1 pm are used for creating high resolution. However, in far-field microscopy with visible light both factors can be optimized only to a certain extent. Standard microscopes equipped with a high NA objective lens typically provide resolutions of $r_{lateral} \approx 500\text{ nm}/(2 \cdot 1.4) \approx 180\text{ nm}$ and $r_{axial} \approx 500\text{ nm}/(2 \cdot 1.518 \cdot \sin^2(67°/2)) \approx 541\text{ nm}$.

Several techniques based on special illumination schemes and mathematical methods have been developed to push the diffraction barrier to its ultimate limits. In two- or multiphoton excitation microscopy, simultaneous absorption of two or m photons of respective lower energy excites fluorophores[2]. Due to the non-linear dependency of the resulting emission on the excitation intensity, the width of the effective focal spot is reduced by a factor $\sqrt{2}$. However, doubling of the excitation wavelength produces a twofold enlarged effective focal spot so that the attainable resolution is in fact worse compared to the respective one-photon excitation[3]. Advantages of two-photon microscopy lie in other factors such as a deep penetration depth, low scattering and the restriction of photobleaching to the focal spot.

Sample illumination with structured light has been harnessed in different ways for increasing the spatial resolution. Structured Illumination Microscopy (SIM) based on standing wave patterns provides two-fold increased resolution in both lateral and axial dimensions[4–6]. The diffraction-limited, low frequency illumination pattern interacts with the high frequency patterned sample giving rise to a third, lower frequency pattern, the so-called Moiré fringes. In contrast to the high frequencies of the sample, the Moiré fringes can be transmitted by the microscope optics. Fourier transformation of the recorded image, separation of the high frequencies from the lower frequencies and transformation back to real space produces an image with increased spatial resolution. Several raw images recorded with different phases and orientations of the illumination pattern with respect to the sample are used to calculate one final superresolution image.

Two opposing lenses in a spot-scanning 4-Pi[7] or wide-field I^5M[8] configuration are able to increase the axial resolution down to 70-150 nm. Interference of coherent excitation light or the emitted light or of both is reducing the effective excitation and detection spots, respectively. Side lobes of the excitation point spread function (PSF) can be suppressed by, for example, combination with two-photon excitation. The high axial resolution is especially interesting for investigations of three-dimensional (3D) complex samples.

The spatial resolutions of the (far-field) microscope techniques discussed so far are still

fundamentally limited by diffraction. Giving up the use of lenses and coupling light into subdiffraction-sized apertures of, for example a tip, can be used to generate subdiffraction resolution[9;10]. At distances ~$\lambda/2$ to the output of the tip, light evolves as an exponentially decaying evanescent field. Interaction of the non-diffracting evanescent light with the sample allows imaging with a lateral resolution <20 nm[11] and therewith far below the diffraction limit. However, this requires not only to bring the tip as close as a few nanometer to the sample, but also limits the probed volume to the surface of the sample[12;13]. The latter is a severe constraint when imaging of the 3D structure of cells is intended. Similarly, axial resolutions below the diffraction limit can be obtained by Total Internal Reflection Fluorescence (TIRF) microscopy. In this case, fluorescence is induced by the evanescent field generated at the glass/medium interface through highly inclined angle illumination. The evanescent field intensity decays exponentially within 100-200 nm so that the probed volume is confined to the proximity of the interface. In this sense, TIRF techniques can also be considered as near-field methods, since axial subdiffraction resolution is limited to the glass/sample interface, e.g. the lower cell membrane. Atomic Force Microscopy (AFM) is another near-field technique providing nanoscopic resolution[14–16]. By scanning the sample with a sharp tip and measuring its deflection, topographical and mechanical information can be obtained. Although specific interactions with, for example, peptides or antibodies can be measured by chemically modifying the tip, conventional AFM is a label-free technique without molecular specificity. However, the latter is often required for biological studies. That is why AFM is frequently combined with optical microscopy methods such as Fluorescence Lifetime Imaging Microscopy (FLIM)[17], Fluorescence Correlation Spectroscopy (FCS)[18], Fluorescence Recovery After Photobleaching (FRAP)[19] or STED[20]. Scanning Electron Microscopy (SEM)[21] and Transmission Electron Microscopy (TEM)[22] provide resolutions down to the level of single molecules or even atoms by scanning the sample with a beam of highly accelerated electrons. Yet, the sample preparation is complex and the imaging is carried out under high vacuum and often at cryogenic conditions. Environmental SEM enables imaging of biological samples under lower vacuum conditions, though imaging of living cells is still not possible. The electron beam would be reflected by the water layer keeping the cells alive or, when dried, by the remaining salt and protein crystals covering the cells. Nevertheless, cryo-electron microscopy is an indispensable tool especially for structural biology[23]. In correlative light and electron microscopy, the below 15 nm resolution of electron microscopy is combined with fluorescence microscopy yielding information about both structure and function of biological systems. However, none of the mentioned near-field methods, except of the correlative ones, provides the same potentials as fluorescence microscopy for biological studies, which are noninvasiveness/live-cell compatibility, molecular specificity, multicolour optionality and a micrometer to millimeter depth of focus. Hence, fundamentally

improving the resolution of lens-based fluorescence microscopy is highly desired. Yet, a strategy overcoming Abbe's law is needed.

1.1 Overcoming the diffraction limit in the far-field

In the early 1990s, the idea came up to make use of the properties of the (fluorescent) marker molecules so far only harnessed to *highlight* structures of interest in samples [24–26]. All previous attempts to increase the resolution of light microscopes focused on instrumental improvements of the microscope. The idea initialized the completely new scientific field of lens-based super-resolution fluorescence microscopy, or nanoscopy, whereby STimulated Emission Depletion (STED) microscopy became the first method truly breaking the diffraction barrier [24;27;28].

All far-field fluorescence nanoscopy methods discern fluorescent molecules at subdiffraction length scales by preparing them in distinguishable states for the time point of detection [29]. Usually, these molecular states are a non-fluorescent (off) and a fluorescent (on) state. Importantly, the concept is not limited to fluorescence and, in fact, even not to optics [30]. Only the defined transfer between two states is decisive. There are two different experimental approaches, which are outlined in the following. Then, STED microscopy is discussed in more detail.

1.1.1 Coordinate-targeted methods

In STED microscopy, fluorophores are toggled between the ground state S_0 (off) and the first excited singlet state S_1 (on). Stimulated emission is used to 'switch' molecules off. In RESOLFT (REversible Saturable Optical Linear Fluorescence Transitions) microscopy [31;32], molecules are switched between a non-emitting and an emitting form, for example, via a cis/trans isomerization or a hydration/dehydration reaction. It has been realized both with Reversibly Switchable Fluorescent Proteins (RSFPs) [33–39] and synthetic photochromic markers [40]. STED microscopy can be understood as a special case of RESOLFT microscopy. However, in the following, the term RESOLFT microscopy only describes implementations using RSFPs.

RESOLFT and STED microscopy both define the spatial positions of the emitting and non-emitting states by illumination with patterns of light driving the respective transitions (coordinate-targeted methods). Images with subdiffraction resolution are readily obtained by scanning these patterns over the sample. More specifically, STED and RESOLFT methods spatially confine the on-state by saturating the off-transition so that no post-processing of data is needed. Yet, subdiffraction resolution is also accessible by confining the off-state via saturation of the on-transition. The resulting images are in this case 'negative images' of the sample in which features appear as subdiffraction-sized dark regions. These datasets can be converted to 'positive images' by mathematical deconvolution. Respective methods are called Saturated Patterned Excitation Microscopy (SPEM) [41] and Saturated Structured Illumination Microscopy

(SSIM)[42], respectively. In their case, samples are illuminated with standing waves of intense excitation light depleting the ground state and imprinting steeply confined dark areas in the sample[43]. In comparison to classical SIM, camera images of the fluorescence emission contain spatial frequencies of higher order which improve resolution given that they can be disentangled from the lower frequency noise[44]. So far, SSIM and SPEM have only been demonstrated experimentally for dye-labeled polystyrene beads, since saturating the excitation means that almost the entire population is transferred to the bleaching-prone S_1 state. Saturated SIM at low light levels is possible with RSFPs. Similar to RESOLFT, patterned off-switching[45] or on-switching[46] light is applied to confine the on- or the off-state of the protein ensemble, respectively. In fact, both on- and off-switching can be combined by superimposing the minima of both illumination patterns[46]. Again, the 'negative images' obtained when confining the off-state, still contain a high amount of low frequency information which may lead to artifacts in the final images[44;47]. On the contrary, confining the on-state produces 'positive images' which almost only contain high frequency information given that high on/off contrasts are achieved.

Ground State Depletion (GSD)[26] of ultra-photostable nitrogen-vacancy centers in diamond has been realized by pixel-wise scanning with an intense doughnut-shaped excitation beam[30;48]. Deconvolution of the 'negative' images yielded final images with resolutions below 10 nm. By adding a second, regularly focused excitation beam co-aligned to the intensity minimum of the doughnut, the confined state can be read out directly therewith avoiding the deconvolution step[30;49;50].

Coordinate-targeted methods require scanning of either the light pattern or the sample. Short image acquisition times in point-scanning STED, GSD and RESOLFT modalities can be realized by fast scanners such as resonant[51] or electro-optic scanners[52]. Significant acceleration is also obtained by employing multiple observation spots, *i.e.* by parallelization[38;53–56].

1.1.2 Coordinate-stochastic methods

Molecules at subdiffraction length scales can also be differentiated without applying patterned light. The position of a single emitting molecule can be determined by calculating the centroid of the diffraction-blurred spot of fluorescence focused on a camera. Thereby, the localization precision scales with the square root of the number of detected photons and can be as good as a few nanometers. Preparing sparse subsets of simultaneously signaling molecules, which are separated by distances larger than the diffraction-limited spot size, and recording them on many (thousands) camera images, yields a map summarizing the determined molecule positions. For high numbers of molecule localization, this map becomes an image of the sample with diffraction-unlimited resolution. Importantly, localization *per se* is not able to provide superresolution. The decisive step in these coordinate-stochastic methods is again the transfer of molecules to different

states. The principle has been first realized in the form of (F)PALM ((Fluorescence) Photo-Activation Localization Microscopy)[57;58] and STORM (Stochastic Optical Reconstruction Microscopy)[59]. In (F)PALM, photoactivatable proteins[57;58] or dyes[60] are driven to the on-state, read-out and bleached irreversibly. STORM relies on reversible photoswitching of organic fluorophores, which is observed for cyanines under certain buffer conditions[59]. Alternatively, molecules can be transferred to long-lived dark states via intersystem crossing to triplet or redox states[61;62]. Furthermore, RSPFs[63;64], single-walled carbon nanotubes[65] and quantum dots[66] were employed for PALM and STORM as well. Coordinate-stochastic imaging has also been realized with temporal-stochastic switching of fluorophores in the form of, for example, PALMIRA (PALM with Independently Running Acquisition)[63;64], GSDIM (Ground State Depletion followed by Individual Molecule return)[67] and direct-STORM[61;68]. These methods harness the stochastic blinking of molecules (at random positions) caused by random transitions to dark states or switching cross-talk of the single, freely-running laser. Another method, called SOFI (Superresolution Optical Fluctuation Imaging) microscopy[69], uses higher-order statistical analysis of the blinking behavior of simultaneously signaling molecules therewith enabling high-speed superresolution imaging.

1.2 STED nanoscopy

In STED nanoscopy, fluorescent molecules in subdiffraction-sized regions are prepared in the emitting first excited singlet S_1 and the ground state S_0 for the time-point of detection (Fig. 1.1a).

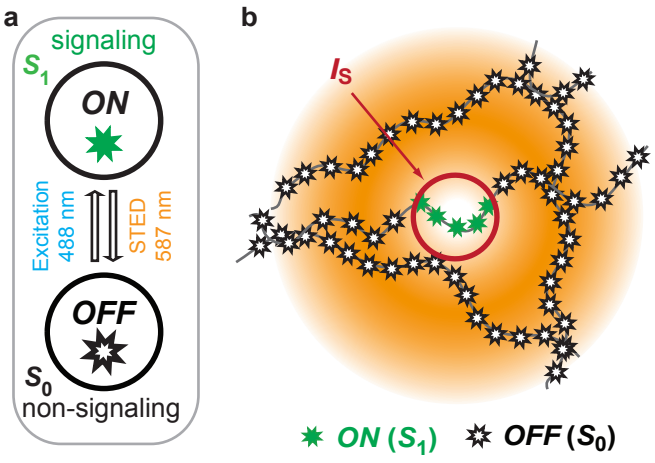

Figure 1.1: State configuration in STED nanoscopy. *(**a**) In STED nanoscopy, the signaling ON and non-signaling OFF states correspond to the singlet states S_1 and S_0 of the fluorophore, respectively. (**b**) Upon excitation to S_1 (not shown), fluorophores residing in regions of STED light intensities $>I_S$ are transferred back to S_0. Only molecules in a subdiffraction-sized area remain in the signaling ON state. Colours encode the wavelength of the light driving the respective transition and emitted as fluorescence, respectively. Colors in the figure indicate light wavelengths being typically found in STED nanoscopy of GFP. Figure adapted from Danzl, Sidenstein et al.*[70].

To this end, molecules are illuminated by excitation and STED light, which transfer molecules to S_1 and immediately back to S_0 via stimulated emission, respectively. The wavelength of STED light is situated at the red end of the fluorophores emission spectrum thereby avoiding pronounced re-excitation to S_1. In a standard implementation, the STED light beam is focused to a doughnut-shaped spot in the sample which is superimposing the circular excitation spot. Therewith, remaining spontaneous fluorescence is confined to the area within the doughnut center (Fig. 1.1b). High resolutions are obtained by saturating the off-state by applying high STED powers. Typically, excitation and STED light are delivered by pulsed lasers. Since excited state lifetimes are in the order of few nanoseconds, precise synchronization of the laser pulses has to be ensured. Averaged over all orientations of the dyes, the fraction of fluorescence still being detectable after the action of the STED pulse along the x-coordinate $\eta(x)$ can be well described by an exponential function in the form [71]

$$\eta(x) \cong exp(-ln(2)I_{STED}(x)/I_S). \tag{1.3}$$

I_{STED} is the STED intensity and I_S is the saturation intensity, needed to transfer, for example, 95% of the molecules to the dark state. Importantly, this strong non-linear dependency of the fluorescence on the STED intensity is the key to the multiple gain in resolution. Assuming a linear electric field close to the focal point, the de-excitation pattern can be approximated by a parabola [72]:

$$I_{STED}(x) = 4I_{STED}a^2x^2 \tag{1.4}$$

The resulting effective point spread function (PSF) is given by $h_{eff}(x) = h_c(x)\eta(x)$ and is a Gaussian with reduced width along x [72]:

$$h_{eff}(x) = exp(-4ln(2)x^2(d_c^{-2} + a^2\zeta)) \tag{1.5}$$

d_c denotes the confocal resolution, a the pattern steepness along x and ζ the saturation factor defined as I_{STED}/I_S. The full width at half maximum of h_{eff} becomes [72]:

$$d = \frac{d_c}{\sqrt{1 + d_c^2a^2\zeta}} \tag{1.6}$$

The confocal resolution is recovered for $\zeta = 0$ whereas for high STED intensities, *i.e.* for high saturation levels, d becomes independent of the confocal resolution [72]:

$$d = \frac{1}{a\sqrt{\zeta}} \tag{1.7}$$

Indeed, this square root dependence of the resolution on the saturation level could be experimentally confirmed by measurements on fluorescent beads[72]. STED microscopy has also been realized with continuous wave (cw) beams[73]. However, nowadays, fiber lasers providing nanosecond-long pulses with energies of up to 30 nJ/pulse at repetitions rates of 20 or 40 MHz are preferred as STED lasers. In combination with gated detection[74], which removes fluorescence emitted during the action of the STED pulse, imaging down to a resolution of 20 nm has been demonstrated with synthetic fluorophores[75;76]. The maximum attainable resolution gain depends among others on the quality of the staining, the saturation intensity of the STED process, and the photophyiscal properties of the fluorophore. Especially its resistance against photobleaching is indispensable for obtaining high resolutions. Fluorescent nitrogen vacancies in diamonds, which are extremely photostable, enabled STED imaging down to a resolution of 5.8 nm[77]. On the contrary, genetically-encoded markers like the Green Fluorescent Protein (GFP) are much less photostable and therefore limit the attainable resolution to about 40-50 nm. Largely, bleaching is evoked by the intense STED beam acting on the excited state of the fluorophores. Although, in principle, stimulated emission reduces the risk for intersystem crossing to dark states by de-exciting the molecules to the ground state, detrimental processes like excitation to higher lying states are masking this effect. All the more, as relatively high STED powers are needed, because the on/off state difference created by inducing the transition $S_1 \rightarrow S_0$ through stimulated emission is short-lived. The lifetime of S_1 is typically 1-4 ns and the molecular optical cross-section about $\sim 10^{-17}$ cm^2 leading to $I_S \approx$ 5-20 MW/cm^2. This corresponds to maxima $I_{max} \approx$ 20-1000 MW/cm^2. Consequently, one way to reduce bleaching in STED microscopy is to prevent molecules from assuming S_1 in regions of high STED light intensity (see following chapter).

During the last 15 years, performances of STED modalities have been continuously improved. Reviewing of all STED implementations and related refinements would be beyond the scope of this introduction. In general, STED microscopes became more efficient in terms of image quality, imaging speed and multicolour compatibility. The introduction of compact, high power fiber lasers for pulsed STED[76] made microscopes significantly simpler and more cost-effective. Developments like the easySTED phase plate[78] or the introduction of FPGA- (Field Programmable Gate Array) based microscope control further reduced setup and hardware complexity. Advanced STED implementations harnessing, for example, spatial light modulators or adaptive optics increased the versatility of the setups[79;80]. Imaging schemes like D- and T-Rex microscopy[81;82], which promote dark- and triplet relaxation, and RESCue-STED[83] for Reducing the number of State Transition Cycles made STED at lower bleaching rates possible. Several multicolour imaging schemes have been realized which are summarized in Section 3.1.1. STED imaging with nanoscopic resolution in axial direction can be achieved in

the simplest form by inserting a top-hat phase plate in the STED beam path giving rise to a bottle-beam (or 'z-doughnut', see Fig. 2.29 on page 41)[28;84–86]. Alternatively, illumination by two opposing objective lenses in a 4pi configuration[87–89], single plane illumination[90] or adaptive optics[91;92] are able to provide axial resolution gain. All modalities can be combined with the classical doughnut-shaped focus resulting in an effective isotropic observation volume. 4pi 'isoSTED' has been demonstrated with resolutions down 30 nm in all spatial directions[93].

1.3 Fluorescent labels for STED nanoscopy

Different types of fluorescent markers enabling microscopy over the whole visible spectrum have been published and tested for STED. One prominent example is the synthetic fluorophore KK114[94;95], which performs exceptionally well with the 775 nm STED line. Live-cell STED microscopy with resolutions down to 50 nm was demonstrated using fluorescent proteins like GFP[96;97], Citrine[98;99] or TagRFP[100] and was even transferred to the living mouse brain[101]. Synthetic fluorophores as alternatives to fluorescent proteins for imaging intra-cellular structures have been explored for STED as well[102–105]. In particular, the silicon rhodamine[103] has a great potential as demonstrated by imaging actin in living neurons[106;107]. Likewise, research focuses on developing improved red fluorescent proteins whose brightness is typically lower than those of their green counterparts. Examples of recently introduced red markers potentially interesting for STED applications are mGarnet[108], mScarlet[109], and bacterial phytochrome photoreceptor based fluorescent probes with excitation and emission peaks in the near-infrared region[110]. Additionally, fluorescent quantum dots[111] or nanodiamonds[77] may play a role as labels for STED microscopy in future. In light of the rapid advancements in marker development, even higher imaging performances of all superresolution methods can be expected in future. Synthetic, reversibly switchable fluorophores with low switching fatigue are highly awaited and promising candidates for coordinate-targeted superresolution microscopy[112]. In addition, new fluorophore concepts proposing self-healing dyes, multi-chromophore systems or chromophores with plasmonic effects could lead to markers with superior brightness and photostability[113].

Along with increasing resolution comes the need for better labeling techniques. Important parameters are the label size, the labeling density and specificity, and the multicolour compatibility. Accordingly, good stainings are characterized by a uniform and continuous labeling of the structure of interest without artifacts like dye agglomerates and unspecific staining. Often, immunolabeling procedures based on a primary antibody binding to the structure of interest and a dye-labeled secondary antibody recognizing the primary one, are utilized for single or multicolour stainings of fixed samples. However, due to the 12-15 nm size of the antibodies[114], the dye molecule is brought only as close as 24-30 nm to the epitope which may already significantly influence the precision and accuracy of superresolution measure-

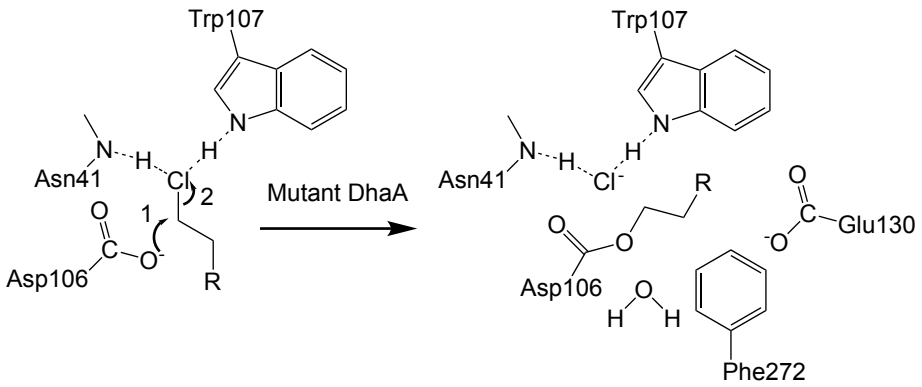

Figure 1.2: Halo-tag reaction. *The chloroalkane linker of a dye (R) is inserting into the binding pocket of a modified Rhodococcus dehalogenase (mutant DhaA). There the chlorine atom is stabilized via hydrogen bonds and is split off in a nucleophilic displacement reaction under formation of an ester bond. Base-catalyzed hydrolysis of the enzym-alkyl product is suppressed, because the Phe272 replacing the His272 of the wild-type deahalogenase is not able to stabilize the water molecule. This results in a persistent binding of the dye to the fusion protein.*

ments[115;116]. Site-specific labeling with single-stranded antibodies of camelid origin, so-called nanobodies[117], can reduce the epitope-label distance to below 2 nm[118]. Labeling of structures inside living cells is usually accomplished by expression of a vector encoding a fusion protein of a fluorescent protein and a protein binding to or being incorporated into the structure of interest. In this work, labeling of actin inside living cells and neurons was achieved by expressing a nanobody-rsEGFP2 construct which has a higher binding affinity to actin than the Lifeact protein[119]. Cell-penetrating synthetic dyes can be attached to the target structure by bio-orthogonal reactions. Specific and covalent labeling can be realized by SNAP[120]-, CLIP[121]- or Halo-tag[122] fusion proteins. To this end, dyes are modified with a specific linker, like a chloroalkane (Halo-tag). The chloroalkane reacts under formation of a stable ester bond with a genetically-modified Rhodococcus dehalogenase expressed as fusion protein by the cell (Fig. 1.2). Ideally, the unbound dye is not fluorescent and lights up upon binding to target so that remaining dye does not have to be washed out. Such fluorogenic behavior is observed, for example, in case of the aforementioned silicon rhodamine[106], which enables imaging of the characteristic 190 nm cortical actin pattern not possible with nanobodies or Lifeact.

1.4 Applications of STED nanoscopy

Fluorescence microscopy is especially in the life sciences a routinely applied method. Yet, fluorescence techniques and STED microscopy in particular are also in the toolbox of material scientists[123;124]. However, in most cases, STED microscopy provides new insights in studies of cell biology, microbiology or neurobiology[125–129]. STED microscopy revealed, for example, the doughnut-shaped structure of the protein Bruchpilot in active zones of neuromuscular presynapses of *Drosophila*[130]. The strong influence of dense cortical actin meshwork on the lipid

and protein organization of eukaryotic cell membranes was studied by STED imaging and STED-FCS measurements[131;132]. Also, STED microscopy helped to study the nanoscale protein organization in mitochondria[133]. Recently, STORM and STED microscopy revealed a periodic interplay of cortical actin and spectrin structures in various types of neuronal cells[107;134–136] also investigated in the project presented in Chapter 3. In light of the advancing commercialization and methodical simplification of the techniques, increasing impact of superresolution microscopy on various scientific fields can be expected.

1.5 Motivation

Although STED microscopes became significantly simpler and more advanced in recent years, there is still room for improvements. Bleaching of fluorophores is still one major limitation especially in life cell applications, since genetically-encoded markers are considerably less photostable compared to synthetic fluorophores and live-cell labeling strategies based on cell-penetrating dyes are still in the early stage of development. Furthermore, coordinate-targeted methods like STED and RESOLFT crucially rely on the state contrast imprinted on the fluorophore ensemble. In particular, image quality in RESOLFT nanoscopy with reversibly switchable proteins is negatively affected by signal background of non-switchable protein subpopulations. Similarly, STED images of dense samples suffer from signal background stemming from out-of-focus regions not well suppressed by the STED PSF. Hence, novel approaches for reducing fluorophore bleaching and increasing state contrast are still required. In Chapter 2, a general concept tackling both problems is presented.

STED light may not only lead to bleaching of fluorophores but also interacts with the sample itself. In particular, STED light of ~590 nm is absorbed to a certain extent by cellular structures which can induce cellular movements and can, in worst case, lead to photodestruction. At wavelengths above 600 nm, light absorption in biological samples is considerably reduced[137]. Hence, it is not only desirable to minimize the STED power requirements, as realized by the concept presented in Chapter 2, but concomitantly to shift the STED wavelength further to the red visible or near-infrared spectrum. In Chapter 3, STED at 620 nm is explored for the use with different types of markers in fixed and living samples. Moreover, straightforward imaging schemes for simultaneous recording of more than two species with subdiffraction resolution are still rare. Within the scope of the project presented in Chapter 3, strategies for improving multicolour STED imaging were developed.

Chapter 2

Coordinate-targeted fluorescence nanoscopy with multiple off-states[1]

2.1 Introduction

In a coordinate-targeted concept like STED, resolution is increased by scaling up the applied STED power so that I_S is surpassed at a smaller distance d from the doughnut center. This implies that in regions of the maxima, *i.e.* of the doughnut crest, intensities $I_{max} \gg I_S$ are impinged on the fluorophores and on the sample. Yet, for inducing the transition to the off-state with a high probability, only I_S is needed. Since the doughnut-shaped PSF is diffraction-limited as well, it cannot be engineered arbitrarily and the maxima cannot be avoided. So, high intensities are required for high resolution, but the maxima itself do not have a function. To the contrary, at high intensities fluorophore bleaching is increased, since detrimental processes like anti-Stokes excitation and excitation to higher-lying states are more competing [138]. At higher resolutions, bleaching is further exacerbated, because both I_{max} and the relative number of molecules exposed to intensities greater than I_S become larger. Concomitantly, the on/off contrast has to be enhanced as well, since the relative number of fluorophores located inside the d-sized region becomes smaller compared with those located outside. Hence, the probability of molecules to undesirably assume the on-state must decrease.

RESOLFT microscopy utilizes reversibly switchable fluorophores, typically fluorescent proteins (RSFPs) [139–141] for creating the on/off state contrast that generates diffraction-unlimited resolution. Specifically, RSFPs can be transferred by light to a metastable non-fluorescent form via, for example, cis-trans isomerization which either does not absorb the excitation light or

1 The project was conducted together with J.G. Danzl, C. Gregor, N.T. Urban, and P. Ilgen. Contributions are detailed on page 85. Results of the project were published as J.G. Danzl[†], S.C. Sidenstein[†], C. Gregor, N.T. Urban, P. Ilgen, S. Jakobs, S.W. Hell (2016) *Nature Photonics* **10**, 122-128. ([†]Equal contributors.)

decays rapidly by internal conversion back to the ground state without emitting a fluorescence photon. Due to the second to minute lifetime of the non-fluorescent state, high intensities for switching can be avoided by exchanging against switching time. Consequently, RESOLFT microscopy is considerably slower than STED microscopy, although fast switching proteins like rsEGFP2 [36] and the Dronpa [140] variant DronpaM195T [37;142] have been developed. Typical pixel dwell times required with these proteins are 100-500 µs which is still about one order of magnitude longer than those for STED microscopy. In case of the mentioned RSFPs, the off-switching is the most time-consuming step, since it is less quantum efficient compared to the on-switching. Imaging can be sped up to a certain extent by higher off-switching intensities. However, the on/off contrast of the molecule ensemble is reduced concomitantly due to cross-talk action of the off-switching light. This so-called 'switching background' leads to a confocal pedestal around subdiffraction-sized structures which renders densely packed structures less good discernible.

Hence, both STED and RESOLFT microscopy admit of improvement. In the following, a concept is presented which enables enhanced image quality of coordinate-targeted superresolution microscopy modalities.

2.2 MOST concept

It is proposed that molecules in high (STED) intensity regions can be protected and that the on/off contrast can be enhanced by harnessing multiple off-states and Multiple Off-State

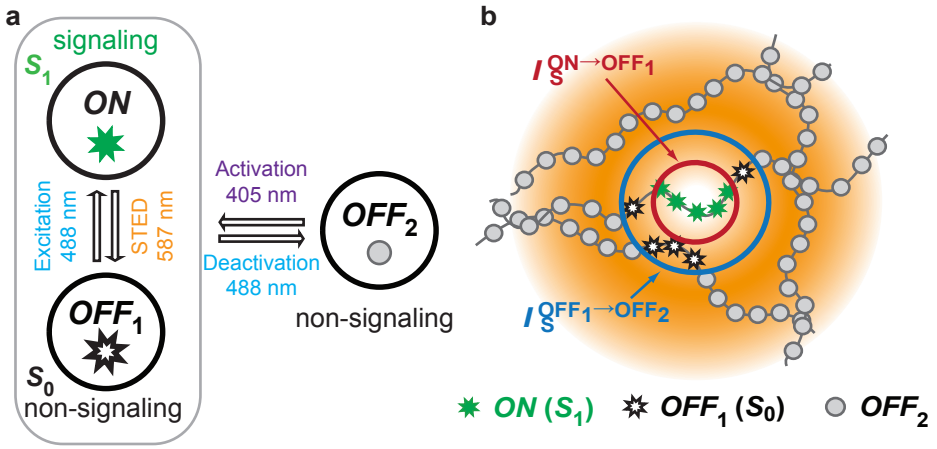

Figure 2.1: State configuration of a MOST scheme. *(**a**) In a MOST scheme, another non-signalling state OFF_2 is added to the basic states ON and OFF_1. Molecules can be reversibly transferred to OFF_2 by 488 nm deactivation and back by 405 nm activation light. (**b**) In a straightforward implementation, STED (shown in orange) and deactivation light (not shown) are applied as co-aligned doughnut-shaped foci. Superimposed with Gaussian-shaped activation and excitation foci (not shown), molecules in bleaching-prone regions of high STED intensities are transferred to OFF_2 by deactivation light (not shown). Subsequent application of STED light only acts on molecules close to the center, where the STED intensity is markedly reduced compared to the doughnut crest (compare Fig. 1.1b). Figure and caption reproduced from Danzl, Sidenstein et al. [70].*

Transitions (MOST) (Fig. 2.1a). Although, concatenation of state transitions has been explored extensively for superresolution [3;25], the combination of multiple off-states is a novel concept. Implementing MOST in combination with stimulated emission leads to a method called 'protected STED'.

In the simplest form of protected STED, molecules in the doughnut-shaped region are transferred to an additional second off-state (OFF_2) prior to the application of the STED light doughnut (Fig. 2.1b). STED light impinges then only on molecules located close to the doughnut zero, where STED intensity is markedly reduced compared to the maxima. In other words, STED light acts only at regions and in doses actually being required for increasing the resolution. The intensity maxima are essentially cut away by transferring the vulnerable fluorophores into a molecular state which does not absorb the STED light.

A straightforward way of realizing MOST nanoscopy in the form of protected STED is to combine STED with reversible photoswitching of proteins, as used in RESOLFT microscopy. The deactivated configuration serves as the second off-state OFF_2, whereas the S_0 and the S_1 states of the active configuration are the OFF_1 and the ON states, respectively (Fig. 2.2). In the active configuration, molecules can be excited from S_0 to the signaling state S_1, which is not possible for molecules in OFF_2. These molecules would first require activation. Also deactivated molecules must either not absorb STED light, or they must instantaneously relax back to OFF_2. If so, the molecules can be protected from bleaching by deactivation before being exposed to the intense STED light.

Potentially interesting markers for implementing protected STED are reversibly switchable descendants of the enhanced green fluorescent protein (rsEGFPs). On one hand, non-photoswitchable EGFP is frequently employed for *in vitro* and *in vivo* microscopy with STED wavelengths of ~590 nm [96;97;143]. On the other hand, rsEGFP2, a fast switching rsEGFP variant, has proven to be suitable for RESOLFT imaging [36]. Further candidates are, for

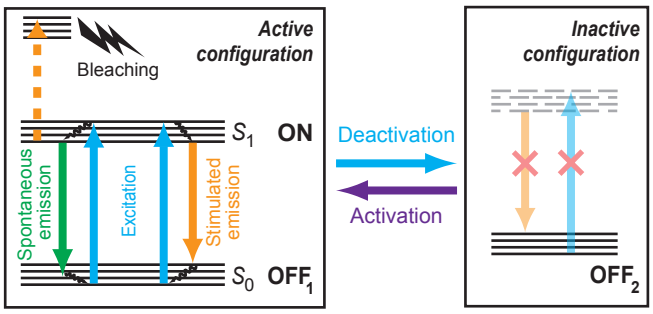

Figure 2.2: Simplified diagram of states harnessed for protected STED. *Conjunction of three states corresponding to the singlet states S_0 (OFF_1) and S_1 (ON) of the active configuration and a meta-stable state (OFF_2) of the deactivated configuration. Colour-coding indicates the wavelength of light driving the respective transition and of the emitted fluorescence, respectively for rsEGFP variants. The dashed arrow symbolizes excitation to higher lying states by the STED beam as an example for a pathway of fluorophore bleaching. Figure adapted from ref.* [70].

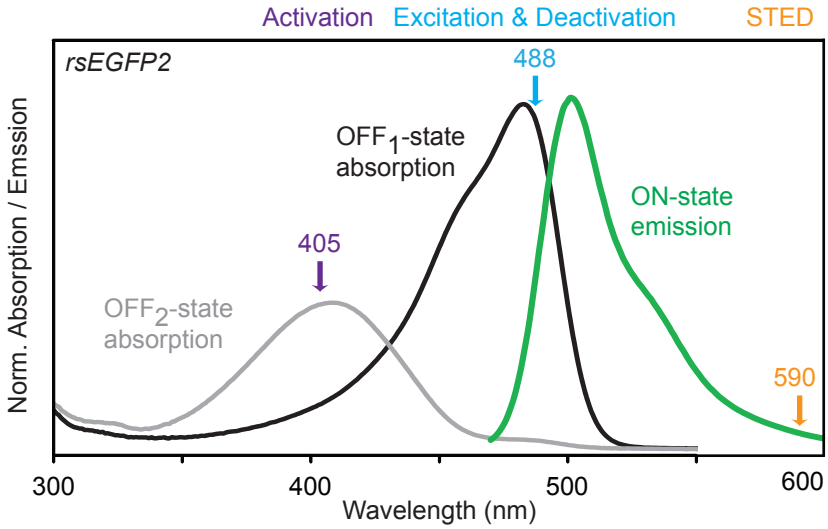

Figure 2.3: Spectral properties of rsEGFP2. *Normalized spectra of the rsEGFP2 OFF_2-state absorption (grey), the OFF_1-state absorption (black) and the ON-state emission (green). Emission is induced by excitation from the OFF_1-state by 488 nm light. STED is efficiently accomplished without pronounced anti-Stokes excitation by light of 590 nm. Transfer to OFF_2 is achieved with light of 488 nm and back to OFF_1 of 405 nm.*

example, the slower switching variants rsEGFP[34] and rsEGFP(N205S)[38] as well as DronpaM195T[37;142]. In the red spectral region, the mCherry descendant rsCherryRev1.4[39] is a potential candidate as well. Of course, switchable synthetic fluorophores[144] are also applicable to protected STED imaging. Although the diffraction barrier has been overcome by using bistable organic markers[40], the existing synthetic dyes do not provide enough switching cycles for coordinate-targeted superresolution imaging with high pixelation densities. On the contrary, an ensemble of rsEGFP2 molecules can be activated (at ~405 nm) and deactivated (at ~488 nm) more than 2,000 times before half of the molecules is bleached[36] (Fig. 2.3).

2.2.1 Image formation in MOST nanoscopy

The point spread function (PSF), h, can be understood as the normalized spatial probability distribution P of a molecule to assume a certain state. In case of protected STED, these are the probabilities: i) for activation, $P_{\mathrm{OFF1}(\leftarrow\mathrm{OFF2})}$; ii) for remaining active after application of the deactivation pattern, $P_{\mathrm{OFF1}(\rightarrow\mathrm{OFF2})}$; iii) for being excited to the fluorescent ON state, $P_{\mathrm{ON}(\leftarrow\mathrm{OFF1})}$; and iv) for remaining in the ON state after action of the STED beam pattern, $P_{\mathrm{ON}(\rightarrow\mathrm{OFF1})}$. The probability distributions depend on the shape of the respective spatial light distribution and the kinetics of the induced transition. The regular-shaped excitation and activation foci can be approximated by Gaussian functions (Fig. 2.4). Doughnut-shaped foci around the intensity zero are well described by a parabola (see Section 1.2). Concerning the kinetics, a linear dependency of the number of activated/excited molecules from the applied intensity can be assumed for low activation/excitation light levels. In pulsed STED modalities,

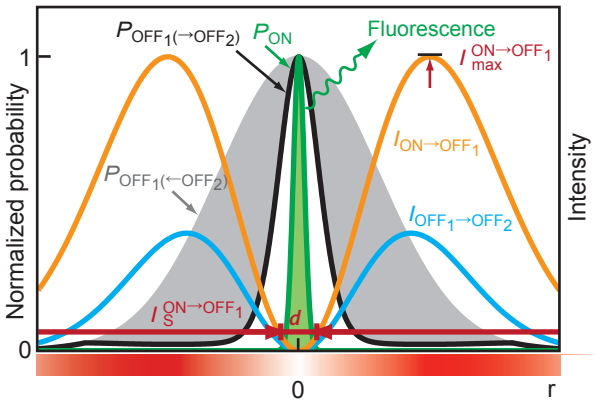

Figure 2.4: Normalized spatial distribution of probabilities *for a molecule to reside in OFF_1 after activation ($P_{OFF1(\leftarrow OFF2)}$); to reside in OFF_1 after the protective $OFF_1 \rightarrow OFF_2$ transition ($P_{OFF1(\rightarrow OFF2)}$); and to reside in the emitting ON state (P_{ON}) after joint action of both off-transitions (driven by the light intensity distributions $I_{ON(\rightarrow OFF1)}$ and $I_{OFF1(\rightarrow OFF2)}$) and excitation ($OFF_1 \rightarrow ON$, not shown). d: region where ON state can be assumed. r: distance from intensity minimum. Figure and caption reproduced from ref.* [70].

the number of molecules residing in the on-state during the action of the STED light decays with $P_{ON(\rightarrow OFF1)} = exp(-\zeta h_{STED}(x,y,z))$ with ζ being the ratio of the peak STED light intensity and the saturation intensity $I_S^{ON\rightarrow OFF1}$ [72;87]. Similarly, the deactivation process can be approximated with a single (or double) exponential decay [145]. P_{ON} describes the molecules remaining able to fluoresce after action of all light beams. Since all transitions are induced sequentially, P_{ON} is given by the product of the normalized spatial probability distributions of the individual transitions:

$$P_{ON} = P_{OFF1(\leftarrow OFF2)} \cdot P_{OFF1(\rightarrow OFF2)} \cdot P_{ON(\leftarrow OFF1)} \cdot P_{ON(\rightarrow OFF1)} \cdot P_{det}. \tag{2.1}$$

P_{det} accounts for the spatial detection probability. The multiplicative conjunction of transitions can be used to modify the shape of P_{ON} and therefore of the probed volume. Thereby, in protected STED, not only the lateral and axial dimensions of the main peak are constricted, but also side lobes and diffuse signal are suppressed. The latter can stem, for example, from switching background of the RSFP or from anti-Stokes excitation by the STED laser. The switching background results from the fluorescing molecules that cannot be transferred to OFF_2 by the deactivation light. In case of rsEGFP2, about 10% of all molecules depending on the applied deactivation power remain in the activated configuration [36]. Hence, the probability distribution of deactivation can be understood as $P_{OFF1(\rightarrow OFF2)} = P_{switching} + P_{non-switching}$. Inserting this relation into Equation 2.1 and factorising yield:

$$P_{ON} = P_{OFF1(\leftarrow OFF2)} \cdot P_{ON(\leftarrow OFF1)} \cdot \Big(P_{switching} P_{ON(\rightarrow OFF1)} + P_{non-switching} \cdot P_{ON(\rightarrow OFF1)} \Big) \cdot P_{det}. \tag{2.2}$$

This interplay shows that the fluorescence of the non-switched population is suppressed by the action of the STED transition $P_{\mathrm{ON}(\rightarrow\mathrm{OFF1})}$. *Vice versa* deactivation can counteract anti-Stokes excitation of the STED laser (not shown in the formula). In a similar manner, side-lobes stemming from imperfect coverage of the excitation PSF by a single doughnut focus can be jointly subdued. Hence, the MOST concept not only provides advantages in terms of fluorophore protection against bleaching, but concomitantly provides handles for enhancing the on/off contrast within subdiffraction-sized probe volumes. How these attributes effect the obtained super-resolved images will be dealt with in the following sections.

2.3 Results

The MOST concept was implemented in the form of protected STED on rsEGFP variants. Samples were obtained by expressing vectors encoding fusion proteins of the RSFP variant with proteins like, for example, keratin or vimentin. Both proteins assemble to filamentous cytoskeletal structures, which are stable over a timescale of minutes without showing significant spatial movement and protein turnover. This enables experiments where brightnesses of structures before and after the dedicated light exposures can be compared. To this end, a mircoscope was set up that allows activation, deactivation, excitation, and STED of green RSFPs (see Section 2.5.1). Although these four steps require in principle only four different beams and a detection pathway, additional features were implemented in the setup. For example further laser lines, a second detection channel as well as STED and deactivation beams for 3D superresolution imaging were added. Thereby, the choice of the STED light source is crucial. Here, a Raman-shifted fibre laser at 587 nm with broad pulses of up to 1.1 ns duration at a repetition rate of 20 MHz was utilized, securing both low peak powers and time for triplet relaxation[76]. Yet, not only the STED laser, but all technical and methodical parameters of the imaging system were optimized to enable best possible imaging conditions.

Of vital importance for the concept is that the various light-induced actions are sufficiently orthogonal to each other. In particular, this is of concern with the intense STED beam, which could lead to activation of previously deactivated molecules and thereby counteract any protective transfer to a second off-state. However, one can show for rsEGFP(N205S) and rsEGFP2 that first STED light does not lead to activation of molecules residing in OFF_2 and that second STED light alone does not lead to bleaching of activated or deactivated proteins (Figs. 2.5 and 2.6a-d). Moreover, when exposing deactivated rsEGFP2 molecules to excitation and STED light together, again no significant bleaching is observed in the subsequently recorded image of the re-activated molecules (Fig. 2.6e). In contrast, repeating this experiment with the same power settings on activated molecules, pronounced bleaching is observed (Fig. 2.6f). Experiments with the structurally unrelated fluorophores Dronpa(M195T)[146] (green-emitting)

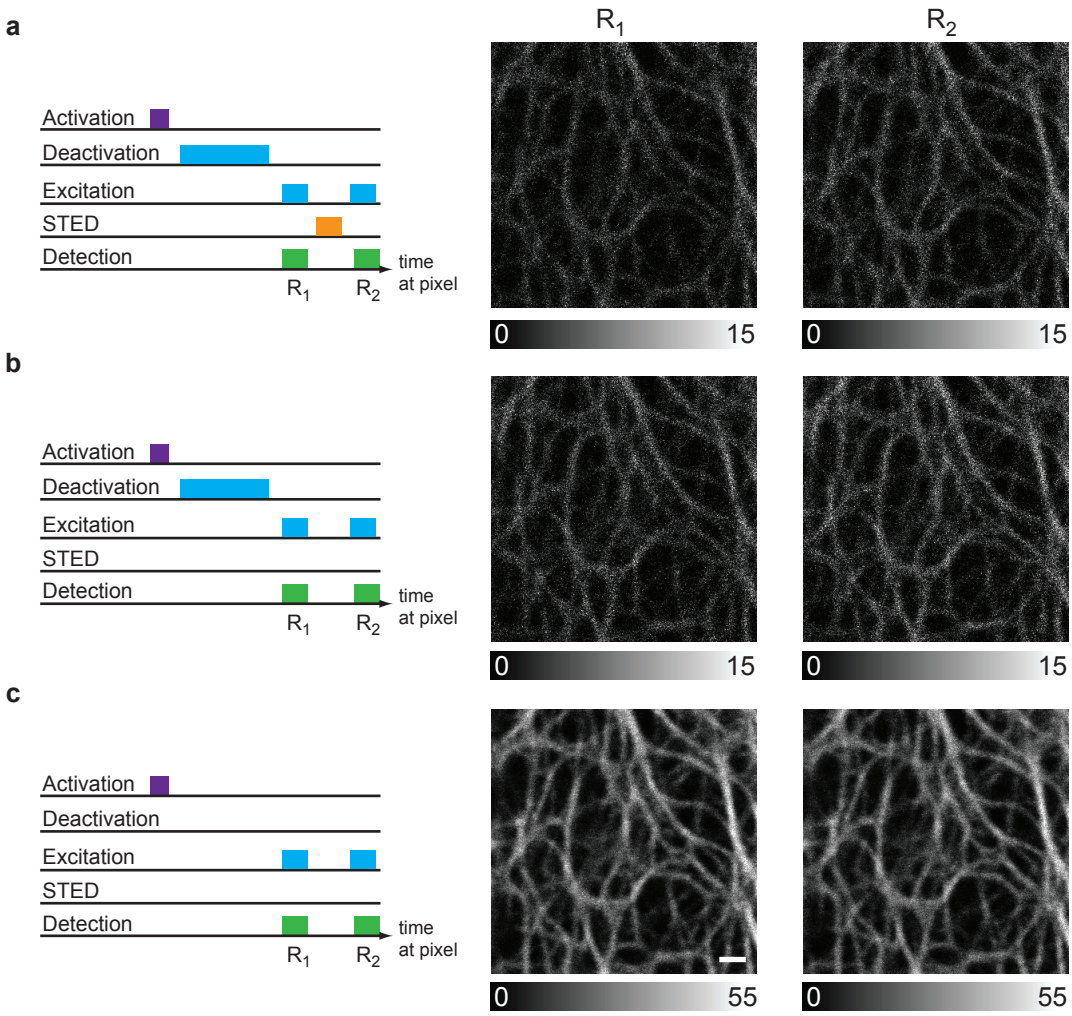

Figure 2.5: STED light does not activate proteins. *Confocal images recorded in two detection periods R_1 and R_2 while performing the indicated pixel sequences. (**a**,**b**) In both experiments, the two images are equally bright, demonstrating that the STED light applied in panel **a** after R_1 and before R_2 does not lead to significant activation of the proteins residing in OFF_2. (Proteins were first deactivated in the whole confocal volume.) (**c**) Omitting the deactivation light shows that the remaining fluorescence signal in the images of **a** and **b** correspond to switching background of about 4% (excitation power in c reduced by 75%). Sample: HeLa cell expressing keratin-rsEGFP(N205S). Scale bar: 1 µm. Data are raw. Figure reproduced from ref.[70].*

and rsCherryRev.1.4[39] (red-emitting) transfer to OFF_2 shows a similar protective effect (Fig. 2.7). Yet, the Citrine[98] descendant Dreiklang[35] exhibits no protective effect (data not shown) which is due to activation of molecules residing in OFF_2 by the STED light. These findings verify the general protective effect of specifically addressable off states.

Deactivation of rsEGFP(N205S) molecules does not interfere with the STED process (Fig. 2.8). This would be the case, for example, when the molecules would be transferred to a state which can absorb the STED light and eventually emit fluorescence. However, if anything, applying STED light on deactivated proteins suppresses signal from not properly deactivated proteins.

Since all transitions are sufficiently orthogonal, the sequence of light pulses per pixel for

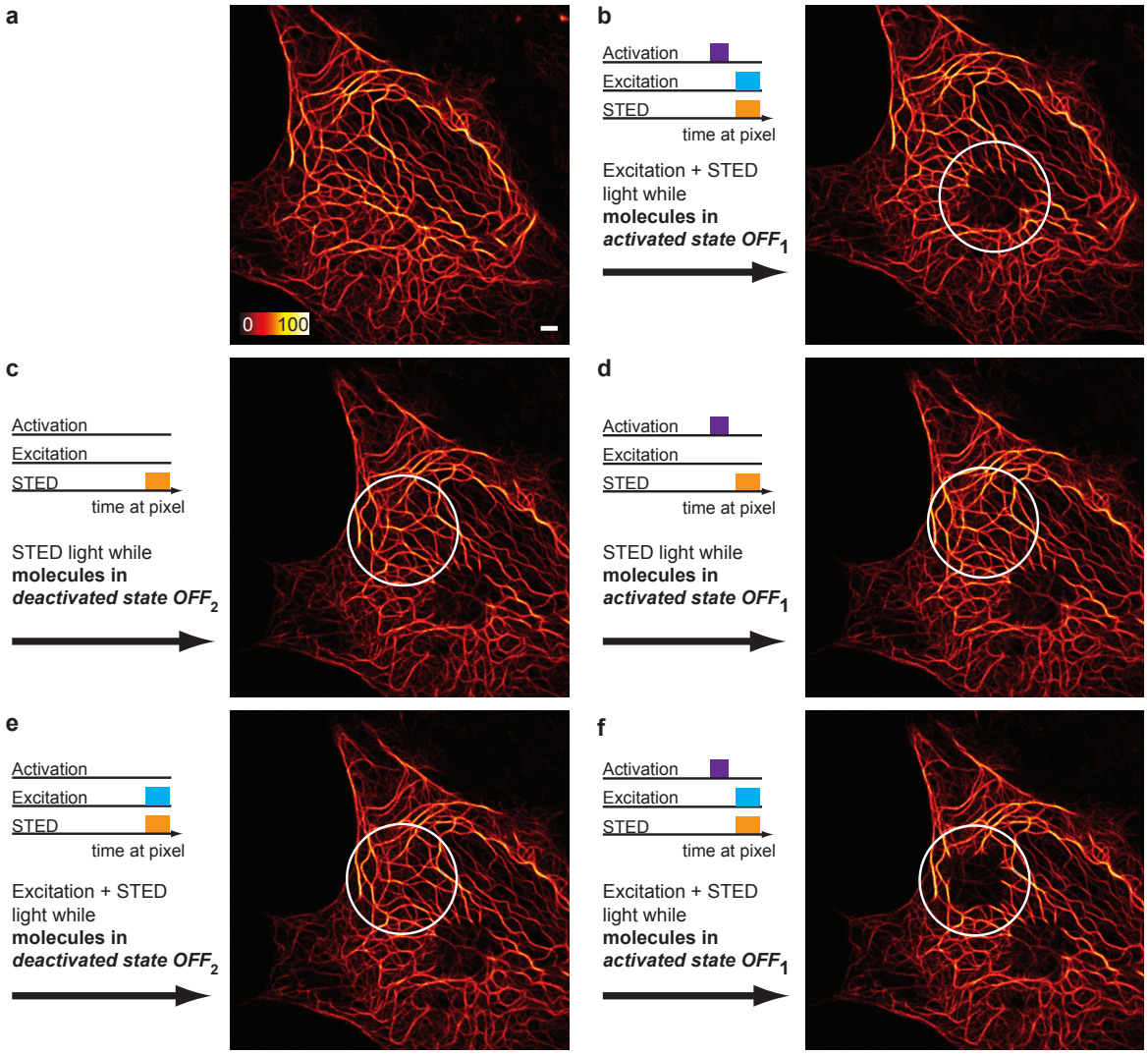

Figure 2.6: Protective effect of transfer to OFF_2. *Series of confocal images recorded after performing four scans with the indicated pixel sequences of the respective square region within the white circle. Deactivation (and activation) of proteins were performed by wide-field illumination of the whole cell. (**a**) Cell before exposure. (**b**) After regular STED imaging of activated proteins prominent photobleaching is observed. (**c**) Scanning deactivated molecules with STED light alone does not lead to bleaching. For the confocal image shown, the proteins were activated again. (**d**) Scanning activated molecules with STED light does not lead to bleaching as well. (**e**) After exposing deactivated molecules to excitation plus STED light, no bleaching is observed, proving that OFF_2 is protective. (**f**) Activating the molecules and repeating the experiment of **e** lead to prominent bleaching again. Sample: HeLa cell expressing keratin-rsEGFP2. STED power: 7 mW. Scale bar: 2 µm. Data are raw. Figure reproduced from ref.* [70].

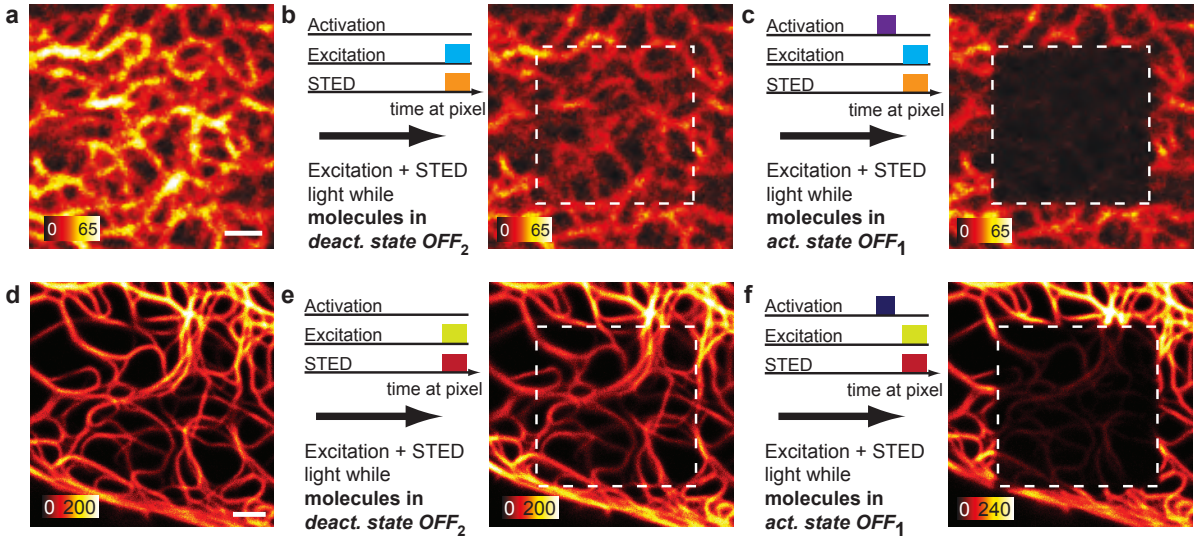

Figure 2.7: Protective effect demonstrated for further RSFP classes. *Series of confocal images recorded after performing several scans with the indicated pixel sequences of the respective square region (like in Fig.2.6). Deactivation (and activation) of proteins were again performed by wide-field illumination of the whole cell. (**a**-**c**) The green-emitting protein Dronpa(M159T) can be protected against STED light of 587 nm by transfer to a deactivated state OFF_2 with 488 nm light (activation: 405 nm, excitation: 488 nm). Sample: HeLa cell expressing keratin-Dronpa(M159T). (**d**-**f**) Likewise, the red-emitting RSFP rsCherryRev1.4 can be protected against STED light of 775 nm by transfer to a state OFF_2 with light of 590 nm (activation: 440 nm, excitation: 560 nm). Scale bars: 1 µm. Figure and caption reproduced from ref.* [70].

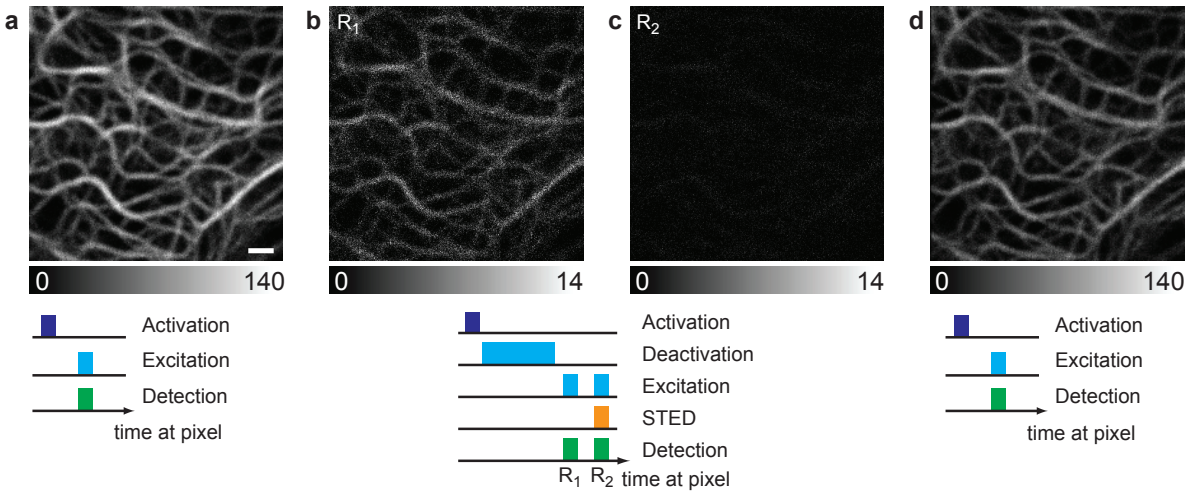

Figure 2.8: Protein switching and STED do not interfere. *Series of images of the same cell with the respective pixel sequences shown below the images. (**a**) Image without protein deactivation. (**b**) Deactivation of proteins by a regular and a doughnut-shaped focus switches off almost all proteins. (**c**) The remaining signal stemming from switching background can be suppressed by STED light applies as well as doughnut and Gaussian focus. (**d**) Subsequent experiment identic to **a** performed at the same region of the cell demonstrating low photo-bleaching despite STED light exposure. Sample: HeLa cell expressing keratin-rsEGFP(N205S). Scale bar: 1 µm. Figure reproduced from ref.* [70].

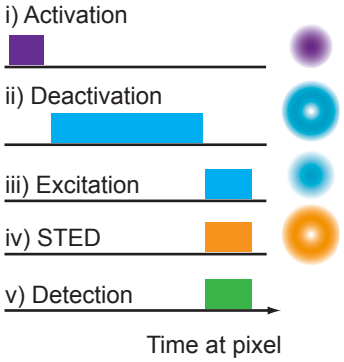

Figure 2.9: Protected STED sequence of light pulses *and fluorescence detection period at each scan pixel along with the focus geometries of the applied beams. Figure reproduced from ref.* [70].

protected STED nanoscopy can be defined: i) activation ($OFF_2 \rightarrow OFF_1$) with a circularly focused beam (405 nm, continuous wave (cw)), ii) deactivation ($OFF_1 \rightarrow OFF_2$) with a superimposed doughnut-shaped focus (488 nm, cw), iii) excitation ($OFF_1 \rightarrow ON$) with a circularly focused beam (488 nm, pulsed), and, simultaneously, iv) STED ($ON \rightarrow OFF_1$) with a doughnut-shaped focus (587 nm, pulsed) (Fig. 2.9). The specified wavelengths correspond to the emission wavelengths of the lasers mainly used in this study for the rsEGFP variants. Co-aligning the minima of the two doughnut-shaped focuses with the maxima of the regularly Gaussian focused beams defines a common subdiffraction area from where the emitted photons are detected. Of course, other geometries like an array of minima [38] are possible, too. While scanning this area over the sample, deactivation ensures that during illumination with STED light, the proteins residing in the doughnut crest are in OFF_2. Furthermore, at every new pixel molecules are again prepared in the activated state before confronting the intensity minima.

Employing the introduced pixel sequence on rsEGFP2 (Fig. 2.10), a similar protective effect is observed as in the experiment of Fig. 2.6, where all RSFP molecules of the cell were deactivated

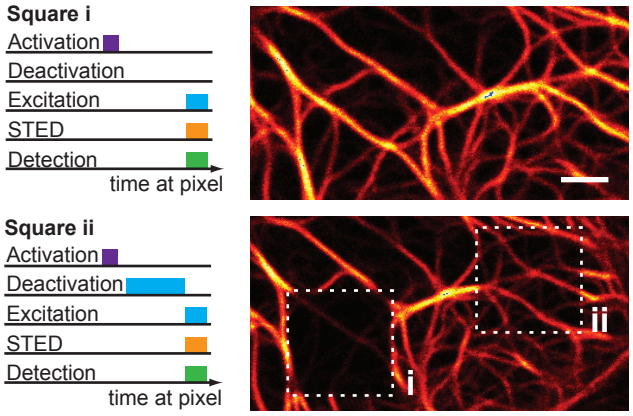

Figure 2.10: Protective transfer to OFF_2 in the pixel sequence. *Confocal images before (upper image) and after (lower image) performing conventional STED in square i and protected STED imaging in square ii (four scans per region). The protective effect is still present despite high switching rates. Sample: HeLa cell expressing keratin-rsEGFP2. Pixel size: 20 nm. Scale bar: 2 µm.*

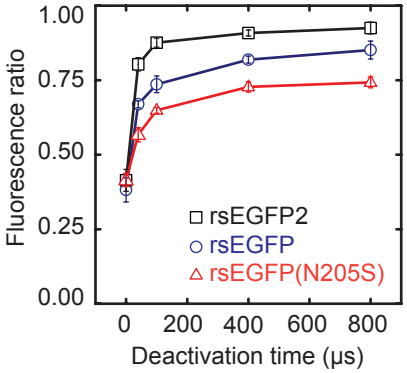

Figure 2.11: Protection of fluorophores as a function of deactivation time. *Intensity ratio of confocal images before and after scanning with the pulse sequence shown in Fig. 2.9. Deactivation times were 0 µs, 40 µs, 100 µs, 400 µs and 800 µs, respectively. Short deactivation times protect already significantly. Mean ± standard deviation from experiments in 10 cells. STED powers: rsEGFP2: 13 mW; rsEGFP: 5 mW, rsEGFP(N205S): 4 mW. Samples: HeLa cells expressing keratin-rsEGFP variants. Figure and caption reproduced from ref.* [70].

in one step. This indicates that rsEGFP2 provides a sufficiently low switching fatigue needed for protected STED imaging with high pixelation densities. This is not surprising, since rsEGFP2 was already successfully harnessed in RESOLFT nanoscopy, which demands even more switching cycles [36].

The protective effect for three rsEGFP variants was quantified by scanning image sections with different deactivation times within the protected STED pixel sequence. The shorter the deactivation time for a given deactivation power, the less molecules are transferred to OFF_2. The STED powers applied to the different RSFP variants were chosen such that the regions scanned without deactivation light were bleached to the same extent. The best protective effect is observed for rsEGFP2 (Fig. 2.11). About 90% of the fluorophores can be conserved under the chosen imaging conditions (13 mW STED light for 30 µs/20 nm pixel, one scan). In general, the protective effect rises quickly with the deactivation time as the fluorophores are first deactivated in the doughnut crest whereas the protection levels off for longer times. These observations confirm on one hand that the protection is most pronounced in the doughnut crests, since the molecules residing there are deactivated with a higher probability than those sitting close to the center or in the outer periphery of the deactivation doughnut. On the other hand, the data suggests that the deactivation time required for effective protection is much shorter than that needed for deactivation in typical RESOLFT imaging where this transition is used for creating superresolution.[1]

To summarize the results obtained so far, the fluorophores can be protected against STED light by transfer to a deactivated state. This was shown for several types of RSFPs and for

1 A typical RESOLFT pixel sequence for rsEGFP2 comprises about 40 µs activation, 400 µs deactivation and 20 µs read-out.

different imaging situations. Moreover, the protective effect is already significant at deactivation times ≤100 µs, suggesting that faster image recordings are possible with protected STED compared to classical RESOLFT nanoscopy.

2.3.1 Comparison with conventional STED and RESOLFT nanoscopy

To investigate, how the protective effect translates into imaging performance, image series with protected STED in comparison with conventional STED and RESOLFT microscopy were recorded. In general, bleaching of fluorophores strongly depends on the chosen imaging parameters like intensities, pixel dwell times and pixel sizes. For a useful comparison, the parameters of the methods were adjusted such that equal resolutions and brightnesses in the first image of each series were obtained. Thus, the STED power applied in the protected STED imaging scheme was lower than in the conventional STED scheme (1.5 mW compared to 7.6 mW), because part of the resolution increase was achieved already by the deactivation step. The obtained image sequences and the corresponding image brightnesses show that with protected STED significantly more recordings are possible than with conventional STED (Fig. 2.12). About 90% of the initial image brightness can be preserved after ten recordings with protected STED, whereas the corresponding STED image is already bleached to ~25% at that point. The brightness course of the protected STED image series almost follows the one of the RESOLFT series, indicating that the detrimental effect of the STED light is suppressed almost completely and that the remaining fluorophore bleaching is dominated by the fatigue of the switching processes. To validate that the fluorophore conservation in protected STED can really be attributed to protective transfer to OFF_2, analogue experiments with specific parameter variations were carried out (Figs. 2.13 and 2.14). However, neither shortening the

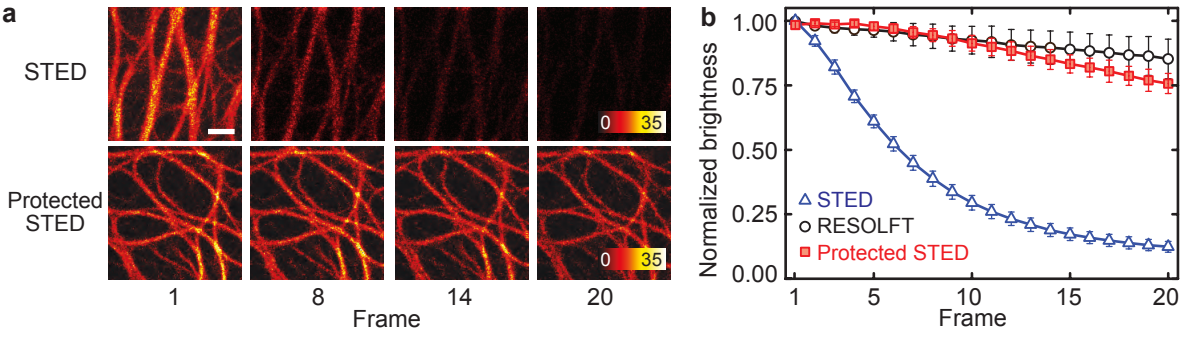

Figure 2.12: Reduced bleaching in protected STED imaging. *(**a**) Image series recorded with STED (7.6 mW STED power) and protected STED (350 µs deactivation, 1.5 mW STED power) with similar resolution and brightness in the first frames. (**b**) Image brightness as a function of frame number normalized to the first frame for STED (blue triangles), protected STED (red squares), and RESOLFT (black circles, 400 µs deactivation). In protected STED bleaching by the STED laser is almost completely suppressed. Sample: HeLa cells expressing keratin-rsEGFP2. Mean ± standard deviation of measurements in 10 cells. Scale bar: 1 µm. Figure and caption reproduced from ref.[70].*

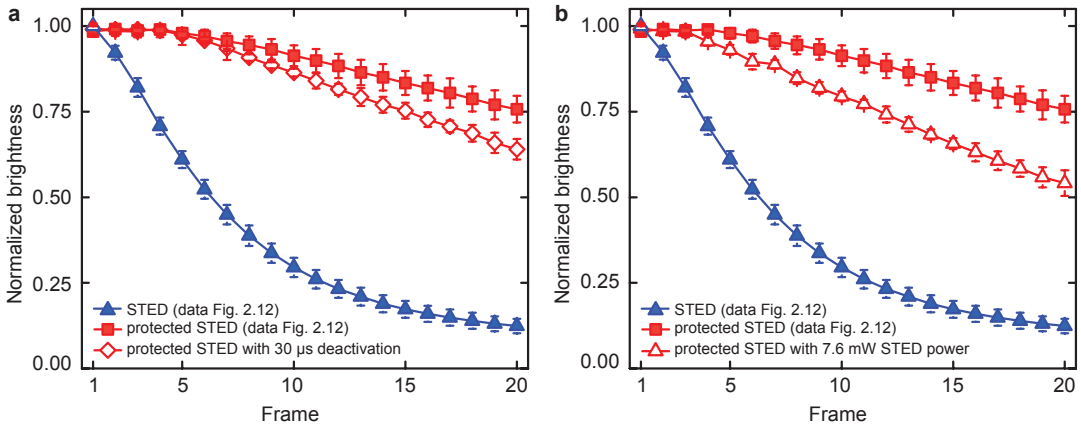

Figure 2.13: Robustness of protective effect against parameter variations. *(**a**) Repeated protected STED imaging carried out like in Fig. 2.12 with reduced deactivation time (30 µs as opposed to 350 µs). To keep image brightness and resolution approximately constant, STED power was increased (from 1.5 mW to 3.3 mW). Protective effect is still present. (**b**) Protected STED imaging with the same STED power (7.6 mW) as used in the STED series of Fig. 2.12 demonstrating that the the lower STED power applied in the previous experiment is not responsible for the protective effect. Sample: HeLa cells expressing keratin-rsEGFP2. Figure and caption reproduced from ref.[70].*

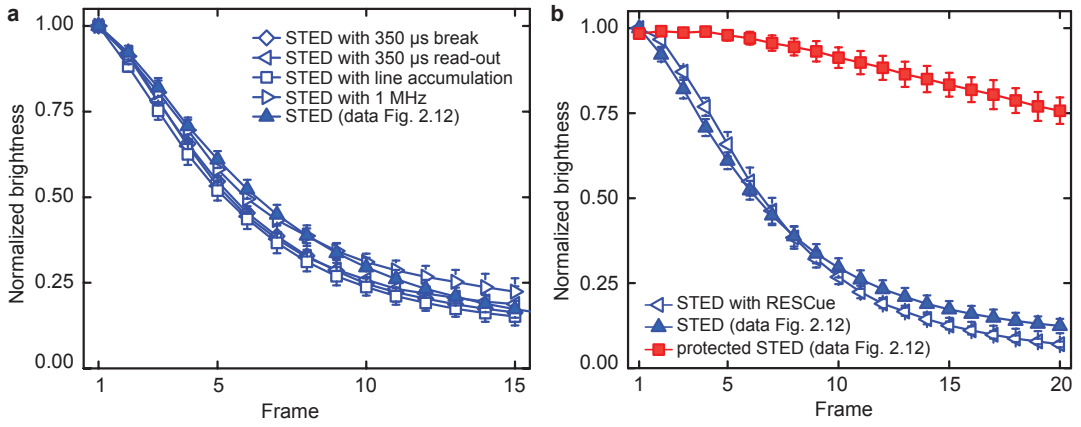

Figure 2.14: STED parameter variations unable to decrease bleaching. *STED image series carried out similar to experiments in Fig. 2.12 trying to mimic the protective effect of deactivation by: (**a**) introducing a break as long as the deactivation period in protected STED ('STED with 350 µs break', other parameters were kept constant); stretching the read-out time with correspondingly reduced excitation power ('STED with 350 µs readout'); dividing and stretching the pixel dwell time in parts by scanning every y-line four times (in total 200 µs readout time per pixel with reduced excitation and constant STED powers, 'STED with line accumulation'); reducing the repetition rate of excitation and STED light 1 MHz (STED pulse energy kept constant, 'STED with 1 MHz') and (**b**) applying RESCue-STED with lower and upper thresholds (excitation and STED parameters were kept constant, details are given in the methods section). All variations failed to significantly reduce bleaching. Sample: HeLa cells expressing keratin-rsEGFP2. Figure and caption reproduced from ref.[70].*

deactivation time (30 µs instead of 350 µs) nor increasing the STED power to the level of the conventional STED series (7.6 mW instead of 1.5 mW) substantially decrease the protective effect (Fig. 2.13). Likewise, attempts to reduce the bleaching in conventional STED imaging by introducing a break before read-out, stretching or dividing the read-out step and by reducing the repetition rate of the STED and excitation laser failed (Fig. 2.14a). All these measures tend to decrease the accumulation of molecules residing in non-emissive, long-lived triplet states[75]. However, obviously, the imaging conditions and the choice of parameters were already exhaustively optimized in this respect. Also, the RESCue (REduction of State transition Cycles) technique[83] was applied to conventional STED (Fig. 2.14b). In RESCue, lower and upper thresholds of count rates set at fractions of the read-out time per pixel define whether the excitation and STED lasers are shut off before the full read-out time is completed. For example, lasers are blocked earlier at regions without labeled structures where lower thresholds are not reached, and at bright spots where upper thresholds are reached. In the former case, the pixel values are set to zero. In the latter, they are extrapolated to the value which would have been measured with the full exposure time. Consequently, the light dose impinged on the cell and the fluorophores is reduced. However, it is not possible to substantially decrease the bleaching in conventional STED imaging of rsEGFPs by including both lower and upper RESCue thresholds. This can be explained by the fact that RSFP-labeled samples are typically too dark for setting effective and statistically secured thresholds and therewith for avoiding the introduction of image artifacts like dark pixels within labeled regions. In summary, protected STED produces significantly more super-resolved images than conventional STED and is robust against parameter variations.

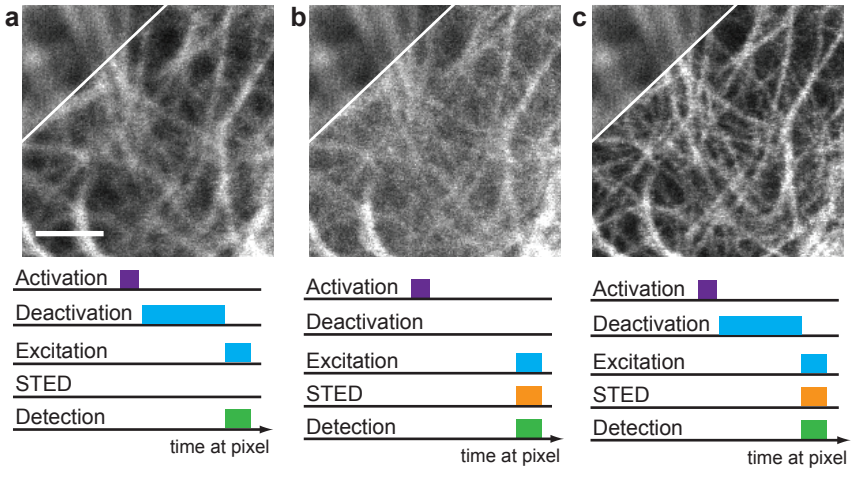

Figure 2.15: Joint contribution of deactivation and STED to subdiffraction image formation. *Imaging of rsEGFP(N205S) with resolution increase solely by deactivation (panel* ***a****) and solely by STED (panel* ***b****), each with parameters not sufficient to resolve the actin network. Only when both beams with the same parameters are applied together (panel* ***c****), the actin cytoskeleton is clearly resolved. Sample: CV-1 cell expressing actin chromobody-rsEGFP(N205S). Scale bar: 1 µm. Figure and caption reproduced from ref.[70].*

In the above protected STED experiments, a substantial part of the resolution increase was achieved by the deactivation process. The protected STED scheme allows, to a certain extent, to freely choose whether the resolution is mainly generated with the deactivation or the STED doughnut beam. This is due to the multiplicative conjunction of the sequentially induced optical transitions[3;25] (Section 2.2.1). This applies both to the on-switching sequence $OFF_2 \rightarrow OFF_1 \rightarrow ON$, and even more to its off-switching counterpart $OFF_1 \rightarrow OFF_2$ and $ON \rightarrow OFF_1$, respectively. A well-resolved image of the actin network of a CV-1 cell is obtained by employing both off-transitions with parameters, which are insufficient to resolve the network, when either only deactivation or STED light is applied (Fig. 2.15). Consequently, bleaching in protected STED mode is reduced both by protection of the fluorophores through transfer to OFF_2 and by reduced STED power requirements due to joint contribution to subdiffraction resolution formation. Furthermore, the multiplicative conjunction leads to improved on/off state contrast. The diffuse background in the STED image of Figure 2.15b stems from insufficiently silenced fluorophores in the outer regions of the confocal excitation/detection PSFs. This becomes evident as well in measurements of a thin layer of filaments by STED and protected STED with z-doughnuts (Fig. 2.16). The 'background' observed in case of conventional STED is strongly reduced in the protected STED image. However, the signal to background ratio in conventional STED microscopy is typically better with more stable dyes. In protected STED, different temporal and spatial dependencies of the deactivation compared to the STED process and the multiplicative conjunction of the two, jointly suppress signal background (Section 2.2.1). By the same token, protected STED solves the in RESOLFT microscopy frequently observed problem of switching background of RSFPs (Fig. 2.8).

To evaluate how this synergism affects the imaging performance of protected STED compared to conventional STED and RESOLFT nanoscopy, images of the actin network of living CV-1 cells were recorded (Fig. 2.17). Structures were labeled by an actin chromobody (AC)-rsEGFP(N205S)

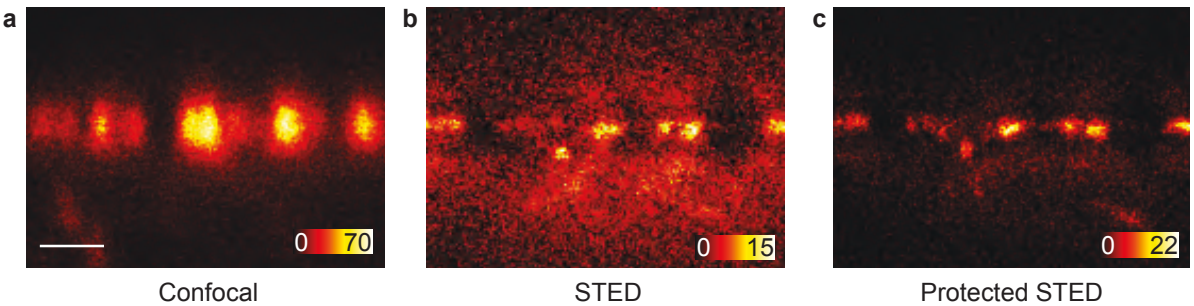

Figure 2.16: Improved spatial state contrast in protected STED. *(**a**) Confocal xz-image of the bottom side of a cell. (**b**) STED imaging of the same cell with a z-doughnut. (**c**) Protected STED image recorded with z-doughnuts both for deactivation and STED. Signal-to-background ratio in the protected STED image is significantly enhanced compared to conventional STED. Sample: HeLa cell expressing keratin-rsEGFP2. Scale bar: 1 µm.*

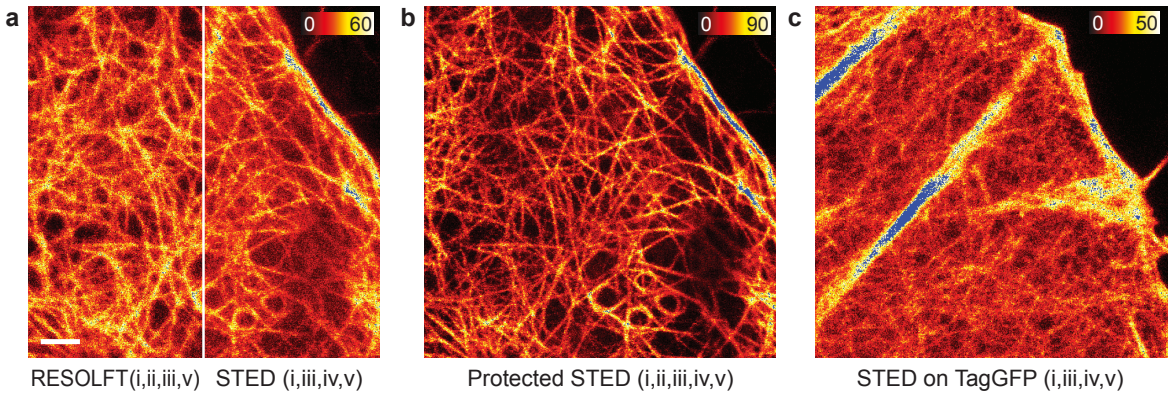

Figure 2.17: Improving contrast with protected STED. *Images of rsEGFP(N205S) highlighting actin recorded with* **a***)RESOLFT and conventional STED nanoscopy (RESOLFT: 2.5 ms deactivation; STED: 11.6 mW STED power).* **b** *In the protected STED image of the same region, sharp and clearly resolved filaments are standing out against a low background (1.5 ms deactivation, 6.7 mW STED power). (***c***) Imaging of non-photoswitchable GFP with conventional STED nanoscopy yields similar results (STED power: 10.5 mW). Sample: CV-1 cells expressing actin chromobody-rsEGFP(N205S) and -TagGFP, respectively. Raw data. Scale bar: 1 µm. Figure reproduced from ref.* [70].

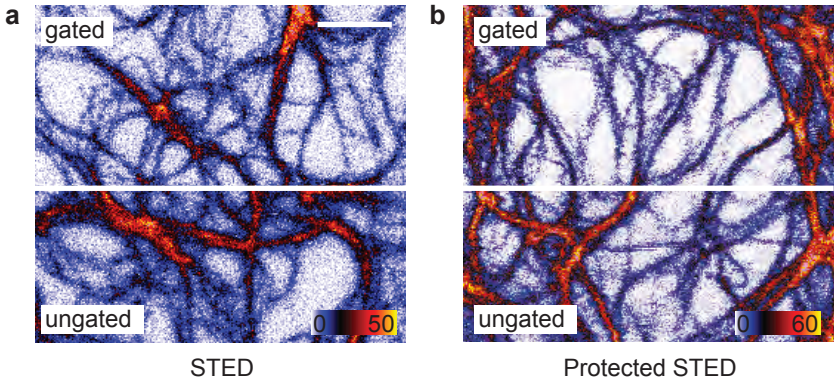

Figure 2.18: Minor effect of time gating in protected STED nanoscopy. *(***a***) STED image recorded with (upper half) and without (lower half) nanosecond time-gating showing much better demarcated filaments in the gated region. (***b***) Same experiment with protected STED exhibiting only a minor effect of time gating. Sample: HeLa cell expressing vimentin-rsEGFP2. Raw data. Scale bar: 1 µm. Figure reproduced from ref.* [70].

construct, which is a fusion of an actin camelid antibody with rsEGFP(N205S). The chromobody exhibits a certain degree of turnover, *i.e.* active binding and unbinding from the target, but it has a higher affinity to actin than the Lifeact marker [119], and is not toxic in contrast to stainings with phalloidin. Other than the STED and RESOLFT counterparts, the protected STED image in Fig. 2.17b is characterized by sharply demarcated subdiffraction-sized structures and a high signal-to-background ratio. Both STED and protected STED images were time-gated on the nanosecond scale [147]. However, the gating effect is higher in conventional STED nanoscopy, since the rejected signal stems from the doughnut region, which is largely deactivated in case of protected STED (Fig. 2.18). Similarly, when protected STED is applied to image the vimentin cytoskeleton of HeLa cells highlighted by rsEGFP2 (Fig. 2.19), sharp filaments with full widths

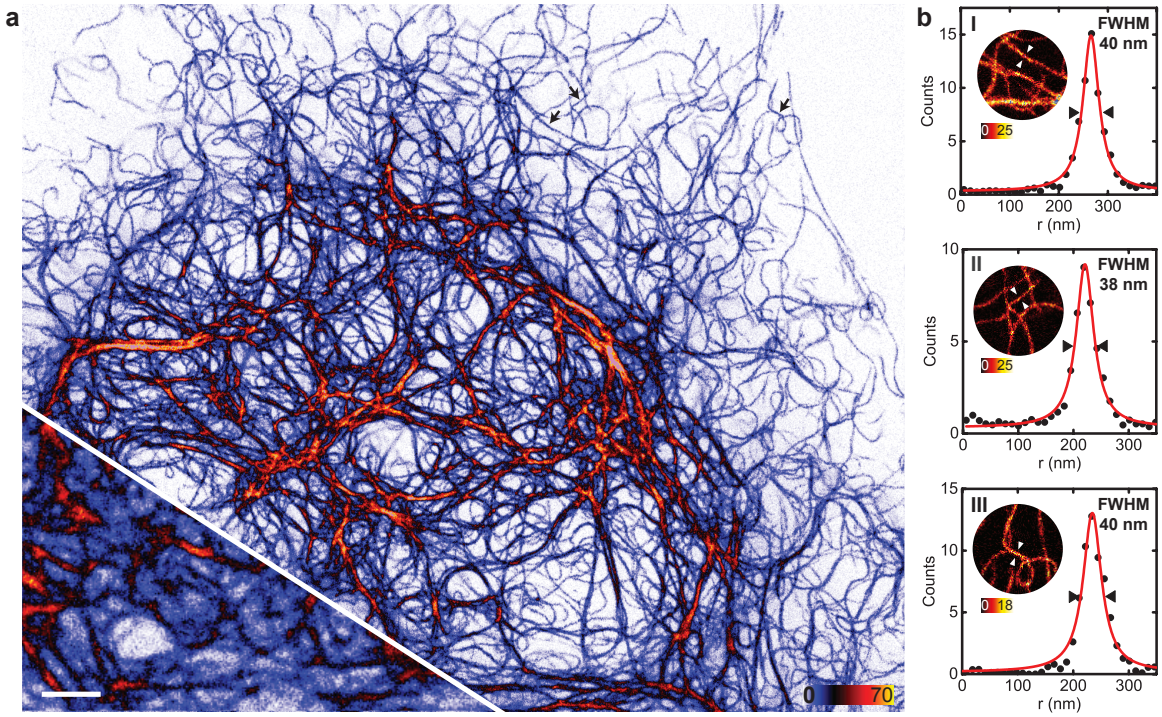

Figure 2.19: Protected STED imaging with rsEGFP2. *(**a**) Protected STED image of a living HeLa cell. Confocal comparison is shown in the lower left corner. The extended colour look-up-table visualizes the signal dynamics in the image thus revealing filaments that are thin and faint amid bright fibre bundles. Deactivation time: 350 µs, STED power: 7.6 mW. Data smoothed with 1.2 pixel wide Gaussian. Scale bar: 2 µm. (**b**) 10 pixel wide line profiles drawn on raw data of the vimentin filaments marked by arrows in panel **a** and by arrowheads in the respective diagram in **b**. Lorentzian fits yielded FWHM of 39.7±1.3 nm, 38.4±1.7 nm, 40.3±1.9 nm at signal-to-background ratios of ~49, 29, 87 for filaments I-III, respectively. Diameter of close-ups: 2.1 µm. Sample: HeLa cell expressing vimentin-rsEGFP2. Figure reproduced from ref.* [70].

at half maxima (FWHM) of ~40 nm and signal-to-background ratios of sometimes >100 are obtained. The blue to white colour look-up table better visualizes the signal dynamics in the image than the standard fire table, revealing filaments that are thin and faint amid bright fiber bundles. In summary, the synergistic action of the two off-transitions enhances state contrast, which translates into high resolution, superior signal-to-background ratio, and enhanced overall image contrast.

Depending on the specific sample and the imaging task, parameters like beam powers, dwell times and pixel size are chosen differently. The limited number of available fluorescence photons per area can be exhausted in a few or spread over a large number of frames. Accordingly, the recording of the vimentin network (Fig. 2.19) was acquired with different parameters compared to the keratin images series (Fig. 2.12). However, low bleaching rates and high level of details can be achieved at the same time (Fig. 2.20). Again, protected STED produces sharper images than the conventional RESOLFT technique.

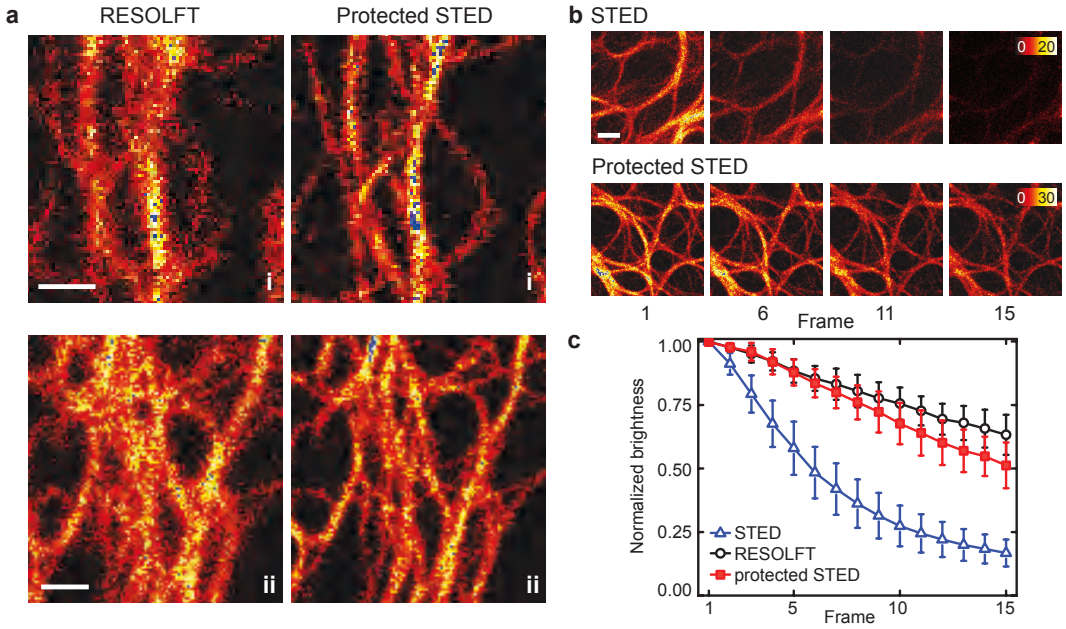

Figure 2.20: Protected STED enables high contrast and low bleaching at the same time. *(**a**) RESOLFT and protected STED images of the same two regions in a HeLa cell. Filaments are better demarcated in the protected STED data. (**b**) Image series recorded with conventional STED, protected STED and RESOLFT. The latter two were recorded with the parameters used in **a**. Again, protected STED produces better images than RESOLFT at low bleaching rates. RESOLFT: 400 µs deactivation with 8 µW. Protected STED: 350 µs deactivation with 4.4 µW, 5.1 mW STED light. Conventional STED: 10 mW STED light. Figure adapted from ref.* [70].

2.3.2 Application of protected STED nanoscopy

3D superresolution imaging

The pendant of the doughnut beam for superresolution generation in lateral directions is the bottle beam or 'z-doughnut' [28;148] for the axial direction (Fig. 2.29 in the Method section). It is generated by inserting an annular phase mask with appropriate diameter and thickness into the beam path. The activation and excitation foci were superimposed with each an xy- and a z-doughnut for deactivation and STED. Therewith, 3D protected STED imaging of the keratin cytoskeleton of a living HeLa cell is possible with ~75 nm lateral and ~110 nm axial resolution (Fig 2.21). The voxel size of the datasets in panel e of the figure was 35x35x40 nm^3 corresponding to 44 xz-slices spaced by 35 nm in the y-direction. Such a high pixelation density is not possible with conventional 3D STED of fluorescent proteins, since very low bleaching rates are demanded.[1]

The 3D protected STED scheme was also employed for making thin optical slices of the cortical actin network of living CV-1 fibroblasts, which were labeled again with the actin

1 The RESCue technique enables high pixelation densities for conventional 3D STED imaging, but it yields the best results only with bright and photostable synthetic fluorophores.

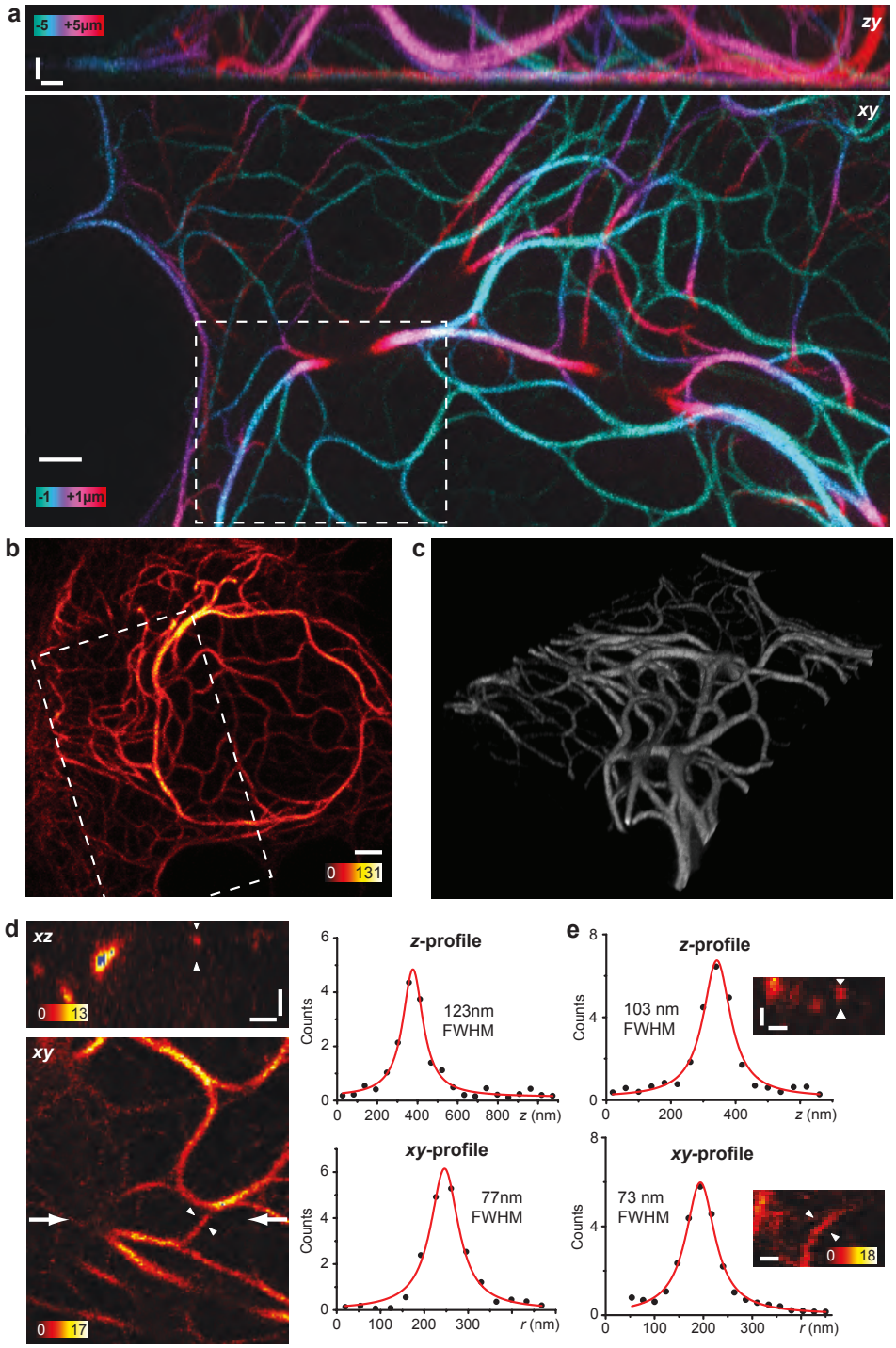

Figure 2.21: 3D superresolution imaging with protected STED. *(**a**) 3D superresolved arrangement of keratin filaments in a living HeLa cell imaged with protected STED (deactivation and STED both xy- and z-doughnuts). The same dataset is shown in the xy-view (large panel) and in zy (small panel), whereby the respective third axis is colour-coded. Voxel size: 35x35x55 nm^3 (xyz). Scale bars: 1 µm for xy-view, 500 nm for zy-view. (**b**) Maximum intensity projection of six z-slices of the same cell recorded with diffration-limited resolution. Dashed rectangle denotes the region imaged in panel **a**. Scale bar: 2 µm. (**c**) 3D reconstruction of the protected STED dataset in panel **a**. (**d**) Single xz- and xy-slices of the volume indicated by the dashed rectangle in panel **a**. The large arrows within the xy-section indicate the position of the xz-slice. Diagrams show line profiles and corresponding fits to Lorentzians of the same filament indicated by the arrowheads in the images. Scale bars: 500 nm. (**e**) Line profiles of a single filament shown in the insets from a measurement with denser sampling in the z-direction. Voxel size: 35x35x40 nm^3. Scale bars: 200 nm. Sample: HeLa cell expressing keratin-rsEGFP2. Figure adapted from ref.[70].*

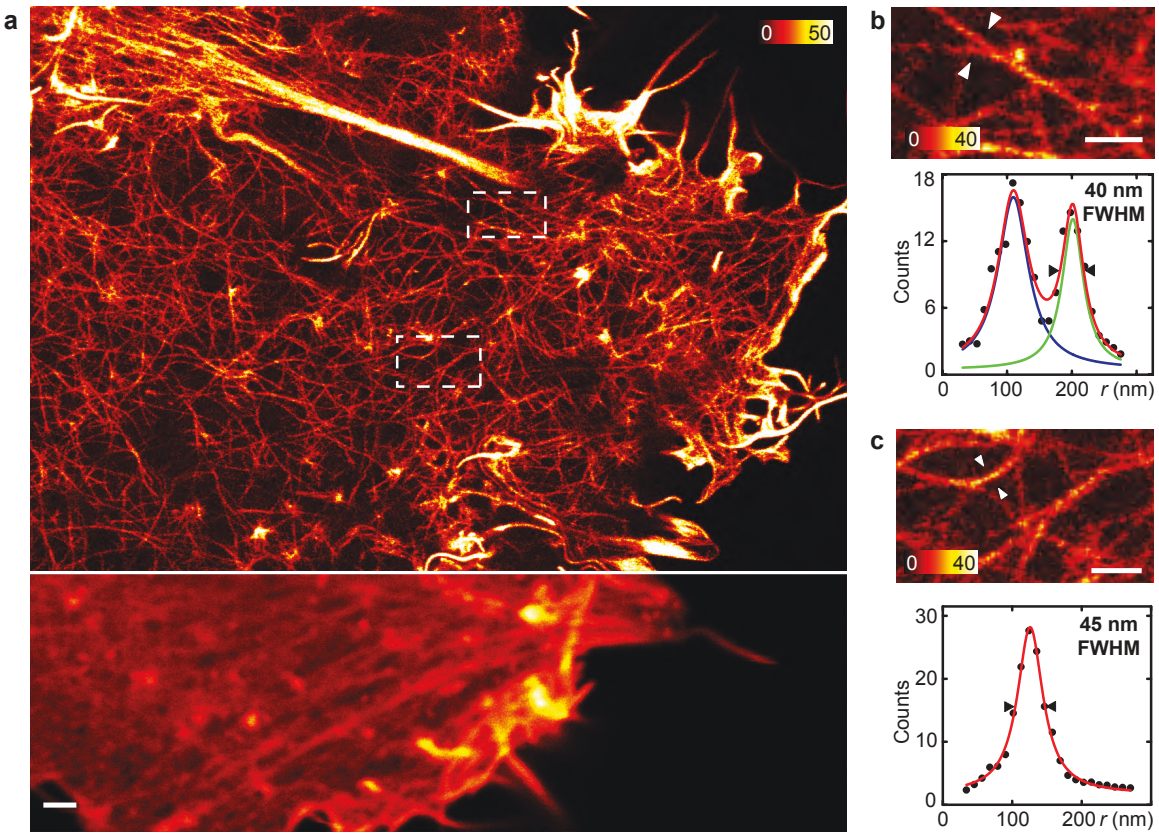

Figure 2.22: Protected STED imaging with rsEGFP(N205S). *(**a**) Protected STED image along with a confocal comparison of a living CV-1 cell expressing actin chromobody-rsEGFP(N205S). The image corresponds to a single optical slice of the cell of subdiffraction thickness (<150 nm) recorded with all four doughnuts. Image smoothed with a 1.3 pixel wide Gaussian. Scale bar: 1 µm. (**b**,**c**) Zoomed views of the regions indicated in **a** and corresponding line profiles of filaments marked by the arrowheads. (**c**) A double Lorentzian fit yielded 57±8 nm and 40±7 nm FWHM and 90.5 nm peak spacing. Scale bars: 500 nm. Figure reproduced from ref.[70].*

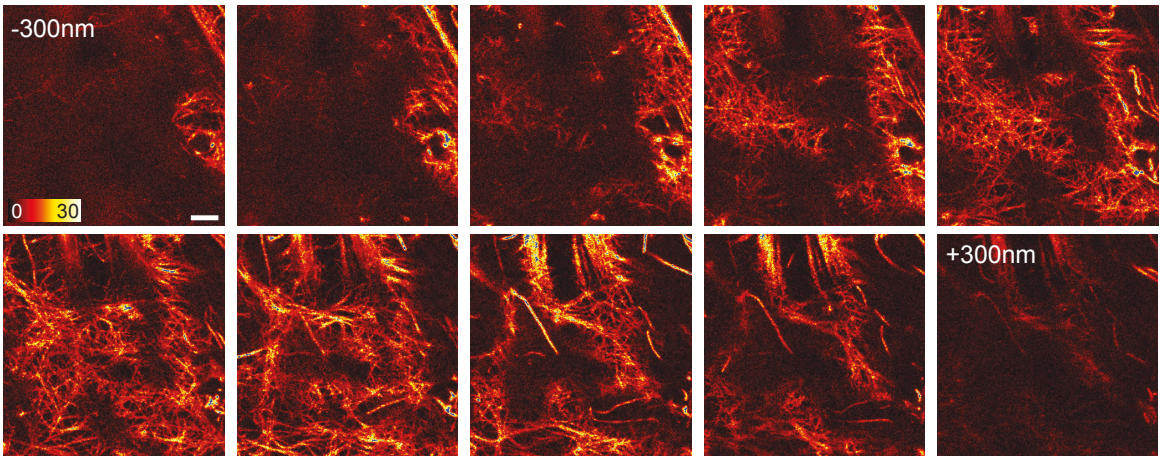

Figure 2.23: 3D protected STED imaging of the cortical actin network. *Image stack recorded in a living CV-1 cell expressing AC-rsEGFP(N205S). Imaging parameters were identical with dataset in Fig. 2.22. The axial resolution is able to visualize structural differences between the individual slices separated by 61 nm. Voxel size: 20x20x61 nm^3 (xyz). Scale bar: 1 µm. Figure reproduced from ref.[70].*

chromobody-rsEGFP(N205S) (Fig. 2.22). The recording shows stress fibres fanning out into a series of fine actin filaments, which can be followed up to the cell periphery. Line intensity profiles of filaments have FWHM of ~45 nm. The branching strands in Fig. 2.22b exhibit nearly full modulation at 90 nm distance. The relatively high fluorescence background stemming from out of focus layers of the dense network as well as from free marker molecules and labeled actin monomers, can be suppressed by the joint action of the two off-transitions. Consequently, high signal-to-background ratios of ~16 and ~30 were obtained for the profiles shown; at the cell periphery the ratio is ~10 times higher. Recording multiple of those z-slices with a spacing of only 61 nm nicely visualizes the three-dimensional complexity of this dense network supporting and modulating the plasma membrane (Fig. 2.23).

Capturing cellular dynamics with protected STED

For visualizing cellular dynamics at the time scale of milliseconds, pixel dwell times of coordinate-targeted imaging schemes must be as short as possible. However, the activation and especially the deactivation time cannot be reduced at will by increasing the respective beam powers. The kinetics of the deactivation processes change at higher power levels leading to an increased switching background, which lowers the overall image quality (Fig. 2.24a). In protected STED, this problem can be counteracted by generating most of the resolution increase with the STED

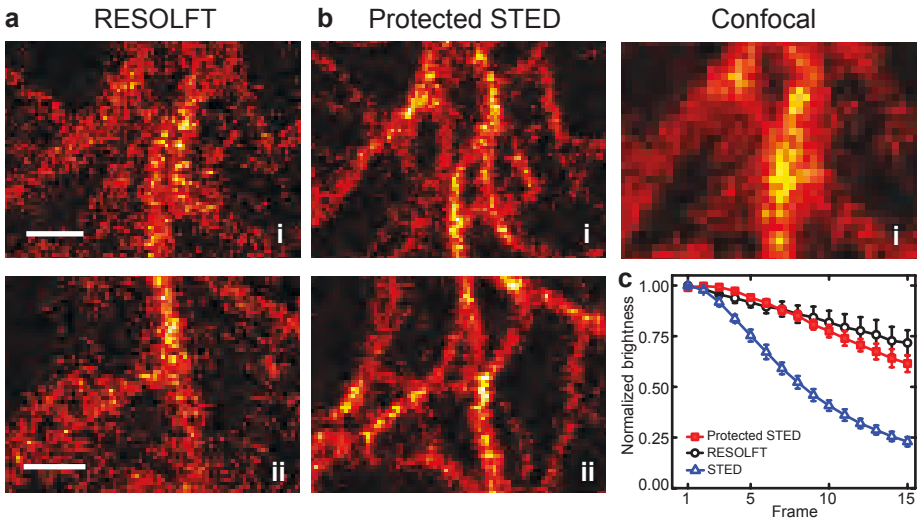

Figure 2.24: Protected STED enables pixel dwell times of sub-100 µs. *(**a**) RESOLFT images of two regions i and ii with an overall pixel dwell time of 80 µs (deactivation with 41.5 µW for 50 µs). (**b**) Protected STED images of the same regions with 95 µs/pixel (deactivation with 8.9 µW for 30 µs, STED with 5.1 mW) showing sharper filaments and revealing much more details than the RESOLFT images. Structures slightly changed due to movement of the living cell. Data smoothed. Scale bar: 500 nm. (**c**) Normalized image counts as a function of frame number for STED, RESOLFT, and protected STED recordings with the same parameters. STED parameters were chosen to yield images of similar resolution and brightness compared to protected STED (pixel dwell time 60 µs and 7.9 mW STED power). Sample: HeLa cells expressing vimentin-rsEGFP2. Figure reproduced from ref.[70].*

process. In fact, much lower deactivation powers (<10 µW) than in similarly fast RESOLFT pixel sequences (~40 µW[36]) can be applied, because the deactivation step can be specifically optimized for fluorophore protection. By this, protected STED can be realized with pixel dwell times as small as 95 µs, whereas 30 µs are allotted to the activation step, 30 µs to the deactivation and 30 µs to excitation and STED (additional 5 µs are introduced for laser synchronization) (Fig. 2.24b). The pixel dwell time still includes 10 µs rise time of the activation laser. The obtained protected STED images show much more details than the respective RESOLFT equivalents of the same regions. Moreover, speeding up the pixel dwell time retains the protective effect and reduces bleaching compared to similarly fast recorded STED image series (Fig. 2.24c).

Protected STED with short pixel dwell times was applied to record movies of the endoplasmatic reticulum and of peroxisomes in living cells, consisting of 500 and 70 frames, respectively (Supplementary Movie 2 and 3 in ref.[70]). Recording the peroxisomes in a 5x10 µm^2 area took ~4.5 s/frame. This corresponds to a frequency of 2.3 Hz for a 2x2 µm^2 large area.

Dual-colour nanoscopy with protected STED

Several multicolour superresolution schemes harnessing protected STED are conceivable. Perhaps the most straightforward, but rather ungainly option is the combination of protected STED of an rsEGFP and conventional STED of a yellow fluorescent protein for (quasi-)simultaneous dual-colour nanoscopy. This combination has the advantage of employing a single STED line for both markers, similar to the scheme proposed by Tønnesen *et al.*[143]. To this end, the microscope setup was upgraded by a 516 nm pulsed laser and a second APD for exciting and

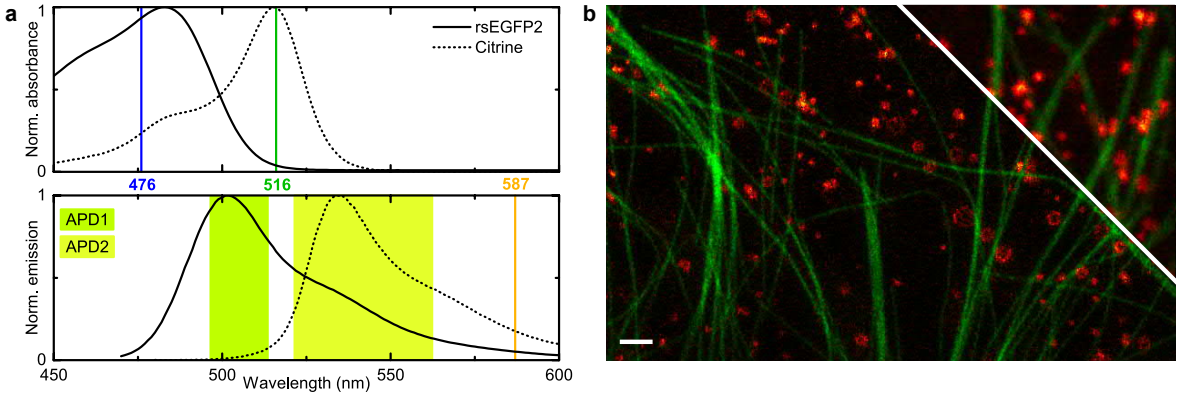

Figure 2.25: Dual-colour nanoscopy. *(**a**) Upgraded spectral scheme for dual-colour imaging. Diagrams show normalized absorption (upper panel) and emission spectra (lower panel) of rsEGFP2 and Citrine, respectively, along with the excitation and STED wavelengths. Activation and deactivation wavelengths are omitted. Detection windows are indicated by the coloured areas. (**b**) Quasi-simultaneous imaging of endosomes by protected STED (rsEGFP(N205S), fire) and microtubules by conventional STED (Citrine, green). Confocal data is shown on the right. Sample: CV-1 cell expressing Rab5a-rsEGFP(N205S) and Map2-Citrine. Data linear unmixed and smoothed. Scale bar: 1 µm. Figure adapted from ref.*[70].

detecting Citrine[149], respectively (Fig. 2.25a). Citrine is an improved version of EYFP. The 516 nm excitation step was added at the end of the protected STED pixel sequence. The 488 nm excitation laser for rsEGFP was replaced by a 476 nm laser to reduce unintended excitation of Citrine during the protected STED recording. Remaining excitation and detection cross-talk could be removed by linear unmixing[150;151]. Yet, Citrine was still continuously excited during the (curtailed) deactivation step of the rsEGFP, which is a major drawback of this implementation. Nonetheless, it was possible to record endosomes and its association with microtubules (Fig. 2.25b and Supplementary Movie 4 in ref.[70]). Endosomes were labeled by Rab5a-rsEGFP(N205S) and microtubules by Map2-Citrine. Protected STED was able to resolve the ring-like structure of the endosomes. By time-lapse imaging over 90 frames with fast protected STED parameters, individual endosomes could be observed being transported along microtubules. In this way, cargo is shuttled through the cell which plays a crucial role for diverse processes such as neuronal signaling, protein secretion, and cell cycle regulation.

Imaging in living brain tissue

Presently, two-photon (2P) excitation microscopy[2] is utilized to image micro- or even millimeter deep in living tissue. Employing red to near-infrared instead of visible light reduces light scattering and therefore tissue penetration. Moreover, since high photon densities are required to render simultaneous absorption of two photons probable, the two-photon (2P) excitation

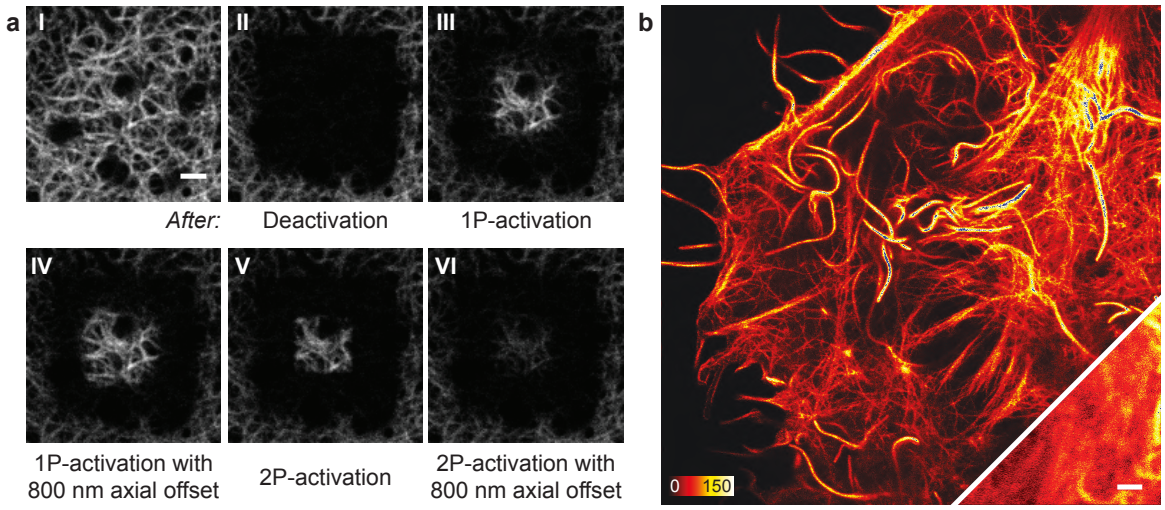

Figure 2.26: Protected STED with two-photon activation. *(**a**) Comparison between one-photon (1P) activation at 405 nm and two-photon (2P) activation at 800 nm. The image series shows confocal scans of the same region after applying different activation patterns as described below the respective panel. Except for the reference image in panel I, no activation light during recording these images was applied. The experiment illustrates selective photoactivation of molecules by 2P compared to 1P activation. Sample: HeLa cell expressing keratin-rsEGFP(N205S). Scale bar: 2 µm. (**b**) Raw protected STED image of a living CV-1 cell recorded with 3D subdiffraction resolution and 2P activation. Sample: CV-1 cell expressing AC-rsEGFP(N205S). Scale bar: 1 µm. Figure adapted from ref.[70].*

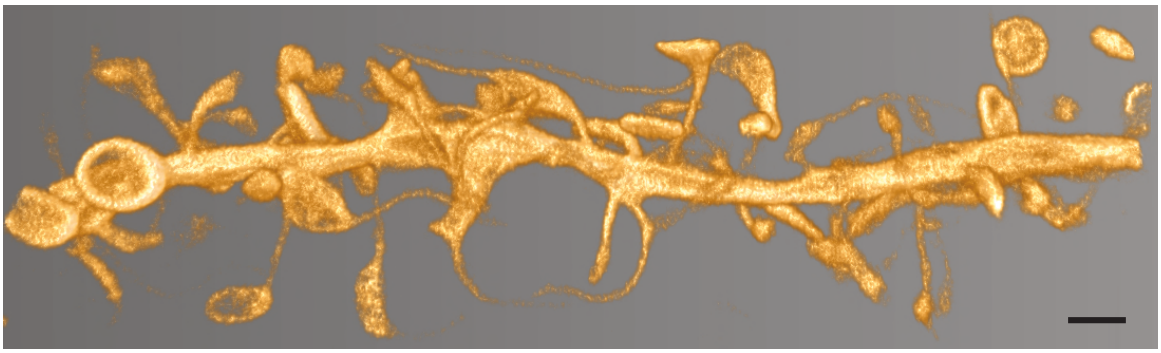

Figure 2.27: 3D protected STED imaging of a hippocampal neuron. *Rendering of a mature dendrite of a living neuron in a cultured hippocampal brain slice. The corresponding image stack of 56 z-slices spaced by 80 nm was recorded with 3D protected STED about 10 µm deep within the slice. Protected STED nicely resolves the filigree necks of the spines. Sample: Hippocampal neurons infected with Semliki Forest viruses encoding AC-rsEGFP2. Scale bar: 1 µm. Figure adapted from ref.* [70].

PSF is shrunken in axial direction compared to the PSF of classical one-photon (1P) excitation microscopy. Bleaching in out-of-focus regions is therefore reduced. This effect can also be harnessed for protected STED by *activating* ($OFF_2 \rightarrow OFF_1$) the proteins in a 2P process. To this end, the 405 nm laser was replaced by a Titanium:Sapphire laser delivering ~100 fs light pulses of 780 or 800 nm at 80 MHz repetition frequency. The increased sectioning capability of 2P activation was demonstrated in cultured CV-1 cells (Fig. 2.26a). By applying pulsed 780 nm light, activation of proteins in layers as far as 800 nm away of the actual focal plane can be drastically reduced compared to activation with 405 nm cw light (panel IV and VI in Fig. 2.26). Similarly, the activated area is better confined in the *xy*-plane (compare panel III and V). By this, background from out-of-focus planes can be suppressed which is especially relevant for highly 3D samples. Additionally, fluorophore bleaching and hence cell toxicity are reduced, since more deactivated molecules are kept in OFF_2. 3D protected STED including 2P activation was used to image again the actin network in living CV-1 cells confirming that 2P activation is indeed a viable alternative to standard 1P activation (Fig. 2.26b). Then, the full potential of 3D protected STED with 2P activation was explored by imaging neurons in living hippocampal brain slices. Actin was labeled by targeted injecting a Semliki Forest virus encoding the AC-rsEGFP(N205S) label one day before imaging. An image stack comprising 56 images with a voxel size of 35x35x80.5 nm^3 was recorded in a depth about 10 µm away from the glass-water interface (the oil objective lens was exchanged by a 63x glycerol objective with NA 1.3). The corresponding volume rendering reveals dendritic spines, with the fine necks nicely resolved (Fig. 2.27). Again, protected STED outperforms conventional 3D-RESOLFT [37] and 2D-STED imaging capabilities [152;153].

2.4 Conclusions and Discussion

With MOST, a new general concept for coordinate-targeted superresolution microscopy has been presented. It offers opportunities for fundamental improvements, especially in STED microscopy of living samples. MOST has been realized in the form of protected STED by combining reversible switching of fluorescent proteins and STED. It could be shown that the combination of two off-transitions is able to reduce fluorophore bleaching and to improve the on/off contrast within the subdiffraction sized probe volume.

Since different state transitions require different optical parameters, varying the parameter of one or more of the transitions specifically allows one to engineer the effective PSF of the imaging process in the most favorable way. For example, if a single off transition, such as deactivation, yields a pedestal reducing the on/off contrast, this can be counteracted by tuning another transition.

Thereby, MOST extends the parameter space of applicable optical intensities, pulse energies, durations and wavelengths. Although imaging parameters have been extensively varied, the combination of parameters used herein for STED and reversible photoswitching is by no means exhaustive. Further systematic screening may yield better conditions for providing higher resolution, imaging speed, and contrast.

The synergistic effect of the two off transitions reduces the intensities below that required just for STED or just for RESOLFT, because the combined action of the two, as realized in protected STED, can yield the same level of contrast. Therefore, the MOST concept also enables the exploration of transitions that do not provide sufficient state contrast for applications on their own. Another way of improving these concepts is to design switchable fluorophores that are specifically optimized for protected STED and MOST purposes. In future, switchable organic fluorophores[144] should enable exceptional imaging performance, given that to date organic dyes are among the best labels for STED.

While protected STED in 3D was carried out with co-aligned *xy*- and *z*-doughnuts, imprinting the phase shifts for *xy*- and *z*-doughnut on single STED and deactivation beams would simplify the microscope alignment. Also, other intensity distributions are amenable. Protected STED should lend itself well to high-speed parallelized nanoscopy[38;55;56] using arrays of minima, where background reduction is an issue due to signal overlap from neighboring recording channels. Reducing the background further by protected STED also means that fewer photons need to be collected, leading to more gentle live-cell imaging conditions.

Protected STED is the most straightforward realization of the MOST concept and other combinations of off-switching transitions are conceivable. Every optical or otherwise induced mechanism that alters the signaling properties of a marker species can be used for creating state

contrast. Preferably, state transitions should not involve (intermediate) states which reduce the number of state cycles by being prone to bleaching or other detrimental processes. For all these reasons, it is anticipated that the joint use of multiple off-switching transitions and its prototype realization protected STED can play an important role in future (live-cell) microscopy with diffraction-unlimited 3D resolution.

2.5 Material and Methods

2.5.1 Nanoscopy setup

Laser light was spectrally filtered, switched and intensity-modulated by acousto-optic modulators (AOMs) and coupled into polarization-maintaining single-mode fibers with the exception of the femtosecond 2P activation laser. STED laser pulses were detected and used for triggering the excitation lasers. STED and excitation pulses were synchronized by home-built electronics. STED and deactivation light was passed through phase plates. Laser beams were overlapped on dichroic mirrors (DM) or polarizing beamsplitter cubes (PBS) and coupled into the back aperture of an objective lens. Fluorescence light was collected by the same objective lens (OL), descanned, and imaged onto a pinhole of variable size (MPH16, Thorlabs, Newton, NJ, USA). Depending on the sample, the pinhole diameter was chosen between sizes corresponding to 0.7-1.0 times the Airy disk at this position. The transmitted fluorescence was focused onto two avalanche photodiodes (APDs). Detection was time-gated on the nanosecond timescale [147], unless otherwise noted by the home-built electronics. Hardware was controlled by an FPGA board (PCIe-7852R, National Instruments, Austin, TX, USA). Microscope control and image acquisition were done with the software ImSpector (Max Planck Innovation).

Component specifications

Lasers: 1P-Acitvation: diode laser DL100 (Toptica, Photonics, Graefelfing, Germany), 405 nm, cw; or diode laser 405-100-COL (Oxxius, Lannion, France), 405 nm, cw. 2P-Activation: Titanium:Sapphire femtosecond laser Mai Tai-HP (Newport-Spectra Physics, Santa Clara, CA, USA). Deactivation: laser diode LBX-488-70-CIR-PP (Oxxius), 488 nm, cw; DPSS laser Dual Calypso (Cobolt, Solna, Sweden), 491 nm, cw. Excitation: Diode lasers with ~100 ps pulse length. 488 nm PicoTA (Toptica Photonics, Graefelfing, Germany and PicoQuant, Berlin, Germany); 476 nm LDH-D-C-485 (PicoQuant, Berlin, Germany); 516 nm LDH-D-C-510 (PicoQuant, Berlin, Germany). STED: Raman-shifted fiber laser Rainbow (prototype, IPG Photonics, Mountain View, CA, USA), 587 nm, 572 nm (or 558 nm), repetition frequency: 20 MHz (or 1 MHz), pulse width: ~0.5-1.1 ns (tuneable).

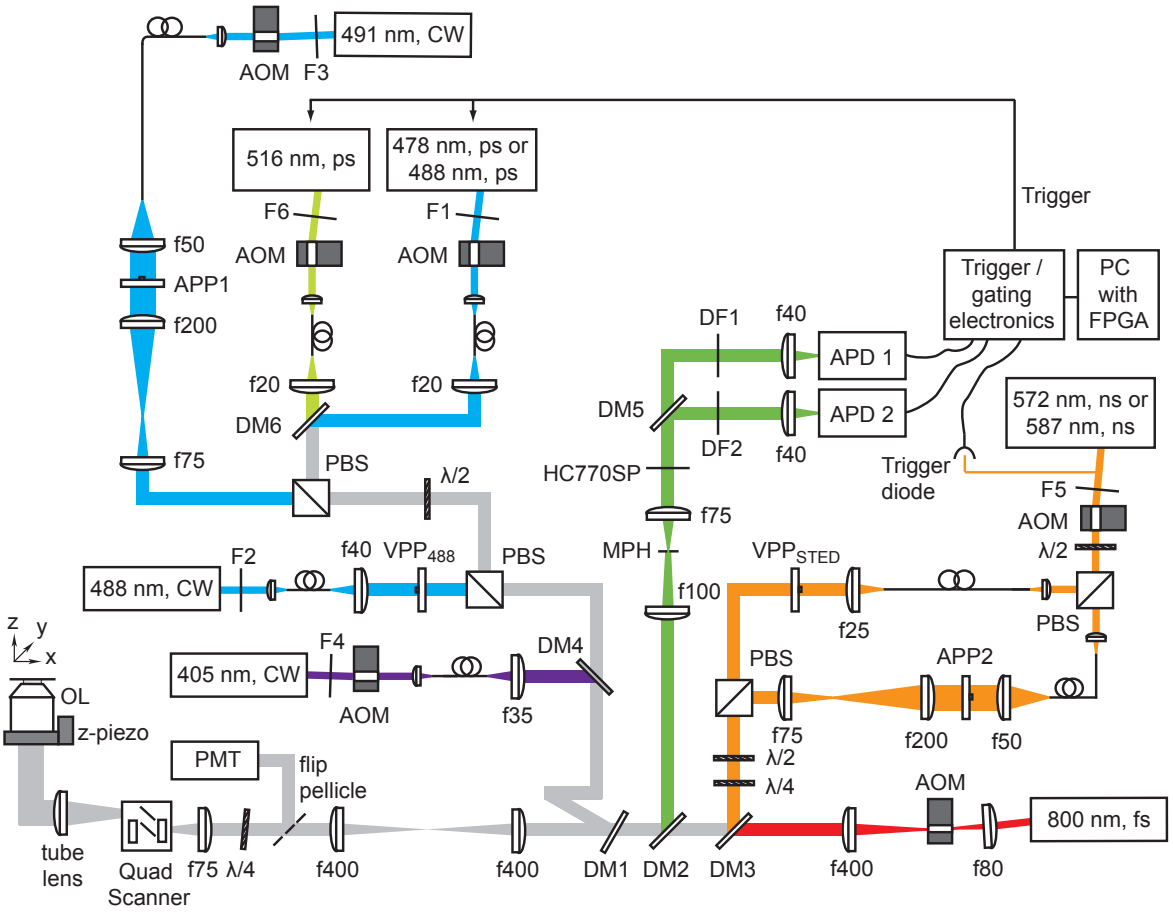

Figure 2.28: Schematic drawing of the relevant (optical) parts of the microscope setup. *Beam steering mirrors were omitted for clarity. OL: objective lens, f: focal length, DM: dichroic mirror, AOM: acousto-optic modulator, DF: detection filter, CW: continuous wave, APP: annular phase mask, VPP: vortex phase mask, PBS: polarizing beam splitter, PMT: photo-multiplier tube, APD: avalanche photodiode, FPGA: field programmable gate array, MPH: motorized pinhole. fs: femtosecond, ns: nanosecond. Figure reproduced from ref.* [70].

Laser cleanup filters: F1: BrightLine 488/6 for 488 nm and Versachrome (Semrock) for 476 nm; F2: MaxLine 488 (Semrock); F3: 532 nm notch + 491/10; F4: BrightLine 405/10 (Semrock); F5: BrightLine 591/6 and StopLine 594 for STED at 587 nm and Bright Line 575/15 plus StopLine 594 (Semrock) for STED at 572 nm; F6: BrightLine 520/5 (Semrock).

AOMs: MT110 or MT200 (AA Opto-electronics, Orsay, France).

Phase plates: Deactivation: *xy*-doughnut (VPP_{488}): 487 nm vortex phase plate VPP1a (RPC Photonics, Rochester, NY, USA); *z*-doughnut (APP1): annular phase plates (home-made): MgF_2 disc of 4.2 mm diameter and ~680 nm thickness on BK7 substrate for experiments with the 100x oil objective and cryolite disk of 5.8 mm diameter and ~810 nm thickness on BK7 substrate for experiments with 63x glycerol objective. STED: *xy*-doughnut (VPP_{STED}) vortex phase plate VPP1a or 1b (RPC Photonics); *z*-doughnut APP2: annular phase plates (home-made): MgF_2 disk of 4.1 mm diameter and ~700 nm thickness on BK7 substrate for experiments with the 100x oil objective and cryolite disk of 4.9 mm diameter and ~840 nm

thickness on BK7 substrate for 63x glycerol objective.

Scanning and positioning: galvanometric beam scanner 'Quad-Scanner'[54] (home-built). Piezo translator Mipos 100PL CAP (Piezosystem Jena, Jena, Germany).

Objective lenses: HCX-PL-APO 100x/1.4-0.7 OIL CS (Leica, Microsystems (Wetzlar, Germany) or HC PL APO 63x/1.3 GLYC CORR CS2 (Leica) for experiments in tissue; combined with a tube lens TL (Leica).

Detectors: avalanche photodiodes SPCM-AQRH-13 (Excelitas, Waltham, MA, USA) and/or PDM module (MPD, Bolzano, Italy).

Dichroic mirrors: DM1: 460 DCXRU (angle tuned, Chroma, Bellows Falls, VT, USA); DM2: 565DCXRU (Chroma); DM3: ZT594RDC (Chroma); DM4: 450DCXRU (Chroma); DM6: 495DCXRU (Chroma); DM5: Razor Edge 514 (Semrock) (optional).

Detection filters: one APD: DF1: BrightLine 525/50 (Semrock, Rochester, NY, USA) or two APDs: DM5; APD 1: DF1; APD2: DF2: BrightLine 535/50 and 594 nm (Semrock). Two-colour measurements: DM5; APD1: BrightLine 514/30 and StopLine 532 (Semrock), both angle tuned; APD2: BrightLine 535/50 and EdgeBasic 514 LP (Semrock); Experiments with 2P activation: HC770SP (Chroma).

Setup for rsCherryRev1.4 experiments

For experiments with rsCherryRev1.4 (Fig. 2.7): Laser for STED: pulse fibre laser ELP-5-775-DG (IPG Photonics Corporation, Oxford, MA, USA), 775 nm, 20 MHz, 1.2 ns pulse duration. Laser for activation: pulsed laser diode LDH-P-C440B (PicoQuant), 440 nm. Laser for excitation: supercontinuum laser Solea (PicoQuant), 560 nm. Laser for deactivation: VFL-P-1000-592 (MPB Communications, Montreal, Canada), 592 nm, cw. All laser beams were passed through AOMs and were focused to circular spots. Fluorescence was detected in the 600-650 nm spectral window.

Point spread functions and beam alignment

For beam alignment and PSF characterization, a pellicle beam splitter (BP145B1, Thorlabs) was flipped into the beam path to direct light reflected by gold or silver nanospheres on a PMT (H10723-01, Hamamatsu Photonics, Hamamatsu, Japan) or a webcam. Measured point spread functions are given in Fig 2.29. For 3D imaging of tissue, the correction collar of the glycerol objective was set at a position where it compensates for aberrations in about 10 µm imaging depth and then the intensity minima were co-aligned.

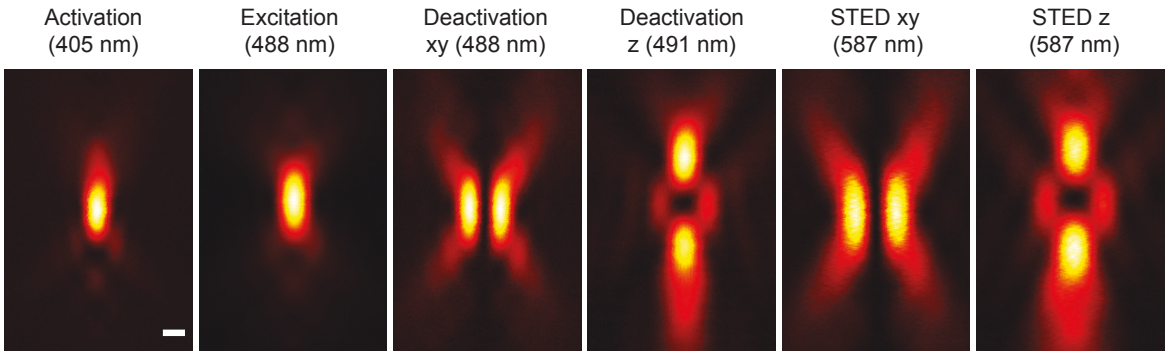

Figure 2.29: *Superimposed point spread functions of the individual beams in xz-direction measured on gold nanospheres. Scale bar: 200 nm. Figure adapted from ref.* [70].

2.5.2 Image acquisition and analysis

Images represent raw data, except, where indicated, smoothing by convolution with a 1-2 pixel wide Gaussian using Matlab (Mathworks, Natick, MA, USA) or ImSpector was performed. Line profiles with the specified widths were measured on raw data in ImSpector. Fitting of line profiles was done with OriginPro (OriginLab, Northampton, MA, USA). Linear unmixing of two colour image data was done with the SpectralUnmixing plugin (rsbweb.nih.gov/ij/plugins/spectral-unmixing.html) of ImageJ (imagej.nih.gov/ij/).

Imaging parameters of individual figures

Figure 2.5: Pulse sequences per pixel: **a**, Activation: 50 µs, 300 nW, plus Break: 10 µs; Deactivation: 2 ms, regular focus with 491 nm, 3.8 µW, plus *xy*-doughnut with 488 nm, 4.4 µW; R_1: Excitation: 488 nm, 50 µs, 1.1 µW; Break: 1 µs; STED: regular focus with 587 nm, 50 µs, 3.5 mW; Break: 1 µs; R_2: Excitation: 488 nm, 50 µs, 1.1 µW. **b**, Identical parameters as in a, without STED pulse. **c**, Activation: 50 µs, 300 nW; Break: 2.01 µs; R_1: Excitation: 488 nm, 50 µs, 280 nW; Break: 52 µs; R_2: Excitation: 488 nm, 50 µs, 280 nW. Pixel size: 30 nm.

Figure 2.6: Each region was scanned four times with the indicated pulse sequences per pixel. Parameters of light pulses: Activation: 50 µs, 210 nW, plus Break: 10 µs; Excitation: 488 nm, 60 µs, 610 nW; STED: *xy*-doughnut, 587 nm, 7.1 mW. Deactivation: scanning a larger region with 488 nm light. Pixel size: 20 nm. Data smoothed: 1.2 pixel Gaussian. Colour map is kept constant.

Figure 2.7: Each region was scanned five times with the indicated pulse sequences per pixel. Parameters of light pulses: **b**,**c**, Activation: 405 nm, 50 µs, 230 nW, plus Break: 10 µs; Excitation: 488 nm, 40 µs, 0.9 µW, plus STED: *xy*-doughnut with 587 nm, 7.3 mW. Deactivation: scanning a larger region with 470 nm light. Pixel size: 20 nm. Data smoothed: 1.2 pixel Gaussian. **e**,**f**, Activation: 440 nm, 200 µs, 3.7 µW, plus Break: 10 µs; Excitation: 560 nm, 500 µs, 0.4 µW, plus STED: regular focus with 775 nm, 17.5 mW, plus Break: 10 µs. Deactivation: scanning a

larger region with 590 nm light. Pixel size: 20 nm. Raw data.

Figure 2.8: **a**, Activation: 280 nW, 50 µs; Break: 10 µs; Excitation: 488 nm, 500 nW, 50 µs. Pixel size: 50 nm. **b**,**c**, Activation: 280 nW, 50 µs; Break: 10 µs; Deactivation: 2 ms, *xy*-doughnut with 488 nm, 4.4 µW and regular focus with 491 nm, 3.3 µW; R_1: Excitation: 488 nm, 50 µs, 1 µW; R_2: Excitation: same as in R_1; STED: 587 nm, *xy*-doughnut with 10.5 mW and regular focus with 6.0 mW. Pixel size: 30 nm. **d**, Same parameters as in a. Raw data.

Figure 2.10: Each square was scanned four times with the indicated pulse sequences per pixel. Parameters of light pulses: Square i: Activation: 50 µs, 280 nW, plus Break: 10 µs; Excitation: 488 nm, 50 µs, 830 nW; STED: *xy*-doughnut, 587 nm, 6.3 mW. Square ii: Activation: 50 µs, 280 nW, plus Break: 10 µs; Deactivation: 200 µs, 5 µW; Excitation: 488 nm, 60 µs, 2.3 µW; STED: *xy*-doughnut, 587 nm, 6.3 mW. Pixel size: 20 nm. Raw data.

Fig. 2.11: Pulse sequences per pixel: *rsEGFP2*: Activation: 50 µs, 280 nW; Break: 10 µs; Deactivation: *xy*-doughnut for variable time with 5.3 µW; Excitation: 488 nm, 30 µs, 2.2 µW, plus STED: *xy*-doughnut with 587 nm, 13.1 mW. *rsEGFP(N205S)*: Activation: 50 µs, 280 nW; Break: 10 µs; Deactivation: *xy*-doughnut with 3.6 µW; Excitation: 476 nm, 50 µs, 1 µW, plus STED: *xy*-doughnut with 587 nm, 3.5 mW. *rsEGFP*: Activation: 50 µs, 320 nW; Break: 10 µs; Deactivation: *xy*-doughnut with 5.3 µW; Excitation: 488 nm, 50 µs, 1.1 µW, plus STED: *xy*-doughnut with 587 nm, 5.1 mW. Pixel size: 20 nm.

Fig. 2.12: **a**,**b**, *STED series*: Activation: 40 µs, 140 nW; Break: 10 µs; Excitation: 488 nm, 30 µs, 1.4 µW, plus STED: *xy*-doughnut with 587 nm, 7.6 mW. *Protected STED series*: Activation: 50 µs, 210 nW; Break: 10 µs; Deactivation: *xy*-doughnut with 350 µs, 4.4 µW; Excitation: 488 nm, 40 µs, 2.2 µW, plus STED: *xy*-doughnut with 587 nm, 1.5 mW. *RESOLFT series*: Activation: 50 µs, 230 nW; Break: 10 µs; Deactivation: *xy*-doughnut with 488 nm, 400 µs, 3.7 µW; Excitation: 491 nm, cw, 10 µs, 8.2 µW. No ns time-gating. Pixel size: 30 nm. Data smoothed: 1.2 pixel Gaussian.

Fig. 2.13: **a**, *Protected STED with 30 µs Deactivation*: Activation: 50 µs, 230 nW; Break: 10 µs; Deactivation: *xy*-doughnut with 488 nm, 30 µs, 6.2 µW; Excitation: 488 nm, 30 µs, 1 µW, plus STED: *xy*-doughnut with 587 nm, 3.3 mW; Break: 6 µs. Mean ± standard deviation (n=5 cells). **b**, *Protected STED with 7.6 mW STED power*: Activation: 50 µs, 230 nW; Break: 10 µs; Deactivation: *xy*-doughnut with 488 nm, 350 µs, 4.4 µW; Excitation: 488 nm, 40 µs, 1.4 µW, plus STED: *xy*-doughnut with 587 nm, 7.6 mW; Break: 6 µs. Mean ± standard deviation (n=5 cells). *Protected STED (Fig. 2.12)*: Activation: 50 µs, 210 nW; Break: 10 µs; Deactivation: *xy*-doughnut with 488 nm, 350 µs, 4.4 µW; Excitation: 488 nm, 40 µs, 2.2 µW, plus STED: *xy*-doughnut with 587 nm, 1.5 mW. *STED (Fig. 2.12*: Activation: 40 µs, 140 nW; Break: 10 µs; Excitation: 488 nm, 30 µs, 1.4 µW, plus STED: *xy*-doughnut with 587 nm, 7.6 mW. Pixel size: 30 nm. **c**, Colour map: 0-35 counts (kept constant).

Fig. 2.14: **a**, Parameters were identical to the STED experiments in Fig. 2.12 except for the following variations. *STED (Fig. 2.12)*: Activation: 40 µs, 140 nW; Break: 10 µs; Excitation: 488 nm, 30 µs, 1.4 µW, plus STED: *xy*-doughnut with 587 nm, 7.6 mW. *STED with 350 µs Break*: Activation; Break: 360 µs; Excitation plus STED. *STED with 350 µs readout*: Activation; Break: 10 µs; Excitation: 350 µs, 110 nW, plus STED: 7.6 mW. *STED with line accumulation*: Activation: 40 µs, 105 nW; Break: 10 µs; Excitation: 50 µs, 130 nW, plus STED; Break: 6 µs. Each line was scanned 4 times and counts were accumulated. *STED with 1 MHz*: Activation: 40 µs, 105 nW; Break: 10 µs; Excitation: 400 µs, 50 nW, 1 MHz, plus STED: 0.41 mW, 1 MHz; Break: 6 µs. Pixel size: 30 nm. Mean ± standard deviation (n=3 cells). **b**, *RESCue-STED*: Activation: 40 µs, 140 nW; Break: 3 µs; Excitation: 30 µs, 1.5 µW, plus STED: 7.6 mW with RESCue-STED decision; Break: 6 µs. RESCue settings (dT decision time, uTh/lTh upper/lower threshold): dT1: 30% of 30 µs, lTh1: 1 count; dT2: 40% of 30 µs, lTh2: 2 counts. uTh: 15 counts. Pixel size: 30 nm. Mean ± standard deviation (n=4 cells).

Figure 2.15: **a**, Activation: 60 µs, 260 nW; Break: 10 µs; Deactivation: *xy*-doughnut with 488 nm, 800 µs, 4.6 µW; Excitation: 488 nm, 70 µs, 0.5 µW. **b**, Activation: as in a; Break: 70 µs; Excitation: 70 µs, 0.5 µW, plus STED: *xy*-doughnut with 587 nm, 5.8 mW. **c**, Activation: as in a; Break: 10 µs,; Deactivation: as in a; Excitation: 70 µs, 2.2 µW, plus STED: as in b. Pixel size: 20 nm. Colour maps: a: 0-110 counts, b: 0-70 counts, c: 0-130 counts, confocal: 0-100 counts. Data smoothed: 1.0 pixel Gaussian.

Figure 2.16: **b**, Activation: 50 µs, 500 nW; Break: 10 µs; Excitation: 476 nm, 50 µs, 2.1 µW, plus STED: *z*-doughnut with 587 nm, 8.2 mW. **c**, Activation: 30 µs, 440 nW; Break: 10 µs; Deactivation: *z*-doughnut with 491 nm, 600 µs, 5.8 µW; Excitation: 476 nm, 40 µs, 2.0 µW, plus STED: *z*-doughnut with 587 nm, 1.66 mW. Every *x*-line scanned twice and pixel counts were accumulated. Pixel size: 30x30 nm (*xz*). Data smoothed: 1.2 pixel Gaussian.

Figure 2.17: **a**, *STED*: Activation: 50 µs, 240 nW; Break: 10 µs; Excitation: 488 nm, 50 µs, 1.9 µW, plus STED: *xy*-doughnut with 587 nm, 11.6 mW. *RESOLFT*: Activation: 60 µs, 250 nW; Break: 10 µs; Deactivation: *xy*-doughnut with 488 nm, 2.5 ms, 5.6 µW; Excitation: 491 nm, cw, 50 µs, 0.7 µW. No ns time-gating. **b**, Activation: 60 µs, 240 nW; Break: 10 µs; Deactivation: *xy*-doughnut with 488 nm, 1.5 ms, 4.1 µW; Excitation: 488 nm, 70 µs, 1.7 µW, plus STED: *xy*-doughnut with 587 nm, 6.7 mW. **c** Excitation: 488 nm, 10 µs, 1.4 µW, plus STED: *xy*-doughnut with 587 nm, 10.5 mW; Break: 5 µs. Accumulation of pixel counts from 4 scans of each *x*-line. Pixel size in all panels: 20 nm.

Figure 2.18: **a**, Activation: 40 µs, 210 nW; Break: 13 µs; Excitation: 488 nm, 30 µs, 0.6 µW, plus STED: *xy*-doughnut with 587 nm, 10 mW; Break: 6 µs). **b**, Activation: 50 µs, 210 nW; Break: 10 µs; Deactivation: *xy*-doughnut with 488 nm, 350 µs, 4.2 µW; Excitation: 488 nm, 40 µs, 2.1 µW, plus STED: *xy*-doughnut with 587 nm, 7.6 mW; Break: 6 µs. In both experiments,

accumulation of pixel counts from 2 scans of each x-line. Pixel size: 20 nm. Data are raw.

Figure 2.19: **a**, Activation: 50 µs, 210 nW; Break: 10 µs; Deactivation: *xy*-doughnut with 488 nm, 350 µs, 3.8 µW; Excitation: 488 nm, 40 µs, 2.1 µW, plus STED: *xy*-doughnut with 587 nm, 7.6 mW; Break: 6 µs. Each line was scanned twice and counts were accumulated. Data smoothed (1.2 pixel Gaussian). **b**, Line profiles: on raw data fitted to Lorentzians. Profile widths: 10 pixels. Signal-to-background ratio was determined between the fitted peak and the immediate surroundings of the respective filament.

Fig. 2.20: **a**, RESOLFT: Activation: 50 µs, 210 nW; Break: 10 µs; Deactivation: *xy*-doughnut with 488 nm, 400 µs, 8 µW); Break: 3 µs; Excitation: 488 nm, 13 µs, 2.2 µW; Break: 5 µs. Protected STED: Activation: 50 µs, 220 nW; Break: 10 µs; Deactivation: *xy*-doughnut with 488 nm, 350 µs, 4.4 µW; Excitation: 488 nm, 40 µs, 2.1 µW, plus STED: *xy*-doughnut with 587 nm, 5.1 mW; Break: 6 µs. Data smoothed: 1.1 pixel Gaussian. **b**,**c**, STED: Activation: 40 µs, 140 nW; Break: 13 µs; Excitation: 488 nm, 30 µs, 0.7 µW), plus STED: *xy*-doughnut with 587 nm, 10 mW; Break: 5 µs. Parameters of protected STED and RESOLFT same as in panel a. Data in panel b smoothed: 1.2 pixel Gaussian. Data in panel c represent mean ± standard deviation (n=3 or 4 cells). Pixel size in all panels: 25 nm.

Figure 2.21: **a**, **c**, **d**, Activation: 50 µs, 230 nW; Break: 10 µs; Deactivation: *xy*-doughnut with 488 nm, 350 µs, 4.4 µW and *z*-doughnut with 2.1 µW; Excitation: 488 nm, 40 µs, 2 µW, plus STED: 587 nm, *xy*-doughnut with 2.3 mW and *z*-doughnut with 5.8 mW. Scan order: *xzy*. Data smoothed: a: 1.3 pixel Gaussian; c: 1.5 pixel Gaussian; d: 1.2 pixel Gaussian. Rendering in c: with 3D viewer of ImageJ. **b**, Maximum intensity projection of a confocal stack. Voxel size: 100x100x500 nm^3. **e**, Activation: 50 µs, 220 nW; Break: 10 µs; Deactivation: *xy*-doughnut with 488 nm, 350 µs, 4.4 µW and *z*-doughnut with 2.2 µW; Excitation: 488 nm, 40 µs, 1.3 µW, plus STED: 587 nm, *xy*-doughnut with 2.1 mW and *z*-doughnut with 5.9 mW. Scan order: *xzy*. Data smoothed: 1.2 pixel Gaussian. Line profiles: on raw data fitted to Lorentzians.

Figure 2.22: Activation: 60 µs, 500 nW; Break: 10 µs; Deactivation: *xy*-doughnut with 488 nm, 1.5 ms, 2 µW) and *z*-doughnut with 491 nm, 1.6 µW; Excitation: 488 nm, 100 µs, 1.1 µW, plus STED: 572 nm, *xy*-doughnut with 7.6 mW and *z*-doughnut with 3 mW. Pixel size: 20 nm. Data (1.3 pixel Gaussian). Colour map saturated at brightest pixels. **b**, **c**, Line profiles: on raw data fitted to Lorentzians. Line width: b: 3 pixels, c: 10 pixels.

Figure 2.23: Same parameters as in Figure 2.22. Voxel size: 20x20x61 nm^3 (*xyz*). Scan order: *xyz*.

Figure 2.24: **a**, *RESOLFT*: Activation: 20 µs (of these 10 µs rise-time), 610 nW; Break: 3 µs; Deactivation: *xy*-doughnut with 50 µs, 41.4 µW; Break: 1 µs; Excitation: 491 nm cw, 5 µs, 3.5 µW; Break: 1 µs. **b**, *Protected STED*: Activation: 30 µs (of these 10 µs rise-time), 610 nW; Break: 3 µs; Deactivation: *xy*-doughnut with 30 µs, 8.9 µW; Break: 1 µs; Excitation: 488 nm,

30 µs, 1.1 µW, plus STED: *xy*-doughnut with 587 nm, 5.1 mW; Break: 1 µs. Data in a and b smoothed (1.3 pixel Gaussian). **c**, *STED*: Activation: 30 µs, 230 nW; Break: 4 µs; Excitation: 488 nm, 30 µs, 0.7 µW, plus STED: *xy*-doughnut with 587 nm, 7.9 mW; Break: 1 µs. *Protected STED* and *RESOLFT*: as in a. Mean ± standard deviation (n=5 cells). Pixel size: 30 nm.

Figure 2.25: Activation: 20 µs, 680 nW; Break: 3 µs; Deactivation of rsEGFP(N205S): *xy*-doughnut with 488 nm, 30 µs, 4.1 µW; Read-out period 1: Excitation: 476 nm, 30 µs, 1.7 µW, plus STED: *xy*-doughnut with 587 nm, 3.4 mW; Read-out period 2: Excitation: 516 nm, 30 µs, 0.4 µW, plus STED: *xy*-doughnut with 587 nm, 3.4 mW. Detection: Channel 1: 490-510 nm, Channel 2: 520-565 nm. Images show linear unmixed data. Data smoothed (1.3 pixel Gaussian). Colour maps nanoscopy: green 0-40 counts, fire 0-25 counts. Pixel size: 25 nm for nanoscopy, 30 nm for confocal.

Figure 2.26: **a**, 2P-Activation: 60 µs, 3.5 mW; Break: 10 µs; Deactivation: 840 µs, *xy*-doughnut with 488 nm, 3.6 µW and *z*-doughnut with 491 nm, 1.9 µW; Excitation: 488 nm, 100 µs, 2.5 µW, plus STED: 572 nm, *xy*-doughnut with 7 mW and *z*-doughnut with 2.7 mW. Pixel size: 20 nm. Scale bar: 1 µm. **c**, III,IV: 1P-Activation: 405 nm, 40 µs, 110 nW. V, VI: 2P-Activation: 800 nm, 40 µs, 1.5 mW. Pixel size: 90 nm.

Figure 2.27: 2P-Activation: 800 nm, 30 µs, 5.9 mW; Break: 3 µs; Deactivation: 180 µs, *xy*-doughnut with 488 nm, 7.8 µW and *z*-doughnut with 491 nm, 8.7 µW; Excitation: 488 nm, 80 µs, 3.4 µW, plus STED: 587 nm, *xy*-doughnut with 3.5 mW and *z*-doughnut with 2.1 mW. Voxel size: 35x35x80 nm^3 (*xyz*). Image dimensions: 7x20x4.5 μm^3 (*xyz*). Scan order: *xzy*. Image rendering: 3D volume of smoothed data (1.2 pixel Gaussian) with Amira v6.0 (Hillsboro, OR, USA).

2.5.3 Cell culture and transfection

HeLa or CV-1 cells were plated on glass coverslips and transfected with a vector encoding a fusion of rsEGFP, rsEGFP2, or rsEGFP(N205S) with the protein of interest. The actin chromobody (AC) label AC-rsEGFP(N205S) is a fusion of rsEGFP(N205S) with an actin camelid antibody (Chromobody, Chromotek, Planegg, Germany). Imaging was typically performed 24-48 h after transfection in HEPES-buffered Dulbecco's modified Eagle's medium without phenol red at room temperature. Measurements were performed only on cells showing no signs of apoptosis.

2.5.4 Preparation of hippocampal brain slices

In this section, the publication Danzl, Sidenstein *et al. Nature Photonics* **10**, 122-128 (2016) is cited from here on: "Organotypic hippocampal slice cultures were prepared from wild-type C57BL/6 mice on postnatal day 5-7. Hippocampi were dissected into 400 µm thick slices and each slice was embedded in a plasma clot on a #1 cover slip. The plasma clot was formed

using equal parts of chicken plasma (Sigma Aldrich) and a coagulating thrombin solution, which contained 0.5 mg/mL thrombin (VWR/Merck, Darmstadt, Germany) resuspended in equal parts of distilled water and Gey's balanced salt solution (home-made, components from VWR/Merck). Slices were cultured in a roller incubator at 35 °C according to procedures described by Gähwiler et al.[154] in a medium composed of: 97 mL Basal Medium Eagle (Gibco), 50 mL Hank's Buffered Salt Solution (Gibco), 50 mL horse serum (Gibco), 2 mL of 45% glucose solution (VWR/Merck), 1 mL of 200 mM glutamine solution (Gibco). Slices were used for imaging 10 days to ~6 weeks after preparation. Semliki Forest virus particles (SFVs) for expression of AC-rsEGFP2 in living brain slices were generated essentially as previously described[152]. We incorporated the DNA sequence coding for a fusion protein of the actin chromobody with rsEGFP2 into a pSCA3 vector as described above. We cotransfected Hek293 cells with the pSCA3-AC-rsEGFP2 plasmid and a pSCA helper plasmid coding for viral structural components[155]. Five days after transfection, we lysed cells with two freeze-thaw cycles. Cellular debris was removed by centrifugation at 1,700 g for 10 minutes. SFVs were pelleted by centrifugation at 48,000 g for 2 hours and resuspended in TBS-5 (130 mM NaCl, 10 mM KCl, 5 mM $MgCl_2$, 50 mM Tris-HCl, pH 7.8). Chymotrypsin was applied for virus activation. Virus particles were injected into the CA1 and CA3 regions with a pressure injector (Tooheyspritzer, Toohey Company, Fairfield, NJ) using a patch clamp pipette. Slices were cultured for another 12-48 h after virus injection. Slices were transferred to an imaging chamber and imaged in artificial cerebrospinal fluid containing 126 mM NaCl, 2.5 mM KCl, 2.5 mM $CaCl_2$, 1.3 mM $MgCl_2$, 30 mM glucose, 27 mM HEPES with pH adjusted to 7.4 with NaOH. Imaging was performed at room temperature."

Chapter 3

Multicolour multilevel STED nanoscopy[1]

3.1 Introduction

Far-field optical superresolution techniques such as STED nanoscopy are on track to become standard methods for molecule-specific imaging in the life sciences and beyond[125;156]. At present, however, simultaneous recordings of more than two fluorophore species with resolution beyond the diffraction limit still requires development. The project described in this chapter aimed to develop and evaluate novel modalities for multicolour STED imaging and their application to biological samples.

3.1.1 Multicolour STED imaging schemes

Biological studies based on fluorescence microscopy often require the simultaneous identification of multiple species per sample. In the ideal case, all these species can be imaged with sub-diffraction resolution so that relative distances can be precisely depicted. For example, the interplay of actin and βII-spectrin periodic patterns in neurons could be disclosed by dual-colour STORM[134] and STED microscopy[157]. To this end, in fluorescence microscopy, structures of interest are typically labeled with markers of different colours. Identification of species is then realized by means of their absorption and/or emission wavelengths, fluorescence lifetime or other parameters. Ideally, two or more discriminators are combined to synergistically suppress channel cross-talk. Thereto, conventional fluorescence microscopes are usually equipped with

1 The project was conducted together with E. D'Este, M.J. Böhm, J.G. Danzl, and V.N. Belov. Contributions are detailed on page 85. Results of the project were published as S.C. Sidenstein, E. D'Este, M.J. Böhm, J.G. Danzl, V.N. Belov, S.W. Hell (2016) *Scientific Reports* **6**, 26725.

multiple excitation lines and detection windows. Basically, this principle can be transferred to STED microscopy as well. However, if the emission maxima of the two or more fluorophore species differ by more than ~50 nm, more than one STED wavelength is needed. For example, Donnert *et al.* combined the dyes Atto532 (λ_{em} 553 nm) and Atto647N (λ_{em} 664 nm) for STED imaging with two doughnuts of 603 nm and 780 nm, respectively[158]. This scheme was applied to study, among others, the relative organization of the proteins Synaptophysin and Syntaxin 1 in neurons[159]. Nevertheless, the rather complex setup relies on the correct mutual alignment of the two STED doughnuts to ensure the nanometer-accurate colocalization of the colour channels. Moreover, this scheme is limited by the bleaching of Atto647N by the 603 nm STED beam. Images can therefore only be recorded sequentially rendering the scheme impractical for living samples. Thereafter, several dual-colour schemes for STED nanoscopy have been published to overcome these limitations.

The combination of dyes whose spectra are separated by only ~60 nm with two pairs of excitation and STED wavelengths is able to avoid the problem of mutual bleaching[86;160–164]. For example, Atto590 and Atto647N can be silenced with STED beams of 720 nm and 755 nm, respectively. Thereby, Atto647N is not excited and hence not bleached by the 720 nm STED line. Consequently, simultaneous recordings by pulsed-interleaved synchronization of the two pairs becomes possible. Yet, the increased detection cross-talk has to be removed by linear unmixing. Extending the scheme with time-resolved detection, allows separation of up to four marker species[165].

Setups are further simplified by combining a long Stokes shift and a conventional Stokes shifted dye[89;161;166–168]. While the absorption spectra of the dyes are well separated and hence can be addressed with high selectivity by two excitation wavelengths, the emission spectra greatly overlap. Thus, a single STED wavelength can be utilized for both dyes, significantly reducing setup complexity and costs. Even more important, the signal from both labels are intrinsically co-aligned, since a single doughnut zero determines the position from which fluorescence light is registered. Again, quasi-simultaneous recordings in pulsed- or line-interleaved schemes were realized.

Imaging with a single STED wavelength of 775 nm is also possible with two conventional Stokes shifted dyes like Atto594 and KK114[76]. The combination of two excitation wavelengths (594 nm and 640 nm) and two detection windows (620±20 nm and 670±20 nm) ensures that excitation cross-talk is suppressed by detection separation and *vice versa*. Once more, this scheme allows quasi-simultaneous imaging with intrinsically co-aligned colour channels. Today, this is the most-widely used dual-colour STED scheme and has been commercialized by several companies[169–171]. Recently, Winter *et al.*[172] developed a four-colour imaging scheme with single wavelengths for excitation (612 nm) and STED (775 nm). Fluorophore species are

discriminated by hyperspectral detection with four APDs in combination with post-processing by non-negative matrix factorization. Unfortunately, part of the dyes are strongly excited by the STED laser which causes fluorophore bleaching and confocal background in the images. The latter has to be recorded separately and subtracted from the raw images prior to the unmixing step.

In the yellow-orange regime, dual-colour STED imaging of living samples has been realized with a single excitation and a single STED laser harnessing the fluorescent proteins GFP and YFP[143]. Since their spectra are separated by only ~20 nm, rigorous linear unmixing is needed. The latter can be avoided by combining two reversibly photoswitchable fluorescent proteins with opposite activation properties[173]. Illumination with blue light leads to activation of one protein while the other is being deactivated. Another option for dual-colour live-cell imaging by (protected) STED has been presented in the previous chapter.

3.1.2 Potentials of the 620 nm line for STED

STED microscopy has been implemented with laser lines in basically any part of the visible spectrum[174]. Nonetheless, two STED wavelengths combined with respective markers emerged during the last few years. The STED wavelength of choice for imaging of fixed samples is usually the 775 nm line[76], since red to far-red emitting synthetic dyes are very bright and extremely photostable. However, for living samples the most widely established STED wavelength is still ~590 nm for de-exciting common green or yellow fluorescent proteins like GFP[96;97], YFP or Citrine[99] (see previous chapter). Red fluorescent proteins fitting to the 775 nm line like TagRFP657[100] or mGarnet[108] are still not in wide use. This can be due to the fact that optimization of well-expressing plasmids of the respective fusion proteins is time-consuming. As an alternative to genetically encoded markers, membrane-permeating dyes like silicon rhodamine[103] are available for labeling of intra-cellular structures (see Section 1.3). Red and far-red STED wavelengths have the advantage of being less absorpted and scattered by biological samples. Furthermore, auto-fluorescence is reduced as well. These factors become crucial especially when investigating samples more complex than single cell layers. Moreover, light of wavelength >600 nm is significantly less phototoxic than blue or UV light[137]. Due to its performance in terms of photostability, brightness and extent of maturation, EGFP is still the gold standard of fluorescent proteins. Hence, it is desirable to shift the STED wavelength as far as possible to the red without loosing the possibility to use EGFP as label. Additionally, moving the STED wavelength from 590 nm to for example 620 nm should enable the use of dyes with fluorescence peaking around 550 nm like Alexa532 or Atto532. Their fluorescence cannot be silenced at ~590 nm without pronounced anti-Stokes excitation which leads to excessive state cycling and bleaching. Thus, a large number of synthetic and genetically encoded markers for

620 nm STED imaging might come to the fore.

In particular, Atto532 is known for its photostability, low inter-system crossing rates (<1%) and high fluorescence quantum yield [75;175;176]. Nanoscopy of Atto532 was already demonstrated with STED wavelengths of 615 nm [177] and 620 nm [178], albeit by using complicated and expensive femtosecond mode-locked laser systems. Those systems usually consisted of a Titanium:Sapphire laser pumping an optical parameteric oscillator (OPO). The repetition rate of the obtained visible light was defined by the pump laser and was typically 76 or 80 MHz. Usually, the femtosecond-short OPO pulses were stretched to 200-300 ps. However, empirically it turned out that broader pulses of up to 1.2 ns are much more suited for STED, since their peak power is lower and hence photobleaching reduced [76]. The compact pulsed fibre laser harnessed as STED light source in this project delivers pulses of ~600 ps width at 40 MHz repetition rate.[1] This promises lower bleaching rates and convenient pixel dwell times of few tens of microseconds [76;165;179]. Indeed, the pulse repetition rate is lower compared to the aforementioned systems but still relatively high. Relaxation of fluorophores residing in dark states could be increased and hence bleaching further suppressed by reducing the repetition rate to few MHz and/or by dividing the continuous pulse train into bunches of only few pulses with microseconds-long breaks in between [81;82]. The latter strategy can be partly mimicked by repetitive scanning along the fast scan axis with short pixel dwell times and accumulation of the respective pixel counts.

3.2 Nanoscope design

A 620 nm STED microscope for multicolour imaging was developed (Fig. 3.1a). It based on the setup used for protected STED, but components were replaced to match the specific requirements of the project (technical details are given in the Methods section). A pulsed fibre laser was deployed as STED laser. Due to the relatively low output power of 400 mW at 40 MHz (10 nJ/pulse), the laser was not fibre-coupled, but guided without any beam purification to the back aperture of the objective lens. The regularly focused circular spots of the three excitation lines of 435 nm, 488 nm and 532 nm were superimposed with the doughnut-shaped 620 nm STED focus, which was obtained by inserting a helical vortex phase plate into the STED beam path. The wavelengths allow excitation of the whole range of potentially interesting markers with an emission peak in the range of 520-560 nm including long Stokes shift dyes (Fig. 3.1b). The fluorescence emitted within the STED doughnut center is collected by the objective lens used for excitation, and imaged onto a single confocal pinhole. This design ensures intrinsic nanometer-precise colocalization of the three colour channels which is even preserved when

1 A second STED laser, also utilized for protected STED, was configured to deliver pulses of 618 nm at 20 MHz repetition rate. It was deployed for some of the following measurements (see Methods) and provided similar results compared to the 40 MHz laser.

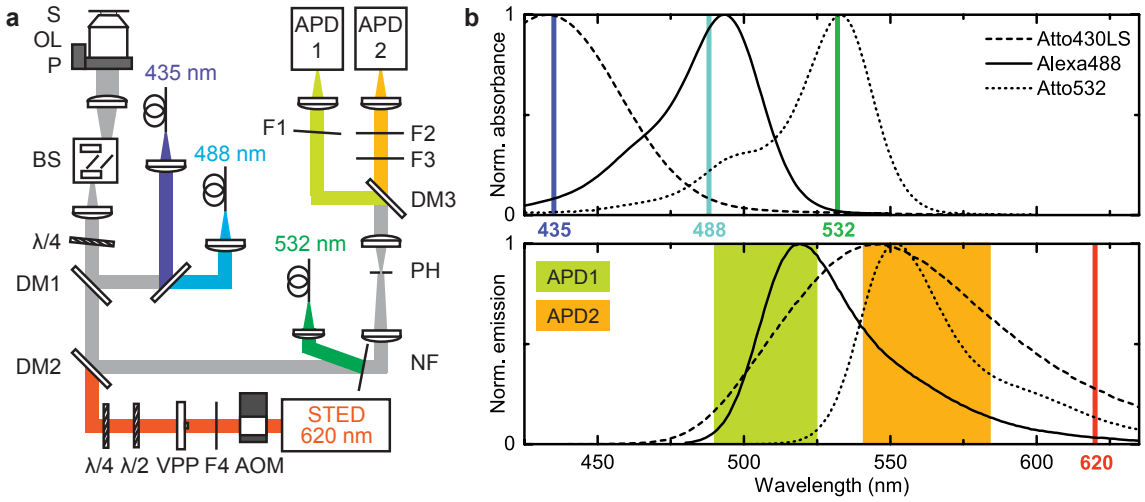

Figure 3.1: Microscope setup and spectral imaging scheme. *(**a**) Schematic drawing of the main optical parts of the STED microscope: S Sample, OL objective lens, P z-piezo translator, BS beam scanner, λ/2 half-wave plate, λ/4 quarter-wave plate, DM dichroic mirror (DM1: 460DCXRU, DM2: ZT594RDC, DM3: T525LPXR), NF notch filter (532nm Notch), PH pinhole, VPP vortex phase plate, AOM acousto-optic modulator, F filter (F1: 514/30, F2: 562/40, F3: 532nm Notch, F4: 620/14), APD avalanche photodiode detector. (**b**) Normalized absorption and emission spectra of the dyes Atto430LS, AlexaFluor488 and Atto532 utilized for three-colour imaging, as well as related laser lines and detection windows. Figure and caption reproduced from Sidenstein et al.* [180].

the excitation spots are misaligned relative to the STED doughnut [76]. After the pinhole, the signal is split into two spectral windows of 510±15 nm and 560±20 nm, focused each on a separate avalanche photodiode (APD1 and APD2, respectively) (Fig. 3.1a). Scanning in lateral directions is realized with a beam scanner consisting of four galvanometric scan mirrors making line frequencies of up to 2 kHz possible [54;181].

3.2.1 Multilevel STED

Generally, the STED power applied in a measurement depends on the fluorescent marker, which has a more or less large cross-section for stimulated emission, the investigated structure, which is more or less good labeled, and the specific imaging task, which demands recording of a single image or of a series of measurements. These and other conditions afford optimization of imaging parameters and, in particular, of the STED power for basically every new experiment. All the more this is true for simultaneously recorded colour channels which require, in principle, modulation of the STED power during the image acquisition. The relative spectral shifts and the corresponding deviating cross-sections for stimulated emission inherently lead to different STED power requirements for the different dyes. Here, switching of the STED power between two levels down to the single-pixel level is realized by home-built electronics ('multilevel STED'). As will be seen in the following, multilevel STED optimizes the resolutions and brightnesses of the individual channels in multicolour STED recordings.

3.3 Results

3.3.1 Evaluation of the imaging scheme

Series of synthetic and genetically encoded markers were screened for evaluating the setup and, in particular, for their use in combination with the 620 nm STED line. Since their absorption spectra are well separated, the three dyes Atto430LS, AlexaFluor488 and Atto532 were identified as being potentially suitable for three-colour imaging with low cross-talk (Fig. 3.1b). A semi-quantitative assessment of dye and setup performances is possible with dye-labeled DNA origamis[182]. Origamis stained at two positions with defined separation d were obtained for each of the three dyes[183] (Fig. 3.2a). The average degree of labeling was about 11 dye molecules per spot. Atto532-labeled marks at $d = 50\pm5$ nm could be clearly separated and showed individual full width at half maxima (FWHM) of <35 nm (Fig. 3.2b). Similarly, AlexaFluor488 and Atto430LS allowed separation of two sites spaced by 70±5 nm with single peak widths of <50 nm and <40 nm, respectively (Fig. 3.2c,d). The resolution in case of the AlexaFluor488 sample was limited by pronounced bleaching. Even higher resolutions for all dyes should be possible with more densely labeled samples which provide better signal-to-noise ratios and thereby enable higher STED powers.

Genetically encoded markers for live cell imaging were evaluated in HeLa cells. STED at 620 nm was able to image vimentin tagged by EGFP at a resolution of ~65 nm (Fig. 3.3). Similarly, Caveolin1-YFP and Keratin-Citrine could be resolved down to ~55 nm. As expected, these values are slightly higher than the ~40-50 nm usually obtained with STED at ~590 nm. This is mainly due to the lower cross-sections for stimulated emission of these markers at 620 nm.

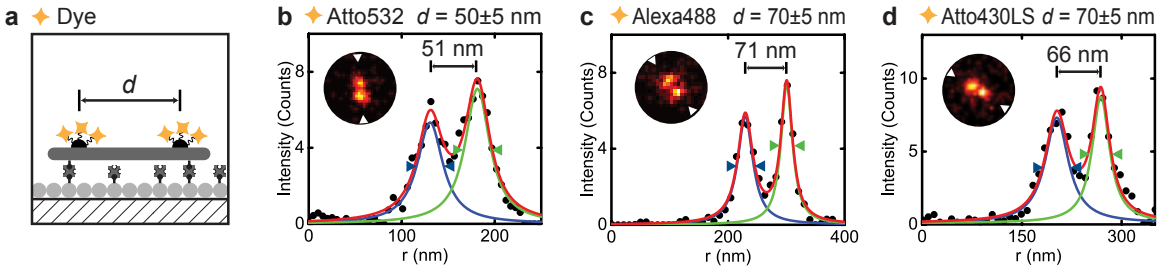

Figure 3.2: DNA origami imaging. *(**a**) Schematic drawing of a DNA origami molecule immobilized on a glass surface through biotin-neutravidin links. Two positions on the origami located at a distance d from each other are labeled with dye molecules. (**b**) Inset shows STED image of a single DNA origami molecule with spots marked by Atto532 molecules at d = 50±5 nm. The line profile drawn across the DNA origami shown in the inset was fitted by two Lorentzian functions. Fitting yielded a spot separation distance of 51 nm with single spot full width at half maxima (FWHM) of <35 nm. (**c**) Same as **d**, but for an origami with d = 70±5 nm labeled with AlexaFluor488. The corresponding fit yielded a separation distance of 71 nm and single-peak FWHM of <50 nm. (**d**) Same as **f** for an Atto430LS-labeled origami. The corresponding fit yielded a separation distance of 66 nm and peak FWHM of <40 nm. Figure and caption reproduced from ref.[180].*

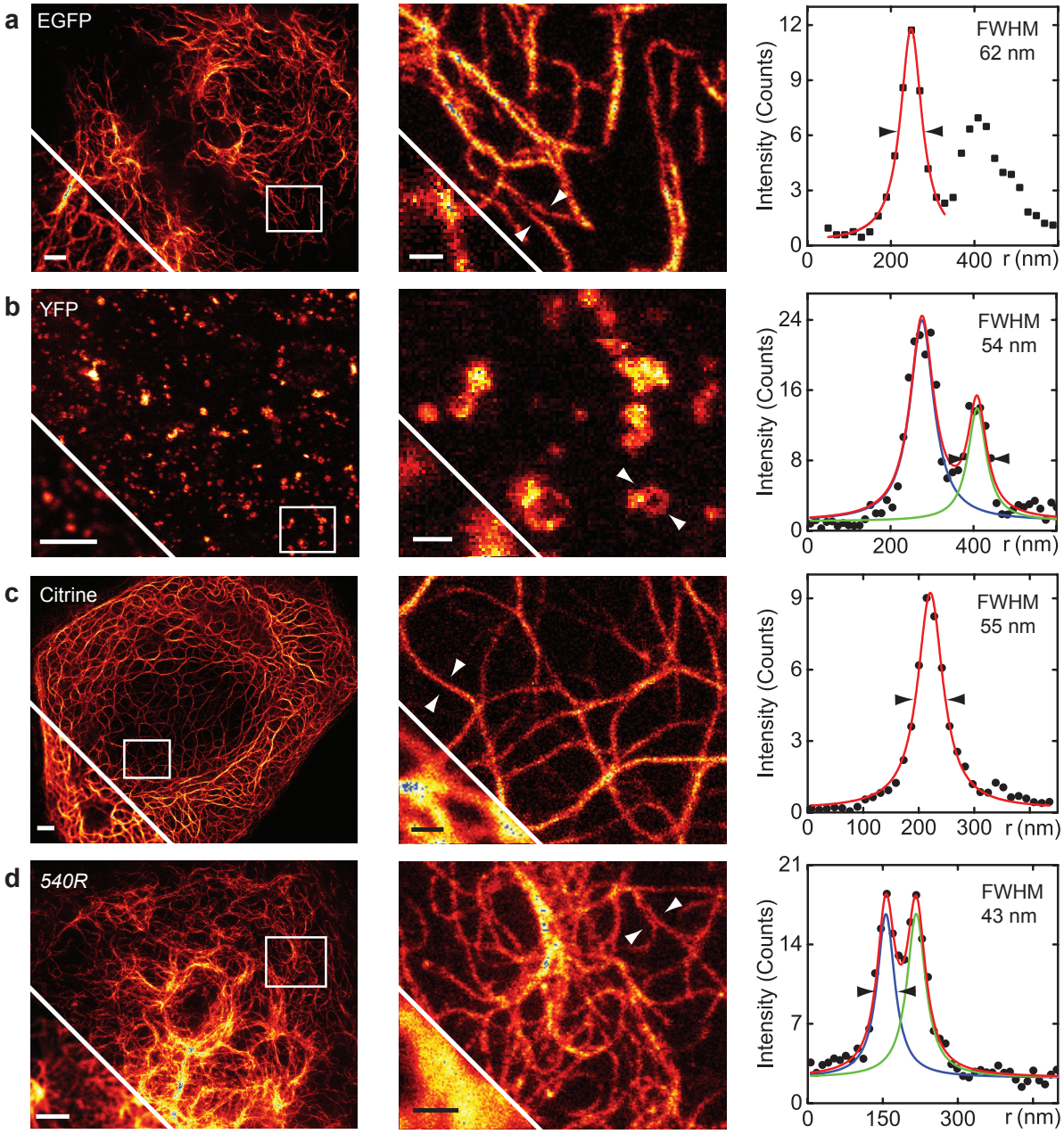

Figure 3.3: Fluorescent proteins and 540R dye in 620 nm STED nanoscopy. *Raw STED images, along with confocal sections in lower-left corner, of living HeLa cells expressing (**a**) vimentin-EGFP, (**b**) Caveolin1-YFP, (**c**) Keratin-Citrine, and (**d**) vimentin-Halo stained with 540R, respectively. Images in the middle column show close-ups of the region marked in the respective left image. Representative line profiles of filaments depicted in the diagrams on the right are indicated by arrowheads in the zoomed views and were fitted to Lorentzian functions. The obtained full width at half maxima (FWHM) give an approximation of the optical resolution. Features at this level of resolution and contrast can be found in multiple locations within the imaged field. Scale bars: left: 2 µm, right: 500 nm. Figure and caption reproduced from ref.[180].*

However, the obtained resolutions are already sufficient for many applications.

Promising alternatives to fluorescent proteins for imaging in living cells are membrane-permeating synthetic dyes. Prominent examples are the green- 6-carboxyrhodamine 110, the red- tetramethylrhodamine and the far-red-emitting silicon rhodamine[103]. However, up to now, there are no reports on dyes with an emission maximum around 560 nm suitable for live-cell imaging which would fit well to the 620 nm STED line. Therefore, a water-soluble 6'-carboxy-Q-rhodamine[184] (*540R*, λ_{abs} 540 nm, λ_{em} 561 nm) which was already successfully employed for labeling of fixed samples, was evaluated for live-cell imaging. This dye possesses a compact, zwitterionic structure with a relatively short distance between positive and negative charges which is characteristic of cell-penetrating synthetic probes[105] (Fig. 3.4). HeLa cells expressing a vimentin-Halo-tag fusion protein were incubated under growth conditions in a 1 µM solution of the Halo-tag derivative of *540R* for 20-30 min. Remaining unbound dye was washed out of the cells during another ~20 min by fresh medium. Bright stainings with low background were obtained (Fig. 3.3d). STED imaging at 620 nm was possible down to a resolution of ~45 nm without prominent anti-Stokes excitation by the STED laser.

3.3.2 Multicolour imaging with 620 nm STED

After positively evaluating several dyes, possible combinations of them were explored for multicolour 620 nm STED nanoscopy. EGFP and *540R* were assessed for dual-colour imaging of living cells. Their absorption maxima are separated by ~50 nm and fit very well to the excitation lines 488 nm and 532 nm, respectively (Fig. 3.5a). The emission of EGFP can efficiently be detected by APD1, those of *540R* by APD2. Importantly, the *540R* signal generated upon excitation with the 488 nm line is not influencing the EGFP colour channel, since it is not detected by APD1. On the other way around, EGFP signal potentially captured by APD2 is not present during *540R* read-out, since EGFP is not excitable at 532 nm. Dual-colour recordings were obtained by line-interleaved scanning with 488 nm excitation plus detection with APD1 and 532 nm excitation plus APD2 (Fig. 3.5b). Thereby, each line (along the fast scan axis) was scanned multiple times with the respective excitation-detection combination.

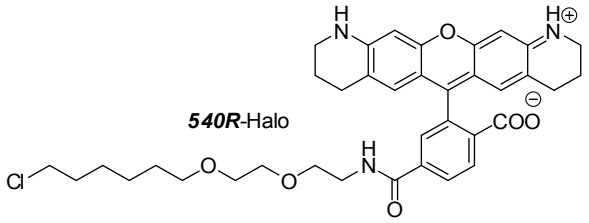

Figure 3.4: Structure of 540R. *Structure of 540R rhodamine dye bearing a chloroalkane (Halo-tag) linker (540R-Halo).*

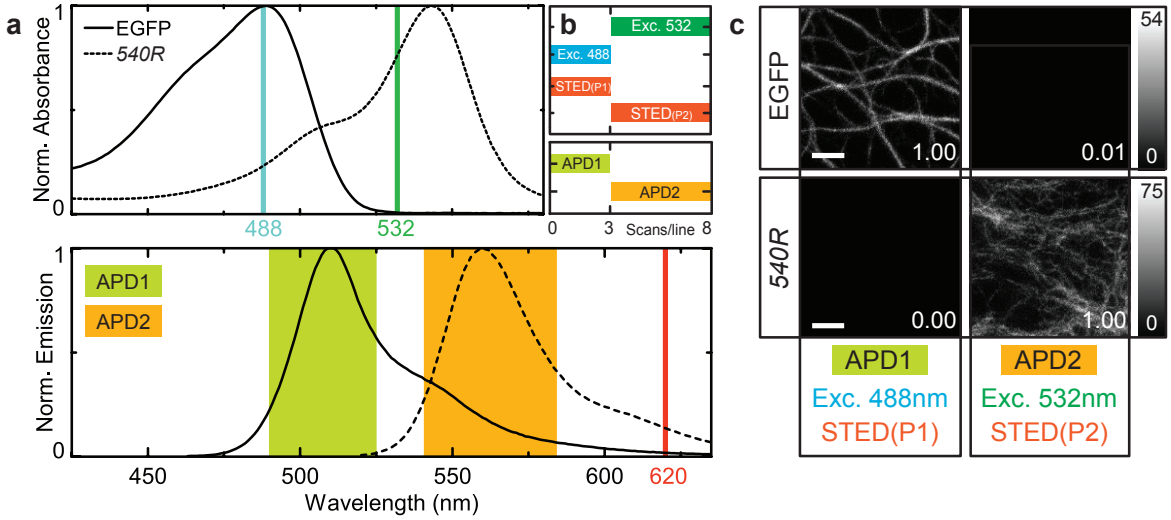

Figure 3.5: Dual-colour STED nanoscopy scheme for living samples. *(**a**) Normalized absorbance and emission spectra of the fluorescent protein EGFP and the membrane-permeating dye 540R-Halo along with the applied laser lines and detection windows of APD1 (green area) and APD2 (orange area). (**b**) Sequence of line steps (i.e. scan repetitions along the fast scanning direction) carried out for imaging of EGFP and 540R. Pixel counts of line repetitions were summed up. Additionally, µs-long breaks at every pixel were inserted. P1 and P2 denote different STED powers. (**c**) Application of the imaging sequence described in **b** on single colour stainings of living HeLa cells expressing keratin-EGFP (upper row) or vimentin-Halo-tag stained with 540R (lower row). Images are raw STED data with the same colourmap settings for the two detection channels. Values stated in the images refer to average pixel counts normalized to the brighter channel indicating signal cross-talk of ≤1% for both markers. Scale bars: 1 µm. Figure and caption reproduced from ref.* [180].

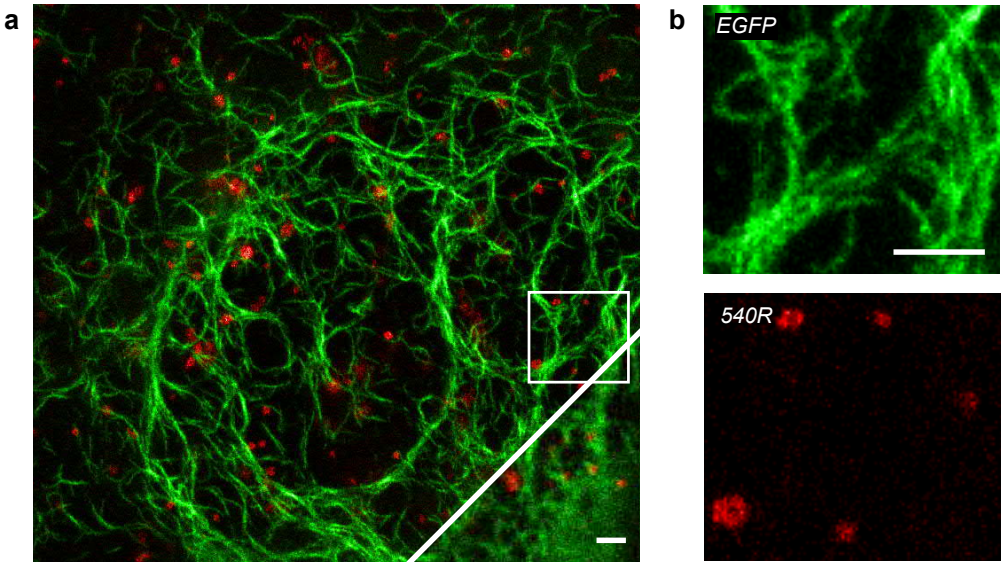

Figure 3.6: Dual-colour STED nanoscopy of living samples. *(**a**) STED image of a living HeLa cell expressing vimentin-EGFP (green) and Pex3-Halo-tag stained with 540R-Halo (red). The confocal counterpart is shown in the lower-right corner. (**b**) Close-ups of the region marked in **a** of the two colour channels, demonstrating the absence of cross-talk and the high signal-to-background ratio in both channels. Images were smoothed with a 1.0 pixel wide Gaussian. No linear unmixing was performed. Scale bars: 1 µm. Figure and caption reproduced from ref.* [180].

Furthermore, breaks of several microseconds were introduced at each pixel[1]. This splitting of the overall pixel dwell time into several smaller parts reduces the accumulation of triplet states and therewith potential bleaching of fluorophores [81;82]. Imaging of single-colour stainings with EGFP and *540R* showed channel cross-talks of ≤1% confirming the successful mutual suppression of excitation and detection overlaps by the imaging scheme (Fig. 3.5c). The scheme was applied to record dual-colour images of HeLa cells labeled with vimentin-EGFP and Pex3-Halo-*540R* (Fig. 3.6). Pex3 is the peroxisomal biogenesis factor 3 which encodes for a peroxin protein. Colour channels are very well separated without the need for linear unmixing as applied in previously published dual-colour STED modalities [143].

AlexaFluor488 and Atto532 were evaluated for dual-colour imaging of fixed samples. Their absorption and emission spectra fit also very well to the spectral properties of the setup (Fig. 3.1b). Accordingly, AlexaFluor488 was excited with 488 nm and detected by APD1, Atto532 by 532 nm and APD2. As outlined in the introduction, different STED powers might be optimal for the individual colour channels. To test this, single colour stainings of neurons were imaged with different STED power levels, whereby colour channels were again recorded quasi-simultaneously line by line. In region I of Figure 3.7, a low STED power of 15 mW was applied to both colour channels. Fine actin filaments labeled with Atto532 were recorded with high signal-to-background ratio. However, the punctate pattern of βII spectrin remains largely unresolved. In region III, 42 mW were applied along with both excitation lines, enabling the high-resolution rendition of the spectrin lattice. However, fine actin structures pervading the dendrite appear too dim due to the overshot STED power applied to Atto532. Multilevel STED now allows to assign different power levels to the individual excitation wavelengths during a single image scan, thereby accounting for the different STED power needs. Hence, in region II 42 mW of STED light were applied along with the 488 nm excitation and 15 mW along with 532 nm. This resulted in bright and well-resolved βII spectrin and actin channels.

The STED power effectively acting on the excited state of the fluorophore can be minimized by moving part of the STED pulse prior to the excitation pulse. Naturally, this works only for broad (≫200 ps) STED pulses and not for continuous-wave STED. Also, bright samples and photostable fluorophores may tolerate unnecessary high STED powers. However, especially when imaging living samples, the overall light doses shone on the sample has to be considered. By ensuring that each fluorophore is treated with adequate STED power, multilevel STED not only improves the image contrast but also avoids dispensable STED doses. Specifically, 32% of the total STED light portion employed in region III of Figure 3.7 could be saved in region II (same pixel dwell time for both channels). In the dual-colour recording of Figure 3.6, the

1 Detailed parameters of every presented image are given in the Methods section.

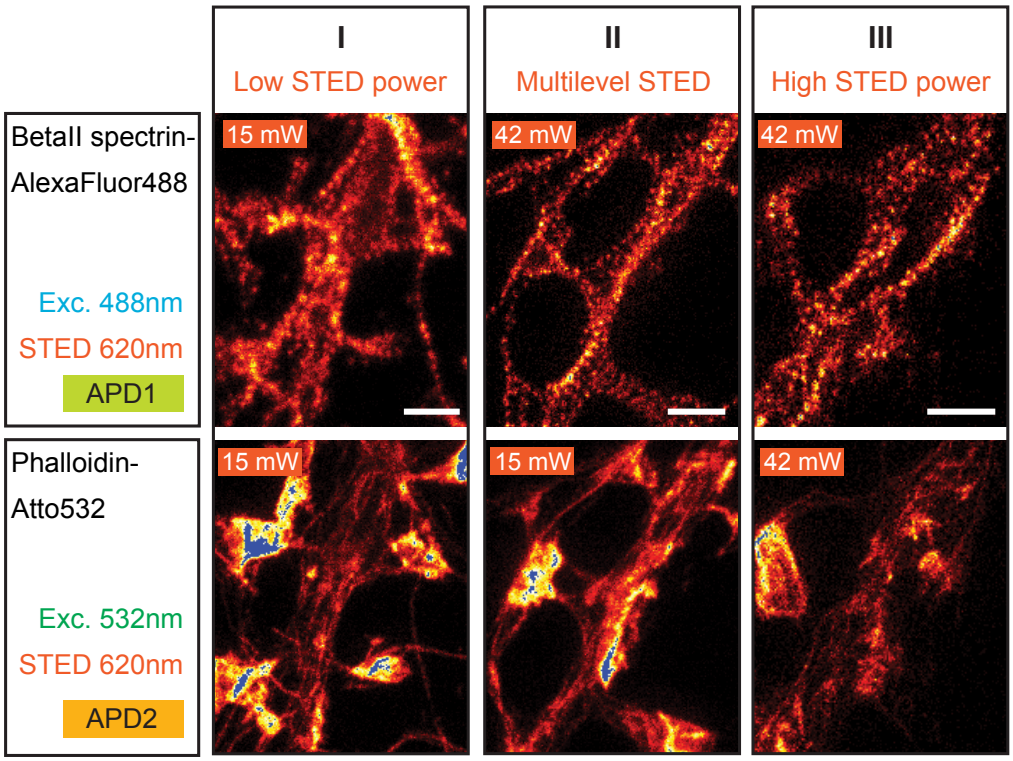

Figure 3.7: Effect of multilevel STED. *Three different regions I-III along the same dendrite of a hippocampal neuron were imaged either with fixed STED power (I and III) or with multilevel STED (II). For each region, the two stained structures βII spectrin-AlexaFluor488 (upper row) and phalloidin-Atto532 (lower row) were recorded line-wise with the excitation-detection combinations shown in the boxes on the left. In region I, a low STED power of 15 mW was used for imaging both markers whereas in region III, a constant STED power of 42 mW was applied. In region II, multilevel STED was applied assigning 42 mW of STED power to the 488 nm and 15 mW to the 532 nm excitation. This results in well-resolved and bright recordings of both structures at the same time. Concomitantly, STED dose was reduced by 26% in region II compared to III. Scale bars: 1 µm. Figure and caption reproduced from ref.* [180].

STED doses could even be reduced by 54% compared to standard STED modalities with a single STED power (5 line repetitions with 532 nm excitation plus 5 mW STED and 3 lines with 488 nm plus 36 mW STED). This makes multilevel STED even more interesting for applications with STED wavelengths below 600 nm which are stronger absorbed by living samples [137].

In the following, the AlexaFluor488-Atto532 pair was harnessed to image cytoskeletal structures of rat hippocampal neurons. Recent studies revealed characteristic patterns of actin and βII spectrin in axons and young dendrites [106;107;134;135]. It was shown that actin forms rings along axon initial segments with a periodic spacing of ~190 nm [134]. These rings are periodically intercalated by neurofascin [107]. Dual-colour 620 nm STED recordings of AlexaFluor488 highlighting neurofascin and phalloidin-Atto532 binding actin captures the subtle interplay of both structures as well (Fig. 3.8). Measurements were carried out according to the same scheme as in Fig. 3.7. Again, no linear unmixing is needed for high channel discrimination.

The versatility of the imaging system is further enhanced by combining the AlexaFluor488-

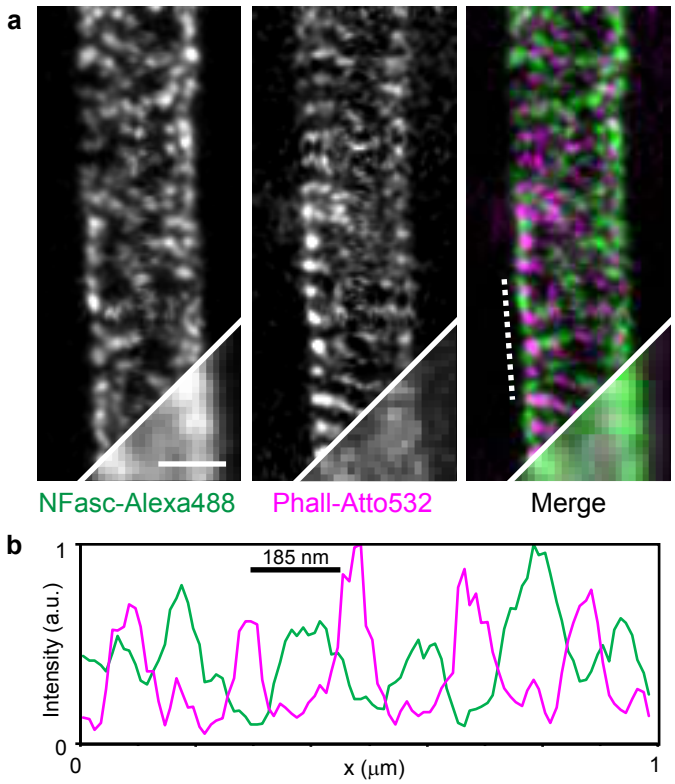

Figure 3.8: Dual-colour STED nanoscopy of fixed samples. *(**a**) STED image of a fixed hippocampal axon stained against neurofascin with AlexaFluor488 (left) and actin with phalloidin-Atto532 (centre) reveals the characteristic periodic lattice. Corresponding confocal images are shown in the lower-right corner. Scale bar: 500 nm. (**b**) Line profiles drawn parallel to the line shown in **a** for the two channels illustrate the interplay of neurofascin and actin. Counts of three pixels perpendicular to the line were summed up. Data of all panels were smoothed with a 1.0 pixel wide Gaussian. No linear unmixing was performed. Figure and caption reproduced from ref.* [180].

Atto532 pair with a long Stokes shift dye for three-colour nanoscopy of fixed samples. Since the long Stokes shift comes at the expense of broad excitation and emission bands, detection separation is not possible with low cross-talk. Hence, selective excitation of the long Stokes shift dye must be secured which is realized by shifting the excitation wavelength as far as possible away from the absorption bands of the other two dyes. Here, a diode laser emitting at 435 nm was chosen for excitation of Atto430LS (Fig. 3.1b). Three-colour imaging was carried out by applying the excitation wavelengths line by line (Fig. 3.9a). The number of STED power levels was technically limited to two so that the same STED power was applied to Atto430LS and AlexaFluor488. However, for the samples investigated here, one power level captures quite well both structure-dye pairs. Fluorescence emission was collected in four detection periods, which were APD1 along with 435 nm excitation, APD2 with 532 nm, as well as APD1 and APD2 simultaneously with 488 nm. In principle, three detection periods are sufficient for three dyes. However, the signal of APD2 during 488 nm excitation comes for free which is later used in the linear unmixing procedure to increase channel separation. Recording of more cross-talk channels was not possible with the available microscope control software. Colour channel separation

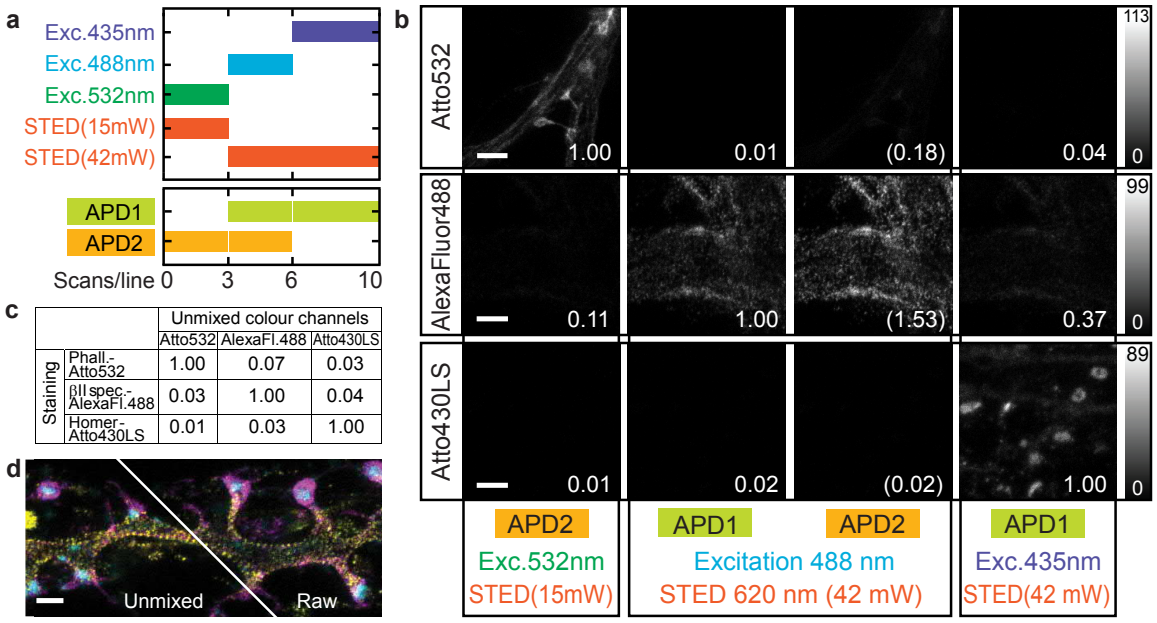

Figure 3.9: Three-colour STED nanoscopy evaluation. *(**a**) Sequence of repetitions along the fast scanning axis carried out for three-colour imaging. Pixel counts of lines with constant laser settings were accumulated. (**b**) Application of the imaging sequence shown in panel **a** on single colour stainings of hippocampal neurons: phalloidin-Atto532 (first row), βII spectrin-AlexaFluor488 (second row) and Homer-Atto430LS (third row). The panel shows raw STED images together with average pixel counts normalized to the brightest channel. Colour maps were adjusted to the brightest channel. Counts collected with APD2 during 488 nm excitation can be mainly attributed to AlexaFluor488 and can be used, when needed, for linear unmixing. (**c**) Matrix of normalized average pixel counts of the linearly unmixed datasets shown in **b**. For linear unmixing, all four detection channels per measurement were used. Cross-talk could be reduced to ≤7% for all markers. (**d**) Raw STED data of the experiment shown in Fig. 3.11a (magenta: phalloidin-Atto532 (excitation 532 nm, APD2); yellow: spectrin-AlexaFluor488 (exc. 488 nm, APD1); cyan: Homer-Atto430LS (exc. 435 nm, APD1)). Linear unmixed data is depicted on the left demonstrating mainly an improved signal in the AlexaFluor488 channel. Scale bars: 1 µm. Figure and caption reproduced from ref.* [180].

was again quantified by measuring single-colour stainings with the same imaging parameters (Fig. 3.9b). Atto532 and Atto430LS signals are separated with cross-talks ≤4% in the raw data. Although the absorption maximum of AlexaFluor488 is about 55 nm away from the 435 nm line, there is still some excitation cross-section which leads to about 37% cross-talk of AlexaFluor488 in the Atto430LS channel. However, all structures are readily identified in the raw data which greatly eases sample and data evaluation during acquisition (Fig. 3.9d). The signal of APD2 acquired during 488 nm excitation mainly stems from AlexaFluor488. By linear unmixing [151;185] of all four detection channels, the signal in the AlexaFluor488 channel is further increased and even more important all cross-talks are reduced to ≤7% (Fig. 3.9c,d). The unmixing matrix was measured in the single-colour images recorded with the same parameters and setup configuration. In conclusion, the combination of two conventional and a long Stokes shift dye together with the carefully chosen spectral properties of the setup facilitates simultaneous three-colour imaging with well-separated and intrinsically co-aligned channels.

3.3.3 Three-colour imaging with 775 nm STED

As outlined, the 775 nm STED line is nowadays the most widely used for imaging of fixed samples. Far-red emitting dyes like KK114, STAR635 and Atto647N are very bright, extremely photostable and facilitate specific immunostainings with low background. Down to 20 nm resolutions are enabled by fibre lasers with nanosecond-long pulses and energies of 30 nJ/pulse (equal to 1200 mW average power)[186]. Hence, a three-colour 775 nm STED scheme would have a great potential and would be interesting for many applicants.

Commercially available 775 nm STED systems are typically equipped with two excitation lasers of 561/590 nm and 640 nm and two detection channels capturing the fluorescence of dyes like Atto594 or STAR580 and Atto647N or KK114, respectively[170;171] (Fig. 3.10a). In analogy to the presented 620 nm scheme, a third, blue-shifted excitation laser synchronized to the STED laser is needed. In some modalities, an additional 485 nm diode laser is built in for imaging of GFP. Synchronizing it to the 775 nm STED laser enables STED microscopy of long Stokes shift dyes like Atto490LS and STAR470SXP (Fig. 3.10a). In doing so, three-colour images were obtained again by line-interleaved scanning with the three excitation beams (see Fig. 3.14 in the following section). STAR635 emission was excited at 640 nm and detected with APD2, STAR580 at 561 nm and with APD1, and Atto490LS at 485 nm and with APD2. Colour separation was quantified by measuring single-colour stainings (Fig. 3.10b). All cross-talks were found to be ≤13% in the raw data whereby sample autofluorescence was even not substracted.

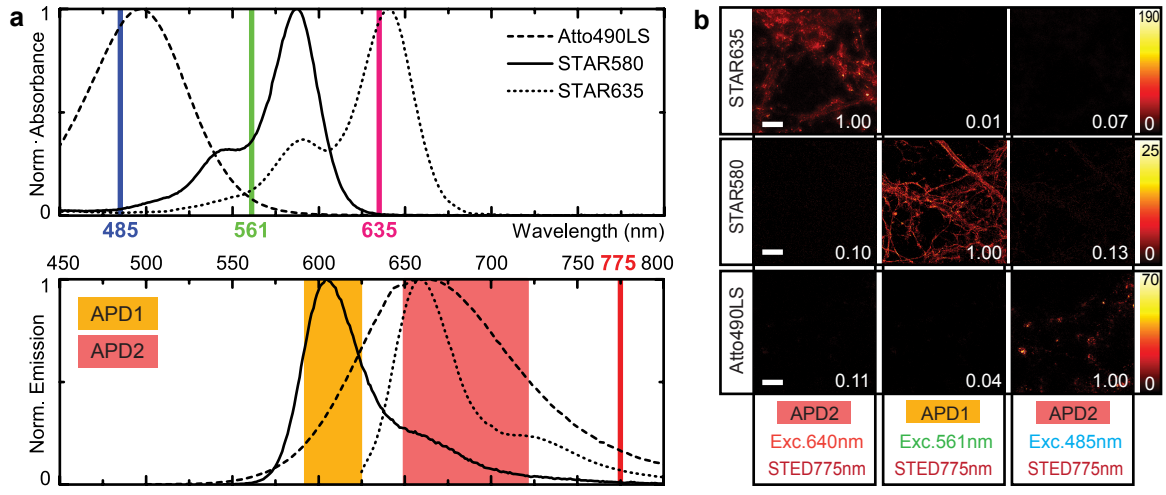

Figure 3.10: Three-colour 775 nm STED scheme. *(**a**) Normalized absorption and emission spectra of the dyes Atto490LS, STAR580, and STAR635 together with excitation and STED wavelengths. Two detection channels capture fluorescence between 605 nm and 625 nm (APD1) and between 650 nm and 720 nm (APD2), respectively. (**b**) Three-colour imaging of single colour stainings of hippocampal neurons: phalloidin-STAR635 (first row), βII spectrin-STAR580 (second row) and Homer-Atto490LS (third row). The panel shows raw STED images together with average pixel counts normalized to the brightest channel. Colour maps were adjusted to the brightest channel. Cross-talk is ≤13% in all channels. Scale bars: 5 µm. Figure adapted from ref.*[180].

Since the microscope was a commercial system, implementation of multilevel STED was not possible. However, in the following experiments the power acting upon STAR635 was reduced by shifting the rising edge of the ~1 ns broad STED pulse a few 100 ps prior to the edge of the 640 nm excitation pulse. Yet, the STED dose reducing effect of multilevel STED is only obtained when truly modulating the power of the STED beam without the need for detuning the pulse superposition. In the following, the potential of the two schemes becomes evident by three-colour imaging of the cytoskeletal organization in hippocampal neurons.

3.3.4 Cytoskeletal organization at synaptic sites of hippocampal neurons

Recently, STED and STORM nanoscopy revealed characteristic subdiffraction sized periodic patterns of actin and βII spectrin along the distal axons[134] and the dendrites[107;135] of hippocampal neurons. In fact, the periodic subcortical lattice was shown to be an ubiquitous feature of neurites in both the central and peripheral nervous systems[136;157]. The pattern was observed both in fixed samples stained with phalloidin as well as in living samples labeled with SiR-Actin[106], thereby ruling out potential labeling artifacts. However, all those studies were carried out on neurons not longer than 15 days *in vitro* where spines are still not or poorly developed. So, it is still an open question what happens to the periodic lattice, when they loose their regular tubular shape due to the outgrowth of spines, as well as if the lattice is present at pre- and post-synaptic sites. Three-colour STED nanoscopy is predestinated for addressing these questions, since concomitant labelings of actin, spectrin as well as a marker for pre- or post-synaptic sites are needed to be imaged with subdiffraction resolution.

Measurements were carried out on neurons being 17-30 days *in vitro*. βII spectrin and actin were stained by AlexaFluor488 and phalloidin-Atto532, respectively. The pre-synaptic marker Bassoon or its post-synaptic counterpart Homer were labeled by Atto430LS. Three-colour images were recorded according to the scheme shown in Fig. 3.9. All colour channels in the obtained images are bright and well resolved, with the respective structures identified unequivocally (Fig. 3.11). Filamentous actin is highly enriched in the dendrites and especially in the spine heads[152] (Fig. 3.11a). Due to the presence of numerous actin bundles pervading the dendrites, the fine and usually very dim cortical actin structures are difficult to identify. Nevertheless, actin intercalating the spectrin pattern is observed in few cases (Fig. 3.12). βII spectrin is found to show a sharp periodic organization along all the dendrites decorated with spines, indicating the presence of the subcortical actin/spectrin lattice also in mature neurons. The spectrin pattern even enters into the thicker spine necks. However, it is generally absent from post-synaptic densities (PSD) highlighted by the Homer staining (Fig. 3.11a,b and 3.13a). At times, βII spectrin puncta are observed next to Homer hotspots, where actin levels are reduced concomitantly. The same arrangement is found in images recorded with the 775 nm STED

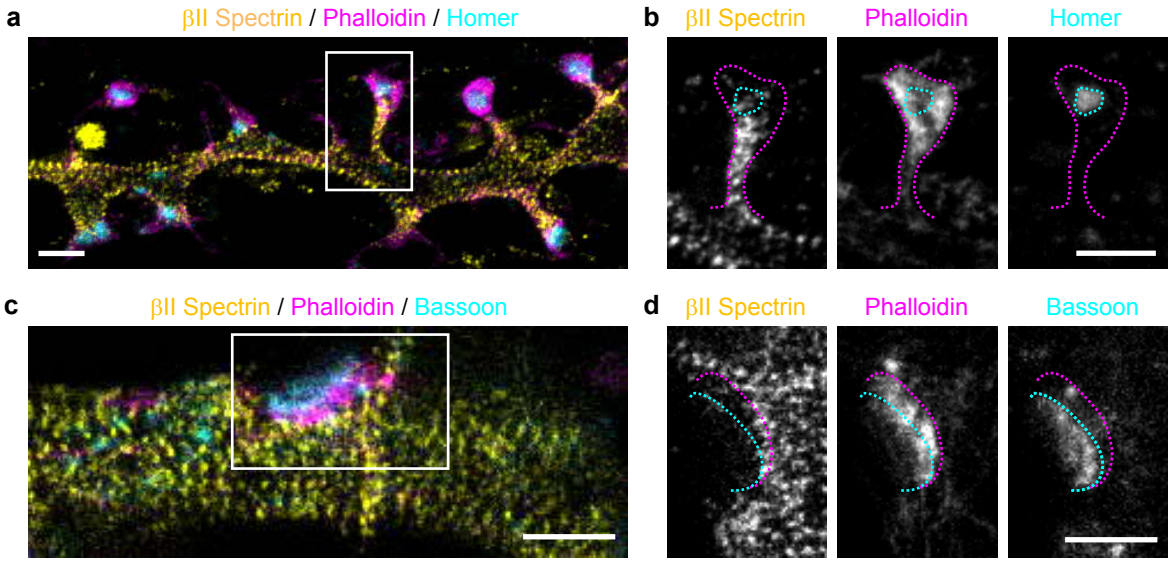

Figure 3.11: The subcortical periodic actin/βII spectrin lattice is discontinued at synaptic sites. *(**a**) Three-colour STED image of a dendrite decorated with spines and stained with βII spectrin (AlexaFluor488, yellow), phalloidin (Atto532, magenta), and Homer (Atto430LS, cyan) shows the periodic spectrin organization. (**b**) Single-channel images of the spine indicated in **a**. Magenta and cyan dashed lines highlight the shape of the spine and the position of the PSD, respectively. βII spectrin enters into the spine neck but does not reach the PSD. (**c**) Same as **a**, but for the pre-synaptic site, identified by Bassoon staining instead of Homer. (**d**) Single channel images of the boxed area in **c**. Magenta and cyan dashed lines highlight the position of the actin cage and of Bassoon, respectively. All panels of the figure show linear unmixed STED data, smoothed with a 1.0 pixel wide Gaussian function. Raw data of the image in panel **a** is shown in Fig. 3.9d. Scale bars: 1 µm. Figure and caption reproduced from ref.[180].*

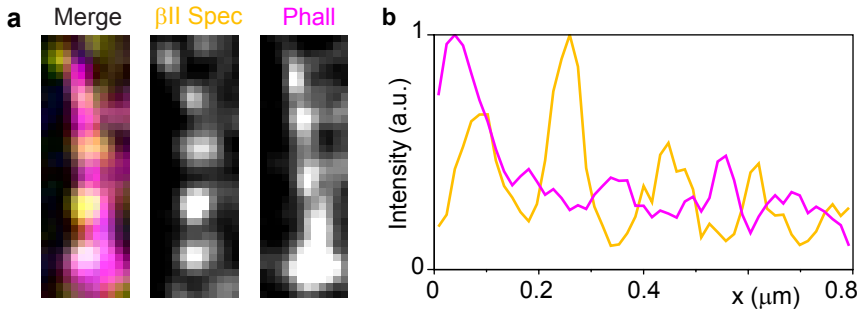

Figure 3.12: Actin and βII spectrin pattern along mature dendrites. *(**a**) Close-up of Fig. 3.11a showing the actin/βII spectrin alternating pattern along mature dendrites in between the spines (300x900 nm^2 section). (**b**) Line profile of 5 pixel width measured on raw data along the dendrite of **a** showing the interspaced peaks. Figure adapted from ref.[180].*

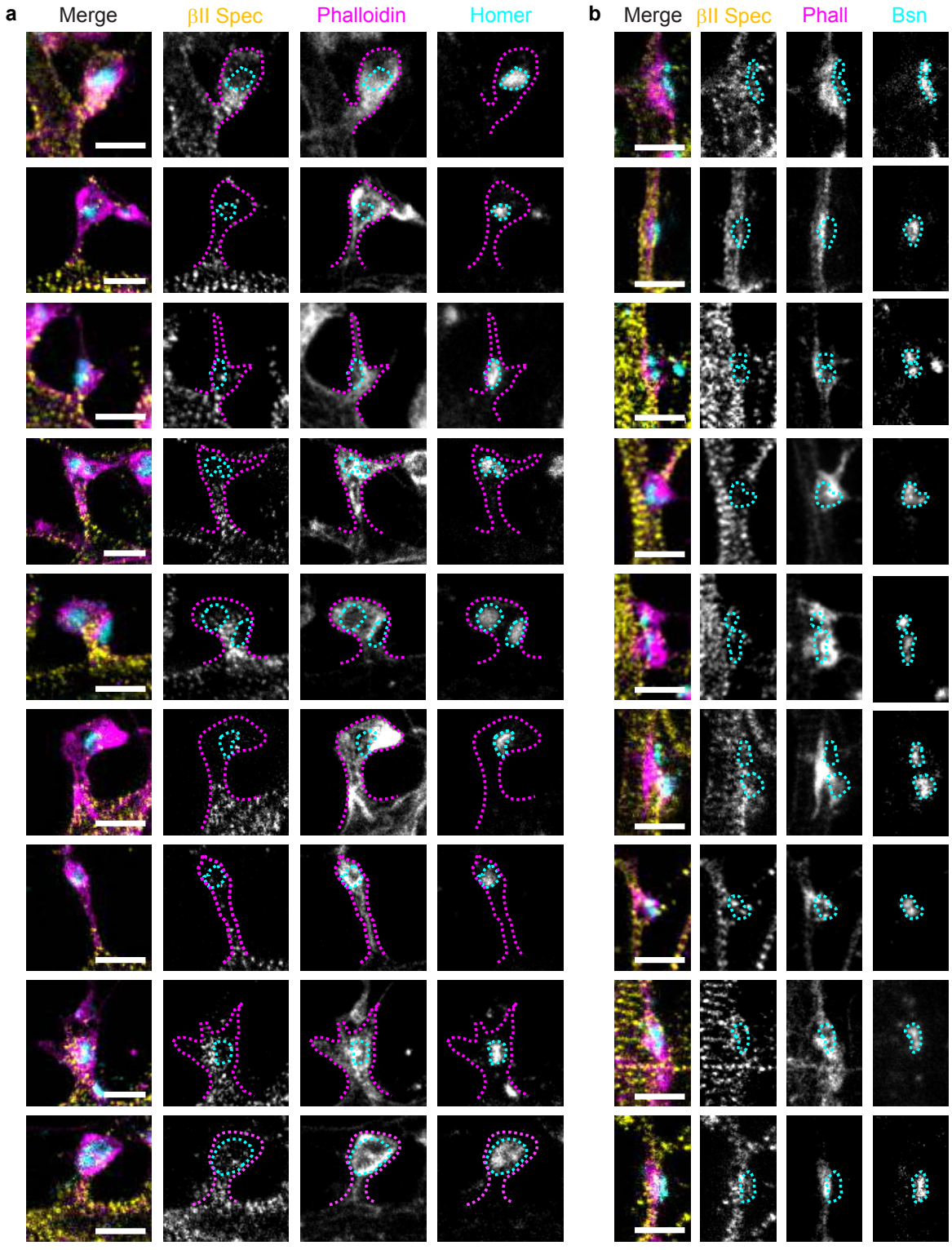

Figure 3.13: Actin and βII spectrin organization at pre- and post-synaptic sites. *(**a**) Gallery of dendritic spines stained against βII spectrin (AlexaFluor488, yellow), phalloidin (Atto532, magenta), and Homer (Atto430LS, cyan). Merged and corresponding single channel images are shown. Magenta and cyan dashed lines highlight the shape of the spine and the position of the PSD, respectively. (**b**) Same as **a**, but for the pre-synaptic site, identified by Bassoon (Bsn) staining. The cyan dashed line highlights the position of the Bassoon puncta. The figure shows linear unmixed STED data, smoothed by convolution with a 1.0 pixel wide Gaussian. Scale bars: 1 µm. Figure and caption adapted from ref.* [180].

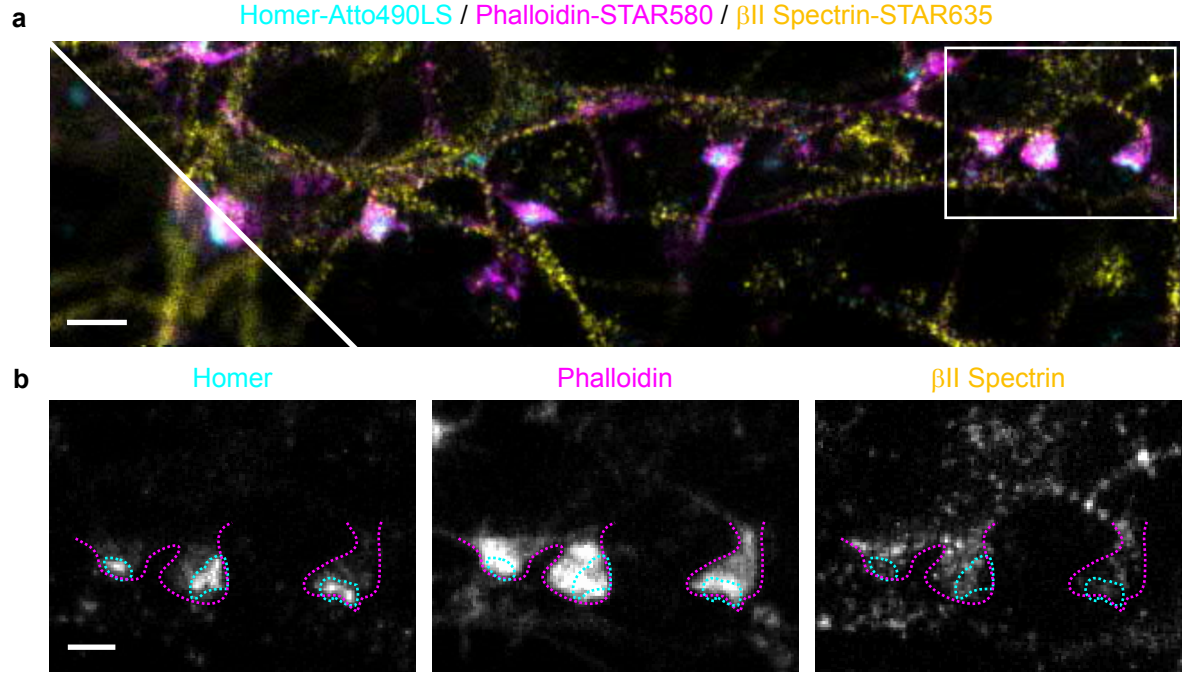

Figure 3.14: Three-colour nanoscopy with a commercial 775 nm STED system. *(**a**) Raw STED image of hippocampal neurons stained with Homer-Atto490LS, phalloidin-STAR580 and βII spectrin-STAR635. A confocal comparison is depicted in the lower-left corner. (**b**) Single colour channels of the raw STED image of the region marked in **a**. Images show similar protein distributions compared to STED at 620 nm. Scale bars: 1 µm. Figure and caption reproduced from ref.* [180].

system (Fig. 3.14). Also at Bassoon-highlighted pre-synaptic sites, βII spectrin content appears lowered and the periodic pattern is discontinued (Fig. 3.11c,d and 3.13b). In most of cases, an actin enrichment is observed adjacent to the active zone virtually edging Bassoon hotspots. In summary, the actin/βII spectrin subcortical periodic lattice is present in all neurites of mature neurons. But it is absent from pre- and post-synaptic sites. Very recently, similar results obtained from STORM measurements were published [136].

3.4 Conclusions and Discussion

The above experiments show that the actin/spectrin pattern is ubiquitous not only in axons and dendrites of young neurons without spines but also in mature dendrites which developed spines (Fig. 3.15). In fact, actin is forming an angular lattice which is connected along the axon or dendrite by βII spectrin tetramers giving rise to the ~190 nm periodicity [134]. This arrangement could be responsible of providing both stable and elastic support to the membrane which renders the dendrites and especially the long axons resistant against mechanical stress. The absence of the lattice at synaptic sites can be explained with the need for plasticity and rapid re-arrangements occurring at these highly specialized and dynamic locations. Indeed, morphological and functional changes would require the disassembly of the subcortical lattice [187].

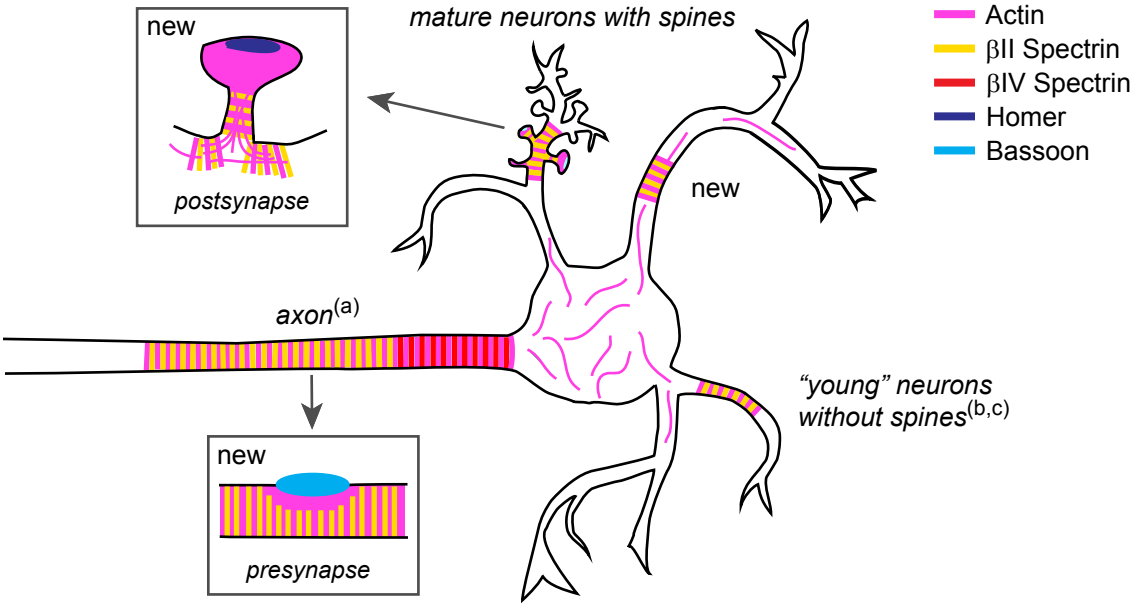

Figure 3.15: Actin/spectrin organization in neurons. *Updated simplified picture of the actin, βII and βIV organization in hippocampal neurons. Periodic patterns are only exemplarily drawn in at few position, but are in fact present throughout the neurites. The situation at the cell body is still unknown. Patterns in axons and young neurons were published by (a) Xu et al.[134], (b) Zhong et al.[135] and (c) D'Este et al.[107]. Very recently, patterned structures in mature dendrites and spines were also identified by STORM imaging[136].*

Furthermore, the lattice might impede the fusion of vesicles with the membrane[188]. On the other hand, further spectrin isoforms like βIV might be specifically enriched at synaptic sites substituting for the scaffolding function of βII spectrin[189;190], similar to what is found in the axon initial segment and at the nodes of Ranvier with βIV spectrin[135;191].

These results together with the proof-of-principle images obtained in living samples demonstrate the potential of the presented STED modality. 620 nm STED is viable with several synthetic and genetically encoded markers whereby the obtained resolution of down to ~35 nm with synthetic dyes is similar to those provided by 590 nm STED systems. Additional tests with a 631 nm STED laser yielded images with slightly lower resolution without increasing the palette of accessible markers (data not shown). Furthermore, the 620 nm line allows live-cell two-colour nanoscopy with high channel discrimination based on EGFP and the cell-penetrating *540R* dye. Ongoing dye development will most like lead to three-colour imaging with live-cell compatible synthetic markers in near future. Moreover, the 620 nm setup is compatible with RESOLFT[34] and protected STED[70] nanoscopy with rsEGFPs, since the needed beams for protein switching can be easily implemented.

The presented microscope scheme forms a basis for establishing routine multicolour imaging applications without the need for elaborate setup alignments, extended data processing, or equipment for fluorescence lifetime separation[165]. With multilevel STED a general strategy

is introduced which both optimizes the image quality and reduces the required STED light dose which is especially beneficial when performing live-cell nanoscopy. Multilevel STED is not limited to line-interleaved modalities, but can be carried out pixel- or even pulse-wise using respectively fast acousto- or electro-optic modulators. Here, the number of power levels was technically limited to two. But, in principle, one or more power levels can be assigned to each excitation line thereby further enlarging the parameter freedom. Multilevel STED is also applicable to other multicolour schemes which harness a single STED doughnut. Especially in the presence of significant excitation cross-talk, multilevel STED will be able to reduce photobleaching.

Of course, the imaging scheme can also be extended to 3D nanoscopy. Owing to the single-doughnut design, a second STED beam stemming from the same laser and engineered as bottle beam ('z-doughnut')[28] is readily added. Or, even better, the corresponding phase shifts can be imprinted on a single beam. 3D superresolution would for example be helpful for a more detailed characterization of the complex structure of synaptic sites.

3.5 Materials and Methods

In this section, the publication Sidenstein *et al. Scientific Reports* **6**, 26725 (2016) is cited from here on:

3.5.1 STED nanoscope

"STED pulses (620 nm, ~600 ps FWHM, 40 MHz) were delivered by a fibre laser (MPB Communications Inc., Montreal, Quebec, Canada). A part of the experiments were carried out with a Raman-shifted fibre laser (Rainbow prototype, IPG Photonics, Mountain View, CA, USA) operating at 618 nm with a repetition rate of 20 MHz (pulse width similar to the MPB laser). Both STED lasers provided similar results. Pulsed diode lasers (488 nm: PicoTA, Toptica Photonics, Graefelfing, Germany and PicoQuant, Berlin, Germany; 435 nm: LDH-D-C-430; 532 nm: LDH-P-FA-530, both PicoQuant) served as excitation light sources and were triggered by the STED laser. Pulse widths of the excitation lasers: ~150 ps. All lasers were spectrally filtered, passed through acousto-optic modulators (AOMs) and were subsequently coupled into polarization-maintaining single-mode fibres (exception: the MPB laser was not fibre-coupled). Fast alternation between two levels of the analogue voltage at the AOM defining the STED power was accomplished by home-built electronics. STED light was passed through a vortex phase-plate (VPP1a, RPC Photonics, Rochester, NY, USA, 620 nm vortex mask) giving rise to a doughnut-shaped focal spot. Beams were combined by dichroic mirrors and notch filters and coupled into the back aperture of an oil-immersion objective lens

with NA 1.4 (HCX-PL-APO 100x/1.4-0.7 OIL CS, Leica Microsystems, Wetzlar, Germany). Scanning in the lateral directions was accomplished by a 'Quad-Scanner'[54], which consists of four galvanometric scan mirrors. For fine focus control and scanning in the axial direction, the objective lens was moved by a piezo translator (z-piezo, Mipos 100PL CAP, Piezosystem Jena, Jena, Germany). The fluorescence light was collected by the same objective lens, de-scanned and separated from the laser light, and focused onto a pinhole of variable size (MPH16, Thorlabs, Newton, NJ, USA). Depending on the sample, the pinhole diameter was varied between sizes corresponding to 0.7-1.0 times the Airy disk at this position. The transmitted fluorescence light was then further spectrally separated, filtered and focused on two avalanche photodiodes (each SPCM-AQRH-13, Excelitas, Waltham, MA, USA). The detection was time-gated on the µs- and ns-timescale by home-built electronics and by an FPGA card (PCIe-7852R, National Instruments, Austin, TX, USA), respectively. Image acquisition and microscope control were performed with the software ImSpector (Max-Planck Innovation).

3.5.2 Image acquisition and analysis

All power values stated in this work refer to the power entering the back aperture of the objective lens. This means that the actually applied power is typically 10-30% lower due to losses at the optical interfaces presented by the objective lens and the sample. Linear unmixing was performed with the SpectralUnmixing plugin (rsbweb.nih.gov/ij/plugins/spectral-unmixing.html) of ImageJ (imagej.nih.gov/ij/) and was applied where indicated. The unmixing matrix was obtained from measurements with the same parameters on single-colour stainings. No deconvolution was performed. Cross-talks of colour channels were determined by calculating the average pixel counts normalized to the brightest channel. Where indicated, images were smoothed by convolution with a 1.0 pixel wide Gaussian using ImSpector. Some neuron images were rotated using bicubic interpolation in ImageJ. Line profiles were fit using the multi-peak fitting function in OriginPro2015. Pixel counts of repetitive scans along the fast scan axis were summed up and cumulative counts are reported.

Imaging parameters

Figure 3.2: Customized DNA origami structures were obtained from GattaQuant, Braunschweig, Germany. **b**, 10 scans along fast scan axis with 532 nm excitation (0.9 µW) + 620 nm STED (29 mW), detection with APD2. Pixel dwell time: 4.5 µs. Pixel size: 10 nm. **c**, 8 scans along fast scan axis with 488 nm excitation (1.7 µW) + 620 nm STED (39 mW), detection with APD1 and APD2, and signals were summed. Pixel dwell time: 2 µs. Pixel size: 16.5 nm. **d**, 3 scans along fast scan axis with 435 nm excitation (0.9 µW) + 620 nm STED (40 mW), detection with APD1 and APD2, and signals were summed. Pixel dwell time: 20 µs. Pixel size:

15 nm. Images smoothed by convolution with a 1.0 pixel wide Gaussian. Line profiles taken on raw image data, averaged over 2 or 3 pixels perpendicular to the direction of the profile.

Figure 3.3: **a**, 3 scans along fast scan axis with 488 nm excitation (1.7 µW) + 620 nm STED (36 mW), detection with APD1. Pixel dwell time: 13 µs + 5 µs break. Pixel size: 30 nm. **b**, 2 scans along fast scan axis with 488 nm excitation (1.1 µW, 20 MHz) + 618 nm STED (16 mW, 20 MHz), detection with one APD filtered with a 550/49 bandpass. Pixel dwell time: 30 µs. Pixel size: 20 nm. **c**, 2 scans along fast scan axis with 488 nm excitation (1.7 µW) + 620 nm STED (26 mW), detection with APD1 and APD2 and signals were summed up. Pixel dwell time: 10 µs + 5 µs break. Pixel size: 23 nm. **d**, 2 scans along fast scan axis with 532 nm excitation (2.6 µW, 20 MHz) + 618 nm STED (10 mW, 20 MHz), detection with APD2. Pixel dwell time: 25 µs. Pixel size: 18 nm. Line profiles were averaged over a 10 pixels, b 2 pixels, c 10 pixels, d 6 pixels perpendicular to the direction of the profile.

Figure 3.5: **c**, Sequence along fast scan axis: 3 scans with 488 nm excitation (1.7 µW) + 620 nm STED (P1: 36 mW), detection with APD1; 5 scans with 532 nm excitation (1.0 µW) + 620 nm STED (P2: 12 mW), detection with APD2. Pixel dwell time: 13 µs + 5 µs break. Pixel size: 30 nm. Figure shows raw data.

Figure 3.6: Sequence along the fast scan axis: 3 scans with 488 nm excitation (1.7 µW) + 620 nm STED (36 mW), detection with APD1; 5 scans with 532 nm excitation (1.0 µW) + 620 nm STED (5 mW), detection with APD2. Pixel dwell time: 13 µs + 5 µs break. Frequency of repetitions along fast scan axis: 50 Hz. Progression along slow scan axis: 6.2 Hz. Pixel size: 30 nm.

Figure 3.7: Scan sequence along fast scan axis: 3 scans with 532 nm excitation (1.7 µW) + 620 nm STED (15 mW or 42 mW), detection with APD2; 3 scans with 488 nm excitation (2.4 µW) + 620 nm STED (15 mW or 42 mW), detection with APD1. Pixel dwell time: 7 µs + 5 µs break. Pixel size: 25 nm. Figure shows raw data.

Figure 3.8: Sequence along fast scan axis: 3 scans with 488 nm excitation (1.8 µW) + 620 nm STED (36 mW), detection with APD1; 3 scans with 532 nm excitation (1.0 µW) + 620 nm STED (15 mW), detection with APD2. Pixel dwell time: 7 µs + 5 µs break. Pixel size: 20 nm. Images were smoothed with 1.0 pixel wide Gaussian.

Figure 3.9: **b**, Sequence along fast scan axis: 3 scans with 532 nm excitation 1.7 µW) + 620 nm STED (15 mW), detection with APD2; 3 scans with 488 nm excitation (2.4 µW) + 620 nm STED (42 mW), detection with APD1 and APD2; 4 scans with 435 nm excitation (3.0 µW) + 620 nm STED (42 mW), detection with APD1. Pixel dwell time: 7 µs + 5 µs break. Pixel size: 25 nm. Panel shows raw data. **d**, Same dataset shown in Fig. 3.11a.

Figure 3.10: Measurements were performed with a commercial STED system (2C STED775, Abberior Instruments, Göttingen, Germany) equipped with the excitation lines 485 nm, 561 nm

and 640 nm, a STED laser at 775 nm (40 MHz) and two gated detection channels. Sequence along fast scan axis: 3 scans with 640 nm excitation + 775 nm STED (STED pulse several 100 ps before excitation pulse), detection with APD2; 3 scans with 561 nm excitation + 775 nm STED, detection with APD1; 5 scans with 485 nm excitation + 775 nm STED, detection with APD2. Pixel dwell time: 7 µs. Pixel size: 30 nm.

Figure 3.11: **a** and **c**, Sequence along fast scan axis: 3 scans with 532 nm excitation (1.7 µW) + 620 nm STED (15 mW), detection with APD2; 3 scans with 488 nm excitation (2.4 µW) + 620 nm STED (42 mW), detection with APD1 and APD2; 4 scans with 435 nm excitation (3.0 µW) + 620 nm STED (42 mW), detection with APD1. Pixel dwell time: 7 µs + 5 µs break. Pixel size: 25 nm. Images were linearly unmixed (see above) and smoothed with 1.0 pixel wide Gaussian.

Figure 3.13: Sequence along fast scan axis: 3 scans with 532 nm excitation (1.7 µW) + 620 nm STED (15 mW), detection with APD2; 3 scans with 488 nm excitation (2.4 µW) + 620 nm STED (42 mW), detection with APD1 and APD2; 4 scans with 435 nm excitation (3.0 µW) + 620 nm STED (42 mW), detection with APD1. Pixel dwell time: 7 µs + 5 µs break. Pixel size: 25 nm or 30 nm.

Figure 3.14: Abberior system: Sequence along fast scan axis: 3 scans with 640 nm excitation + 775 nm STED (STED pulse several 100 ps before excitation pulse), detection with APD2; 3 scans with 561 nm excitation + 775 nm STED, detection with APD1; 3 scans with 485 nm excitation + 775 nm STED, detection with APD2. Pixel dwell time: 7 µs. Pixel size: 30 nm.

3.5.3 Cell culture, transfection and labeling of living cells

HeLa cells were plated on glass coverslips and transfected on the next day with a plasmid encoding a fusion of a fluorescent protein or Halo-tag with the protein of interest. About 24 h after transfection, cells were washed and imaged in HEPES-buffered Dulbecco's modified Eagle's medium (HDMEM) without phenol red. Cells transfected with a Halo-tag-containing plasmid were incubated in a 1 µM solution of 540R-Halo in DMEM for 20-30 min under growth conditions. After that, cells were washed in HDMEM and incubated for another 20-30 min in DMEM under growth conditions. Cells were imaged in HDMEM without phenol red.

3.5.4 Primary hippocampal neuron culture preparation

Cultures of hippocampal neurons were prepared from Wistar rats of mixed sex at postnatal day P0-P1 in accordance with Animal Welfare Law of the Federal Republic of Germany (Tierschutzgesetz der Bundesrepublik Deutschland, TierSchG) and the Regulation about animals used in experiments (1st August 2013, Tierschutzversuchsverordnung). For the procedure of sacrificing rodents for subsequent preparation of any tissue, all regulations given in §4 TierSchG

are followed. Since sacrificing of animals is not an experiment on animals according to §7 Abs. 2 Satz 3 TierSchG, no specific authorization or notification is required. Cells were plated on coverslips coated with 100 µg/mL polyornithine (Sigma-Aldrich, cat. P3655) and 1 µg/mL laminin (BD Bioscience, cat. 354232). Neuronal cultures were maintained in Neurobasal medium (Gibco, cat. 21103049) supplemented with 2% B27 serum-free supplement (Gibco, cat. 17504044), 2 mM L-glutamine (Gibco, cat. 25030) and pen/strep (100 units/mL and 100 µg/mL, respectively, BiochromAG, cat. A2213). On the day after plating, 5 µM cytosine β-D-arabinofuranoside (Sigma, cat. C1768) was added to the cultures. For this study, neuronal cultures at 17-30 days in vitro in which spines were fully developed were used.

3.5.5 Immunostaining

Cells were washed with PBS and fixed in 4% PFA in PBS (pH 7.4) for 20 min at room temperature (RT), quenched with NH4Cl and glycine (100 mM each) for 5 min, permeabilized with 0.1% Triton X-100 for another 5 min, and blocked with BSA 1% in PBS for 30 min. Both primary and secondary antibodies and phalloidin incubations were performed in PBS for 1 h at RT or overnight at 4 °C. Samples were mounted in Mowiol supplemented with DABCO. The antibodies used in this study are: anti-pan-neurofascin (UC Davis/NIH NeuroMab Facility, clone A12/18 cat. 75-172, 1:400 dilution); anti-βII spectrin (BD Biosciences, cat. 612563, 1:400 dilution); anti-Homer 1 (Synaptic Systems, cat. 160 003, 1:200 dilution); anti-Bassoon (Synaptic Systems, cat. 141 003 and 141 004, 1:200 dilution); anti-mouse AlexaFluor488 (Invitrogen, cat. A11001, 1:200 dilution); anti-mouse STAR635 (Abberior, cat. 2-0002-002-0, 1:100 dilution). Anti-rabbit secondary antibody (Dianova, cat. 111-005-003) and anti-guinea-pig secondary antibody (Dianova, cat. 706-005-148) were custom-labeled with Atto430LS dye (AttoTech, cat. AD 430LS-31) or Atto490LS dye (AttoTech, cat. AD 490LS-31). Phalloidin was coupled to Atto532 (AttoTech, cat. AD 532-81, 1:100 dilution) or to STAR580 (Abberior, cat. 2-0205-005-6, 1:100 dilution).”

Bibliography

[1] Abbe, E. (1873) *Archiv für Mikroskopische Anatomie* **9(1)**, 413–468.

[2] Denk, W., Strickler, J. H., and Webb, W. W. (1990) *Science* **248**, 73–76.

[3] Schönle, A., Hänninen, P. E., and Hell, S. W. (1999) *Annalen der Physik* **8(2)**, 115–133.

[4] Frohn, J. T., Knapp, H. F., and Stemmer, A. (2000) *Proceedings of the National Academy of Sciences of the United States of America* **97(13)**, 7232–7236.

[5] Gustafsson, M. G. L. (2000) *Journal of Microscopy* **198(2)**, 82–87.

[6] Gustafsson, M. G. L., Shao, L., Carlton, P. M., Wang, C. J. R., Golubovskaya, I. N., Cande, W. Z., Agard, D. A., and Sedat, J. W. (2008) *Biophysical Journal* **94(12)**, 4957–4970.

[7] Hell, S. and Stelzer, E. H. K. (1992) *Journal of the Optical Society of America A* **9(12)**, 2159.

[8] Gustafsson, Agard, and Sedat (1999) *Journal of Microscopy* **195(1)**, 10–16.

[9] Ash, E. A. and Nicholls, G. (1972) *Nature* **237(5357)**, 510–512.

[10] Synge, E. H. (1928) *Philosophical Magazine* **6**, 356–362.

[11] Betzig, E. and Trautman, J. K. (1992) *Science* **257(5067)**, 189–195.

[12] deBakker, B. I., deLange, F., Cambi, A., Korterik, J. P., van Dijk, Erik M H P, van Hulst, N. F., Figdor, C. G., and Garcia-Parajo, M. F. (2007) *ChemPhysChem* **8(10)**, 1473–1480.

[13] van Zanten, T. S., Gomez, J., Manzo, C., Cambi, A., Buceta, J., Reigada, R., and Garcia-Parajo, M. F. (2010) *Proceedings of the National Academy of Sciences of the United States of America* **107(35)**, 15437–15442.

[14] Haugstad, G. (2011) Understanding atomic force microscopy: Basic modes for advanced applications, Wiley-Blackwell, Oxford.

[15] Vancso, G. J. and Schönherr, H. (2010) Scanning force microscopy of polymers, Springer Laboratory, Springer, Berlin and London.

[16] Arturo M. Baró and Ronald G. Reifenberger, (ed.) (2012) Atomic force microscopy in liquid: Biological applications, Wiley-VCH, Weinheim, Germany 2nd edition.

[17] Hain, N., Wesner, D., Druzhinin, S. I., and Schönherr, H. (2016) *Langmuir*.

[18] Chiantia, S., Ries, J., Chwastek, G., Carrer, D., Li, Z., Bittman, R., and Schwille, P. (2008) *Biochimica et biophysica acta* **1778(5)**, 1356–1364.

[19] Werner, J. H., Montano, G. A., Garcia, A. L., Zurek, N. A., Akhadov, E. A., Lopez, G. P., and Shreve, A. P. (2009) *Langmuir* **25(5)**, 2986–2993.

[20] Harke, B., Chacko, J. V., Haschke, H., Canale, C., and Diaspro, A. (2012) *Optical Nanoscopy* **1(1)**, 3.

[21] Reimer, L. (1998) Scanning electron microscopy: Physics of image formation and microanalysis, Springer series in optical sciencesSpringer, Berlin and New York 2nd completely rev. and updated edition.

[22] Williams, D. B. and Carter, C. B. (2009) Transmission electron microscopy: A textbook for materials science, Springer, New York 2nd edition.

[23] Bai, X.-c., Yan, C., Yang, G., Lu, P., Ma, D., Sun, L., Zhou, R., Scheres, S. H. W., and Shi, Y. (2015) *Nature* **525(7568)**, 212–217.

[24] Hell, S. and Wichmann, J. (1994) *Optics Letters* **19(11)**, 780–782.

[25] Hell, S. W. (1994) *Optics Communications* **106(1-3)**, 19–24.

[26] Hell, S. W. and Kroug, M. (1995) *Applied Physics B Lasers and Optics* **60(5)**, 495–497.

[27] Klar, T. A. and Hell, S. W. (1999) *Optics Letters* **24(14)**, 954.

[28] Klar, T. A., Jakobs, S., Dyba, M., Egner, A., and Hell, S. W. (2000) *Proceedings of the National Academy of Sciences* **97(15)**, 8206–8210.

[29] Hell, S. W. (2007) *Science* **316(5828)**, 1153–1158.

[30] Rittweger, E., Wildanger, D., and Hell, S. W. (2009) *Europhysics Letters* **86(1)**, 14001.

[31] Hell, S. W., Jakobs, S., and Kastrup, L. (2003) *Applied Physics A: Materials Science & Processing* **77(7)**, 859–860.

[32] Hell, S., Dyba, M., and Jakobs, S. (2004) *Current Opinion in Neurobiology* **14(5)**, 599–609.

[33] Hofmann, M., Eggeling, C., Jakobs, S., and Hell, S. W. (2005) *Proceedings of the National Academy of Sciences* **102(49)**, 17565–17569.

[34] Grotjohann, T., Testa, I., Leutenegger, M., Bock, H., Urban, N. T., Lavoie-Cardinal, F., Willig, K. I., Eggeling, C., Jakobs, S., and Hell, S. W. (2011) *Nature* **478(7368)**, 204–208.

[35] Brakemann, T., Stiel, A. C., Weber, G., Andresen, M., Testa, I., Grotjohann, T., Leutenegger, M., Plessmann, U., Urlaub, H., Eggeling, C., Wahl, M. C., Hell, S. W., and Jakobs, S. (2011) *Nature Biotechnology* **29(10)**, 942–947.

[36] Grotjohann, T., Testa, I., Reuss, M., Brakemann, T., Eggeling, C., Hell, S. W., and Jakobs, S. (2012) *eLife* **1**, e00248.

[37] Testa, I., Urban, N. T., Jakobs, S., Eggeling, C., Willig, K. I., and Hell, S. W. (2012) *Neuron* **75(6)**, 992–1000.

[38] Chmyrov, A., Keller, J., Grotjohann, T., Ratz, M., D'Este, E., Jakobs, S., Eggeling, C., and Hell, S. W. (2013) *Nature Methods* **10(8)**, 737–740.

[39] Lavoie-Cardinal, F., Jensen, N. A., Westphal, V., Stiel, A. C., Chmyrov, A., Bierwagen, J., Testa, I., Jakobs, S., and Hell, S. W. (2014) *ChemPhysChem* **15(4)**, 655–663.

[40] Bossi, M., Fölling, J., Dyba, M., Westphal, V., and Hell, S. W. (2006) *New Journal of Physics* **8(11)**, 275.

[41] Heintzmann, R., Jovin, T. M., and Cremer, C. (2002) *Journal of the Optical Society of America A* **19(8)**, 1599.

[42] Gustafsson, M. G. L. (2005) *Proceedings of the National Academy of Sciences of the United States of America* **102(37)**, 13081–13086.

[43] Hell, S. W. (2010) Far-Field Optical Nanoscopy volume **96**, of Springer Series in Chemical Physics pp. 365–398 Springer Berlin, Heidelberg.

[44] Sahl, S. J., Balzarotti, F., Keller-Findeisen, J., Leutenegger, M., Westphal, V., Egner, A., Lavoie-Cardinal, F., Chmyrov, A., Grotjohann, T., and Jakobs, S. (2016) *Science* **352(6285)**, 527.

[45] Rego, E. H., Shao, L., Macklin, J. J., Winoto, L., Johansson, G. A., Kamps-Hughes, N., Davidson, M. W., and Gustafsson, M. G. L. (2012) *Proceedings of the National Academy of Sciences of the United States of America* **109(3)**, E135–43.

[46] Li, D., Shao, L., Chen, B.-C., Zhang, X., Zhang, M., Moses, B., Milkie, D. E., Beach, J. R., Hammer, J. A. r., Pasham, M., Kirchhausen, T., Baird, M. A., Davidson, M. W., Xu, P., and Betzig, E. (2015) *Science* **349(6251)**, aab3500.

[47] Li, D. and Betzig, E. (2016) *Science* **352(6285)**, 527.

[48] Han, K. Y., Wildanger, D., Rittweger, E., Meijer, J., Pezzagna, S., Hell, S. W., and Eggeling, C. (2012) *New Journal of Physics* **14(12)**, 123002.

[49] Bretschneider, S., Eggeling, C., and Hell, S. W. (2007) *Physical review letters* **98(21)**, 218103.

[50] Han, K. Y., Kim, S. K., Eggeling, C., and Hell, S. W. (2010) *Nano Letters* **10(8)**, 3199–3203.

[51] Westphal, V., Rizzoli, S. O., Lauterbach, M. A., Kamin, D., Jahn, R., and Hell, S. W. (2008) *Science* **320(5873)**, 246–249.

[52] Schneider, J., Zahn, J., Maglione, M., Sigrist, S. J., Marquard, J., Chojnacki, J., Krausslich, H.-G., Sahl, S. J., Engelhardt, J., and Hell, S. W. (2015) *Nature Methods* **12(9)**, 827–830.

[53] Schwentker, M. Parallelized Ground State Depletion PhD thesis Heidelberg (2007).

[54] Bingen, P., Reuss, M., Engelhardt, J., and Hell, S. W. (2011) *Optics Express* **19(24)**, 23716–23726.

[55] Yang, B., Przybilla, F., Mestre, M., Trebbia, J. B., and Lounis, B. (2014) *Optics Express* **22(5)**, 5581–5589.

[56] Bergermann, F., Alber, L., Sahl, S. J., Engelhardt, J., and Hell, S. W. (2015) *Optics Express* **23(1)**, 211.

[57] Betzig, E., Patterson, G. H., Sougrat, R., Lindwasser, O. W., Olenych, S., Bonifacino, J. S., Davidson, M. W., Lippincott-Schwartz, J., and Hess, H. F. (2006) *Science* **313(5793)**, 1642–1645.

[58] Hess, S. T., Girirajan, T. P. K., and Mason, M. D. (2006) *Biophysical Journal* **91(11)**, 4258–4272.

[59] Rust, M. J., Bates, M., and Zhuang, X. (2006) *Nature Methods* **3(10)**, 793–795.

[60] Fölling, J., Belov, V., Kunetsky, R., Medda, R., Schönle, A., Egner, A., Eggeling, C., Bossi, M., and Hell, S. W. (2007) *Angewandte Chemie* **119(33)**, 6382–6386.

[61] Heilemann, M., van de Linde, S., Schuttpelz, M., Kasper, R., Seefeldt, B., Mukherjee, A., Tinnefeld, P., and Sauer, M. (2008) *Angewandte Chemie International Edition* **47(33)**, 6172–6176.

[62] Bock, H., Geisler, C., Wurm, C. A., vonMiddendorff, C., Jakobs, S., Schönle, A., Egner, A., Hell, S. W., and Eggeling, C. (2007) *Applied Physics B* **88(2)**, 161–165.

[63] Egner, A., Geisler, C., vonMiddendorf, C., Bock, H., Wenzel, D., Medda, R., Andresen, M., Stiel, A. C., Jakobs, S., Eggeling, C., Schönle, A., and Hell, S. W. (2007) *Biophysical Journal* **93(9)**, 3285–3290.

[64] Geisler, C., Schönle, A., vonMiddendorff, C., Bock, H., Eggeling, C., Egner, A., and Hell, S. W. (2007) *Applied Physics A* **88(2)**, 223–226.

[65] Cognet, L., Tsyboulski, D. A., and Weisman, R. B. (2008) *Nano Letters* **8(2)**, 749–753.

[66] Hoyer, P., Staudt, T., Engelhardt, J., and Hell, S. W. (2011) *Nano Letters* **11(1)**, 245–250.

[67] Fölling, J., Bossi, M., Bock, H., Medda, R., Wurm, C. A., Hein, B., Jakobs, S., Eggeling, C., and Hell, S. W. (2008) *Nature Methods* **5(11)**, 943–945.

[68] van de Linde, S., Kasper, R., Heilemann, M., and Sauer, M. (2008) *Applied Physics B* **93(4)**, 725–731.

[69] Dertinger, T., Colyer, R., Iyer, G., Weiss, S., and Enderlein, J. (2009) *Proceedings of the National Academy of Sciences of the United States of America* **106(52)**, 22287–22292.

[70] Danzl, J. G., Sidenstein, S. C., Gregor, C., Urban, N. T., Ilgen, P., Jakobs, S., and Hell, S. W. (2016) *Nature Photonics* **10(2)**, 122–128.

[71] Dyba, M., Keller, J., and Hell, S. W. (2005) *New Journal of Physics* **7**, 134.

[72] Harke, B., Keller, J., Ullal, C. K., Westphal, V., Schoenle, A., and Hell, S. W. (2008) *Optics Express* **16(6)**, 4154–4162.

[73] Willig, K. I., Harke, B., Medda, R., and Hell, S. W. (2007) *Nature Methods* **4(11)**, 915–918.

[74] Vicidomini, G., Moneron, G., Han, K. Y., Westphal, V., Ta, H., Reuss, M., Engelhardt, J., Eggeling, C., and Hell, S. W. (2011) *Nature Methods* **8(7)**, 571–573.

[75] Donnert, G., Keller, J., Medda, R., Andrei, M. A., Rizzoli, S. O., Lührmann, R., Jahn, R., Eggeling, C., and Hell, S. W. (2006) *Proceedings of the National Academy of Sciences of the United States of America* **103(31)**, 11440–11445.

[76] Göttfert, F., Wurm, C. A., Müller, V., Berning, S., Cordes, V. C., Honigmann, A., and Hell, S. W. (2013) *Biophysical Journal* **105(1)**, L01–L03.

[77] Rittweger, E., Han, K. Y., Irvine, S. E., Eggeling, C., and Hell, S. W. (2009) *Nature Photonics* **3(3)**, 144–147.

[78] Reuss, M., Engelhardt, J., and Hell, S. W. (2010) *Optics Express* **18(2)**, 1049–1058.

[79] Engler, A. Adaptive elements for STED microscopy PhD thesis Heidelberg (2009).

[80] Booth, M., Andrade, D., Burke, D., Patton, B., and Zurauskas, M. (2015) *Microscopy (Oxford, England)* **64(4)**, 251–261.

[81] Donnert, G., Eggeling, C., and Hell, S. W. (2006) *Nature Methods* **4(1)**, 81–86.

[82] Donnert, G., Eggeling, C., and Hell, S. W. (2009) *Photochemical & Photobiological Sciences* **8(4)**, 481.

[83] Staudt, T., Engler, A., Rittweger, E., Harke, B., Engelhardt, J., and Hell, S. W. (2011) *Optics Express* **19(6)**, 5644–5657.

[84] Harke, B., Ullal, C. K., Keller, J., and Hell, S. W. (2008) *Nano Letters* **8(5)**, 1309–1313.

[85] Wildanger, D., Medda, R., Kastrup, L., and Hell, S. W. (2009) *Journal of Microscopy* **236(1)**, 35–43.

[86] Osseforth, C., Moffitt, J. R., Schermelleh, L., and Michaelis, J. (2014) *Optics Express* **22(6)**, 7028.

[87] Dyba, M. and Hell, S. W. (2002) *Physical Review Letters* **88(16)**, 163901.

[88] Dyba, M., Jakobs, S., and Hell, S. W. (2003) *Nature Biotechnology* **21(11)**, 1303–1304.

[89] Schmidt, R., Wurm, C. A., Jakobs, S., Engelhardt, J., Egner, A., and Hell, S. W. (2008) *Nature Methods* **5(6)**, 539–544.

[90] Friedrich, M., Gan, Q., Ermolayev, V., and Harms, G. S. (2011) *Biophysical Journal* **100(8)**, L43–5.

[91] Gould, T. J., Burke, D., Bewersdorf, J., and Booth, M. J. (2012) *Optics Express* **20(19)**, 20998–21009.

[92] Gould, T. J., Kromann, E. B., Burke, D., Booth, M. J., and Bewersdorf, J. (2013) *Optics Letters* **38(11)**, 1860–1862.

[93] Schmidt, R., Wurm, C. A., Punge, A., Egner, A., Jakobs, S., and Hell, S. W. (2009) *Nano Letters* **9(6)**, 2508–2510.

[94] Kolmakov, K., Belov, V. N., Wurm, C. A., Harke, B., Leutenegger, M., Eggeling, C., and Hell, S. W. (2010) *European Journal of Organic Chemistry* **2010(19)**, 3593–3610.

[95] Kolmakov, K., Wurm, C. A., Hennig, R., Rapp, E., Jakobs, S., Belov, V. N., and Hell, S. W. (2012) *Chemistry (Weinheim an der Bergstrasse, Germany)* **18(41)**, 12986–12998.

[96] Willig, K. I., Kellner, R. R., Medda, R., Hein, B., Jakobs, S., and Hell, S. W. (2006) *Nature Methods* **3(9)**, 721–723.

[97] Rankin, B. R., Moneron, G., Wurm, C. A., Nelson, J. C., Walter, A., Schwarzer, D., Schroeder, J., Colón-Ramos, D. A., and Hell, S. W. (2011) *Biophysical Journal* **100(12)**, L63–L65.

[98] Griesbeck, O., Baird, G. S., Campbell, R. E., Zacharias, D. A., and Tsien, R. Y. (2001) *Journal of Biological Chemistry* **276(31)**, 29188–29194.

[99] Hein, B., Willig, K. I., and Hell, S. W. (2008) *Proceedings of the National Academy of Sciences* **105(38)**, 14271–14276.

[100] Morozova, K. S., Piatkevich, K. D., Gould, T. J., Zhang, J., Bewersdorf, J., and Verkhusha, V. V. (2010) *Biophysical Journal* **99(2)**, L13–L15.

[101] Berning, S., Willig, K. I., Steffens, H., Dibaj, P., and Hell, S. W. (2012) *Science* **335(6068)**, 551.

[102] Hein, B., Willig, K. I., Wurm, C. A., Westphal, V., Jakobs, S., and Hell, S. W. (2010) *Biophysical Journal* **98(1)**, 158–163.

[103] Lukinavičius, G., Umezawa, K., Olivier, N., Honigmann, A., Yang, G., Plass, T., Mueller, V., Reymond, L., Corrêa Jr, I. R., Luo, Z.-G., Schultz, C., Lemke, E. A., Heppenstall, P., Eggeling, C., Manley, S., and Johnsson, K. (2013) *Nature Chemistry* **5(2)**, 132–139.

[104] Correa, JR, I. R. (2014) *Current Opinion in Chemical Biology* **20**, 36–45.

[105] Butkevich, A. N., Mitronova, G. Y., Sidenstein, S. C., Klocke, J. L., Kamin, D., Meineke, D. N. H., D'Este, E., Kraemer, P.-T., Danzl, J. G., Belov, V. N., and Hell, S. W. (2016) *Angewandte Chemie International Edition* **55(10)**, 3290–3294.

[106] Lukinavičius, G., Reymond, L., D'Este, E., Masharina, A., Göttfert, F., Ta, H., Güther, A., Fournier, M., Rizzo, S., Waldmann, H., Blaukopf, C., Sommer, C., Gerlich, D. W., Arndt, H.-D., Hell, S. W., and Johnsson, K. (2014) *Nature Methods* **11(7)**, 731–733.

[107] D'Este, E., Kamin, D., Göttfert, F., El-Hady, A., and Hell, S. W. (2015) *Cell Reports* **10(8)**, 1246–1251.

[108] Hense, A., Prunsche, B., Gao, P., Ishitsuka, Y., Nienhaus, K., and Ulrich Nienhaus, G. (2015) *Scientific Reports* **5**, 18006.

[109] Gadella, D., conference presentation, ELMI meeting 2016, Debrecen, Hungary (05/25/2016).

[110] Shcherbakova, D. M., Baloban, M., and Verkhusha, V. V. (2015) *Current Opinion in Chemical Biology* **27**, 52–63.

[111] Hanne, J., Falk, H. J., Görlitz, F., Hoyer, P., Engelhardt, J., Sahl, S. J., and Hell, S. W. (2015) *Nature Communications* **6**, 7127.

[112] Chozinski, T. J., Gagnon, L. A., and Vaughan, J. C. (2014) *FEBS Letters* **588(19)**, 3603–3612.

[113] Hell, S. W., Sahl, S. J., Bates, M., Zhuang, X., Heintzmann, R., Booth, M. J., Bewersdorf, J., Shtengel, G., Hess, H., Tinnefeld, P., Honigmann, A., Jakobs, S., Testa, I., Cognet, L., Lounis, B., Ewers, H., Davis, S. J., Eggeling, C., Klenerman, D., Willig, K. I., Vicidomini, G., Castello, M., Diaspro, A., and Cordes, T. (2015) *Journal of Physics D: Applied Physics* **48(44)**, 443001.

[114] Harris, L. J., Skaletsky, E., and McPherson, A. (1998) *Journal of molecular biology* **275(5)**, 861–872.

[115] Hell, S. W. (2009) *Nature Methods* **6(1)**, 24–32.

[116] Huang, B., Bates, M., and Zhuang, X. (2009) *Annual Review of Biochemistry* **78**, 993–1016.

[117] Ries, J., Kaplan, C., Platonova, E., Eghlidi, H., and Ewers, H. (2012) *Nature Methods* **9(6)**, 582–584.

[118] Pleiner, T., Bates, M., Trakhanov, S., Lee, C.-T., Schliep, J. E., Chug, H., Böhning, M., Stark, H., Urlaub, H., and Görlich, D. (2015) *eLife* **4**, 213.

[119] Riedl, J., Crevenna, A. H., Kessenbrock, K., Yu, J. H., Neukirchen, D., Bista, M., Bradke, F., Jenne, D., Holak, T. A., Werb, Z., Sixt, M., and Wedlich-Soldner, R. (2008) *Nature Methods* **5(7)**, 605–607.

[120] Keppler, A., Gendreizig, S., Gronemeyer, T., Pick, H., Vogel, H., and Johnsson, K. (2002) *Nature Biotechnology* **21(1)**, 86–89.

[121] Gautier, A., Juillerat, A., Heinis, C., Corrêa, I. R., Kindermann, M., Beaufils, F., and Johnsson, K. (2008) *Chemistry & Biology* **15(2)**, 128–136.

[122] Los, G. V., Encell, L. P., McDougall, M. G., Hartzell, D. D., Karassina, N., Zimprich, C., Wood, M. G., Learish, R., Ohana, R. F., Urh, M., Simpson, D., Mendez, J., Zimmerman, K., Otto, P., Vidugiris, G., Zhu, J., Darzins, A., Klaubert, D. H., Bulleit, R. F., and Wood, K. V. (2008) *ACS Chemical Biology* **3(6)**, 373–382.

[123] Ullal, C. K., Schmidt, R., Hell, S. W., and Egner, A. (2009) *Nano Letters* **9(6)**, 2497–2500.

[124] Busko, D., Baluschev, S., Crespy, D., Turshatov, A., and Landfester, K. (2012) *Micron* **43(5)**, 583–588.

[125] Huang, B., Babcock, H., and Zhuang, X. (2010) *Cell* **143**, 1047–1058.

[126] Castro, J. B. and Gould, T. J. (2015) *Journal of Histochemistry & Cytochemistry* **63(12)**, 897–907.

[127] Willig, K. I. and Barrantes, F. J. (2014) *Current Opinion in Chemical Biology* **20**, 16–21.

[128] Chereau, R., Tønnesen, J., and Nägerl, U. V. (2015) *Methods (San Diego, Calif.)* **88**, 57–66.

[129] Eggeling, C. (2015) *Essays in biochemistry* **57**, 69–80.

[130] Kittel, R. J., Wichmann, C., Rasse, T. M., Fouquet, W., Schmidt, M., Schmid, A., Wagh, D. A., Pawlu, C., Kellner, R. R., Willig, K. I., Hell, S. W., Buchner, E., Heckmann, M., and Sigrist, S. J. (2006) *Science* **312(5776)**, 1051–1054.

[131] Honigmann, A., Sadeghi, S., Keller, J., Hell, S. W., Eggeling, C., and Vink, R. (2014) *eLife* **3**, e01671.

[132] Honigmann, A., Mueller, V., Ta, H., Schoenle, A., Sezgin, E., Hell, S. W., and Eggeling, C. (2014) *Nature Communications* **5**, 5412.

[133] Jakobs, S. and Wurm, C. A. (2014) *Current Opinion in Chemical Biology* **20**, 9–15.

[134] Xu, K., Zhong, G., and Zhuang, X. (2012) *Science* **339(6118)**, 452–456.

[135] Zhong, G., He, J., Zhou, R., Lorenzo, D., Babcock, H. P., Bennett, V., and Zhuang, X. (2014) *eLife* **3**, e04581.

[136] He, J., Zhou, R., Wu, Z., Carrasco, M. A., Kurshan, P. T., Farley, J. E., Simon, D. J., Wang, G., Han, B., Hao, J., Heller, E., Freeman, M. R., Shen, K., Maniatis, T., Tessier-Lavigne, M., and Zhuang, X. (2016) *Proceedings of the National Academy of Sciences of the United States of America* **113(21)**, 6029–6034.

[137] Wäldchen, S., Lehmann, J., Klein, T., van de Linde, S., and Sauer, M. (2015) *Scientific Reports* **5**, 15348.

[138] Hotta, J.-i., Fron, E., Dedecker, P., Janssen, K. P. F., Li, C., Müllen, K., Harke, B., Bückers, J., Hell, S. W., and Hofkens, J. (2010) *Journal of the American Chemical Society* **32(14)**, 5021–5023.

[139] Chudakov, D. M., Verkhusha, V. V., Staroverov, D. B., Souslova, E. A., Lukyanov, S., and Lukyanov, K. A. (2004) *Nature Biotechnology* **22(11)**, 1435–1439.

[140] Ando, R., Mizuno, H., and Miyawaki, A. (2004) *Science* **306(5700)**, 1370–1373.

[141] Dickson, R. M., Cubitt, A. B., Tsien, R. Y., and Moerner, W. E. (1997) *Nature* **388(6640)**, 355–358.

[142] Stiel, A. C., Trowitzsch, S., Weber, G., Andresen, M., Eggeling, C., Hell, S. W., Jakobs, S., and Wahl, M. C. (2007) *Biochemical Journal* **402(1)**, 35.

[143] Tønnesen, J., Nadrigny, F., Willig, K. I., Wedlich-Söldner, R., and Nägerl, U. V. (2011) *Biophysical Journal* **101(10)**, 2545–2552.

[144] Irie, M. (2000) *Chemistry Reviews* **100**, 1685–1716.

[145] Vandenberg, W., Leutenegger, M., Lasser, T., Hofkens, J., and Dedecker, P. (2015) *Cell and tissue research* **360(1)**, 151–178.

[146] Stiel, A. C., Trowitzsch, S., Weber, G., Andresen, M., Eggeling, C., Hell, S. W., Jakobs, S., and Wahl, M. C. (2007) *Biochemical Journal* **402(1)**, 35–42.

[147] Vicidomini, G., Moneron, G., Han, K. Y., Westphal, V., Ta, H., Reuss, M., Engelhardt, J., Eggeling, C., and Hell, S. W. (2011) *Nature Methods* **8(7)**, 571–573.

[148] Keller, J., Schönle, A., and Hell, S. W. (2007) *Optics Express* **15(6)**, 3361.

[149] Griesbeck, O., Baird, G. S., Campbell, R. E., Zacharias, D. A., and Tsien, R. Y. (2001) *Journal of Biological Chemistry* **276(31)**, 29188–29194.

[150] Neher, R. and Neher, E. (2004) *Journal of Microscopy* **213(1)**, 46–62.

[151] Zimmermann, T., Rietdorf, J., and Pepperkok, R. (2003) *FEBS Letters* **546(1)**, 87–92.

[152] Urban, N. T., Willig, K. I., Hell, S. W., and Nägerl, U. V. (2011) *Biophysical Journal* **101(5)**, 1277–1284.

[153] Tønnesen, J., Katona, G., Rózsa, B., and Nägerl, U. V. (2014) *Nature Neuroscience* **17**, 678–685.

[154] Gähwiler, B. H., Capogna, M., Debanne, D., McKinney, R. A., and Thompson, S. M. (1997) *Trends in Neurosciences* **20(10)**, 471–477.

[155] DiCiommo, D. P. and Bremner, R. (1998) *Journal of Biological Chemistry* **273(29)**, 18060–18066.

[156] Hell, S. W. (2015) *Angewandte Chemie International Edition* **54(28)**, 8054–8066.

[157] D'Este, E., Kamin, D., Velte, C., Göttfert, F., Simons, M., and Hell, S. W. (2016) *Scientific Reports* **6**, 22741.

[158] Donnert, G., Keller, J., Wurm, C. A., Rizzoli, S. O., Westphal, V., Schönle, A., Jahn, R., Jakobs, S., Eggeling, C., and Hell, S. W. (2007) *Biophysical Journal* **92(8)**, L67–L69.

[159] Meyer, L., Wildanger, D., Medda, R., Punge, A., Rizzoli, S. O., Donnert, G., and Hell, S. W. (2008) *Small* **4(8)**, 1095–1100.

[160] Blom, H., RöNnlund, D., Scott, L., Spicarova, Z., Rantanen, V., Widengren, J., Aperia, A., and Brismar, H. (2012) *Microscopy Research and Technique* **75(2)**, 220–228.

[161] Dean, C., Liu, H., Staudt, T., Stahlberg, M. A., Vingill, S., Buckers, J., Kamin, D., Engelhardt, J., Jackson, M. B., Hell, S. W., and Chapman, E. R. (2012) *Journal of Neuroscience* **32(16)**, 5398–5413.

[162] Neumann, D., Bückers, J., Kastrup, L., Hell, S. W., and Jakobs, S. (2010) *PMC Biophysics* **3(1)**, 4.

[163] Opazo, F., Punge, A., Bückers, J., Hoopmann, P., Kastrup, L., Hell, S. W., and Rizzoli, S. O. (2010) *Traffic* **11(6)**, 800–812.

[164] Reisinger, E., Bresee, C., Neef, J., Nair, R., Reuter, K., Bulankina, A., Nouvian, R., Koch, M., Buckers, J., Kastrup, L., Roux, I., Petit, C., Hell, S. W., Brose, N., Rhee, J.-S., Kugler, S., Brigande, J. V., and Moser, T. (2011) *Journal of Neuroscience* **31(13)**, 4886–4895.

[165] Bückers, J., Wildanger, D., Vicidomini, G., Kastrup, L., and Hell, S. W. (2011) *Optics Express* **19(4)**, 3130.

[166] Clausen, M. P., Galiani, S., deLa Serna, J. B., Fritzsche, M., Chojnacki, J., Gehmlich, K., Lagerholm, B. C., and Eggeling, C. (2014) *NanoBioImaging* **1(1)**, 1–12.

[167] Friedemann, K., Turshatov, A., Landfester, K., and Crespy, D. (2011) *Langmuir* **27(11)**, 7132–7139.

[168] Pellett, P. A., Sun, X., Gould, T. J., Rothman, J. E., Xu, M.-Q., Corrêa, I. R., and Bewersdorf, J. (2011) *Biomedical Optics Express* **2(8)**, 2364.

[169] Leica Microsystems TCS SP8 STED 3X.

[170] Abberior Instruments GmbH 2C STED 775 QUAD Scan.

[171] PicoQuant MicroTime 200 STED.

[172] Winter, F. Multicolour STED nanoscopy with hyperspectral detection PhD thesis Heidelberg (2015).

[173] Willig, K. I., Stiel, A. C., Brakemann, T., Jakobs, S., and Hell, S. W. (2011) *Nano Letters* **11(9)**, 3970–3973.

[174] Eggeling, C., Willig, K. I., Sahl, S. J., and Hell, S. W. (2015) *Quarterly Reviews of Biophysics* **48(02)**, 178–243.

[175] Eggeling, C., Widengren, J., Rigler, R., and Seidel, C. A. M. (1999) Photostability of Fluorescent Dyes for Single-Molecule Spectroscopy: Mechanisms and Experimental Methods for Estimating Photobleaching in Aqueous Solution In Wolfgang Rettig, (ed.), Applied fluorescence in chemistry, biology, and medicine, pp. 193–240 Springer Berlin and New York.

[176] Tsien, R. Y., Ernst, L., and Waggoner, A. (2006) Fluorophores for Confocal Microscopy: Photophysics and Photochemistry In James B. Pawley, (ed.), Handbook Of Biological Confocal Microscopy, pp. 338–352 Springer US Boston, MA.

[177] Willig, K. I., Rizzoli, S. O., Westphal, V., Jahn, R., and Hell, S. W. (2006) *Nature* **440(7086)**, 935–939.

[178] Lauterbach, M. A., Guillon, M., Soltani, A., and Emiliani, V. (2013) *Scientific Reports* **3**, 2050.

[179] Dyba, M. and Hell, S. W. (2003) *Applied Optics* **42(25)**, 5123.

[180] Sidenstein, S. C., D'Este, E., Böhm, M. J., Danzl, J. G., Belov, V. N., and Hell, S. W. (2016) *Scientific Reports* **6**, 26725.

[181] Görlitz, F., Hoyer, P., Falk, H., Kastrup, L., Engelhardt, J., and Hell, S. W. (2014) *Progress In Electromagnetics Research* **147**, 57–68.

[182] Schmied, J. J., Gietl, A., Holzmeister, P., Forthmann, C., Steinhauer, C., Dammeyer, T., and Tinnefeld, P. (2012) *Nature Methods* **9(12)**, 1133–1134.

[183] GATTAquant GATTA-STED Nanoruler (4/27/2016).

[184] Boyarskiy, V. P., Belov, V. N., Medda, R., Hein, B., Bossi, M., and Hell, S. W. (2008) *Chemistry - A European Journal* **14(6)**, 1784–1792.

[185] Neher, R. and Neher, E. (2004) *Journal of Microscopy* **213(1)**, 46–62.

[186] MPB Communications Inc. Nanosecond Pulsed Fiber Laser 775 nm (5/1/2016).

[187] Lynch, G. and Baudry, M. (1984) *Science* **224(4653)**, 1057–1063.

[188] Portis, A., Newton, C., Pangborn, W., and Papahadjopoulos, D. (1979) *Biochemistry* **18(5)**, 780–790.

[189] Pielage, J., Fetter, R. D., and Davis, G. W. (2005) *Current Biology* **15(10)**, 918–928.

[190] Pielage, J., Fetter, R. D., and Davis, G. W. (2006) *The Journal of Cell Biology* **175(3)**, 491–503.

[191] Susuki, K. and Rasband, M. N. (2008) *Experimental Biology and Medicine* **233(4)**, 394–400.

Contributions

The work was carried out in the Department Nanobiophotonics of the Max Planck Institute for Biophysical Chemistry in Göttingen. Research described in Chapter 2 was conducted together with Johann-Georg Danzl (built the microscope, planned experiments and evaluated data), Carola Gregor, Peter Ilgen, and Nicolai T. Urban (all provided samples, all Department Nanobiophotonics, MPI-BPC). Stefan W. Hell laid out the MOST concept, and initiated and supervised the project. I built the microscope, planned experiments, performed all measurements shown, and evaluated data.

Research described in Chapter 3 was conducted together with Elisa D'Este (provided samples, performed imaging experiments, and analyzed data), Marvin J. Böhm (synthesized *540R* dye derivatives), Johann-Georg Danzl (built initial parts of the setup), and Vladimir N. Belov (synthesized dye derivatives, all Department Nanobiophotonics, MPI-BPC). Stefan W. Hell initiated and supervised the project. I built the setup, developed the imaging and multilevel STED schemes, planned and performed experiments, and analyzed data.

List of Publications

Peer-reviewed publications

J.G. Danzl†, S.C. Sidenstein†, C. Gregor, N.T. Urban, P. Ilgen, S. Jakobs, S.W. Hell Coordinate-targeted fluorescence nanoscopy with multiple off states. (2016) *Nature Photonics* **10**, 122-128. †Equal contributors.

S.C. Sidenstein, E. D'Este, M.J. Böhm, J.G. Danzl, V.N. Belov, S.W. Hell Multicolour Multilevel STED nanoscopy of Actin/Spectrin Organization at Synapses. (2016) *Scientific Reports* **6**, 26725.

A.N. Butkevich, G.Yu. Mitronova, S.C. Sidenstein, J. Klocke, D. Kamin, D.N.H. Meineke, E. D'Este, P.-T. Kraemer, J.G. Danzl, V.N. Belov, S.W. Hell Fluorescent Rhodamines and Fluorogenic Carbopyronines for Super-Resolution STED Microscopy in Living Cells. (2016) *Angewandte Chemie International Edition* **55**, 3290-3294.

Patent application

S.C. Sidenstein/S.W. Hell/Max-Planck-Gesellschaft zur Förderung der Wissenschaften e.V.: „Mehrfarbiges hochauflösendes Laser-Scanning-Mikroskop." filed on 03/07/2016.

Conference contributions

S.C. Sidenstein, J.G. Danzl, C. Gregor, N.T. Urban, P. Ilgen, S. Jakobs, S.W. Hell: Oral presentation „Coordinate-targeted fluorescence nanoscopy with multiple off states.", (2016) ELMI Meeting, Debrecen, Ungarn.

S.C. Sidenstein, E. D'Este, M.J. Böhm, J.G. Danzl, V.N. Belov, S.W. Hell: Poster presentation „Coaligned Three-Colour STED Nanoscopy Reveals Cytoskeletal Organization at Synaptic Sites.", (2016) ELMI Meeting, Debrecen, Ungarn.

S.C. Sidenstein, J.G. Danzl, C. Gregor, N.T. Urban, P. Ilgen, S. Jakobs, S.W. Hell: Poster presentation „Coordinate-targeted fluorescence nanoscopy with multiple off states.", (2016) 66th Lindau Nobel Laureate Meeting, Lindau, Germany.

Danksagungen

Diese Arbeit wurde in der Abteilung Nanobiophotonik des Max-Planck-Institutes für Biophysikalische Chemie in Göttingen durchgeführt. Viele Personen haben zum Erfolg dieser Arbeit beigetragen. Ich danke sehr herzlich:

Prof. Stefan W. Hell für die Möglichkeit an spannenden Projekten in diesem aufstrebendem Forschungsgebiet unter idealen Bedingungen arbeiten zu dürfen und für seine engagierte Betreuung und Förderung;

Prof. Holger Schönherr danke ich für seine fortwährende Unterstützung und die Begutachtung dieser Arbeit;

Johann-Georg Danzl für die intensive gemeinsame Arbeit im Projekt protected STED, Carola Gregor für viele biologisch-präparative Arbeiten, Peter Ilgen für den actin chromobody und Nicolai Urban für die Präparation von Hirnschnitten;

Elisa D'Este für die spannenden Neuronenproben und insgesamt für die großartige Zusammenarbeit im Projekt Multicolour Multilevel STED;

Vladimir Belov und Marvin Böhm für die Bereitstellung zellgängiger Fluoreszenzfarbstoffe und die sehr produktive Zusammenarbeit auch im Rahmen weiterer Projekte;

Maria Kamper, Flavie Lavoie-Cardinal, Jan Keller, Tim Grotjohann, Alf Honigmann und Andreas Schönle für viele hilfreiche Diskussionen;

Tanja Gilat, Ellen Rothermel und Jaydev Jethwa für die exzellente Arbeit bei Probenvorbereitung und Labortechnik;

den sehr engagierten Mitarbeitern der Werkstätten für Feinmechanik, Optik und Elektronik des Institutes für biophysikalische Chemie;

Elisa D'Este, Maria Kamper, Katrin-Stephanie Tücking und Jaydev Jethwa für das Korrekturlesen dieser Arbeit;

den aktuellen und ehemaligen Kollegen und Freunden aus der Abteilung NanoBiophotonik für die tolle Atmosphäre und dabei im Besonderen Maria Kamper;

nichtzuletzt meinen Eltern für ihren fortwährenden Rückhalt. Ohne Euch wäre das alles nicht zu schaffen gewesen!